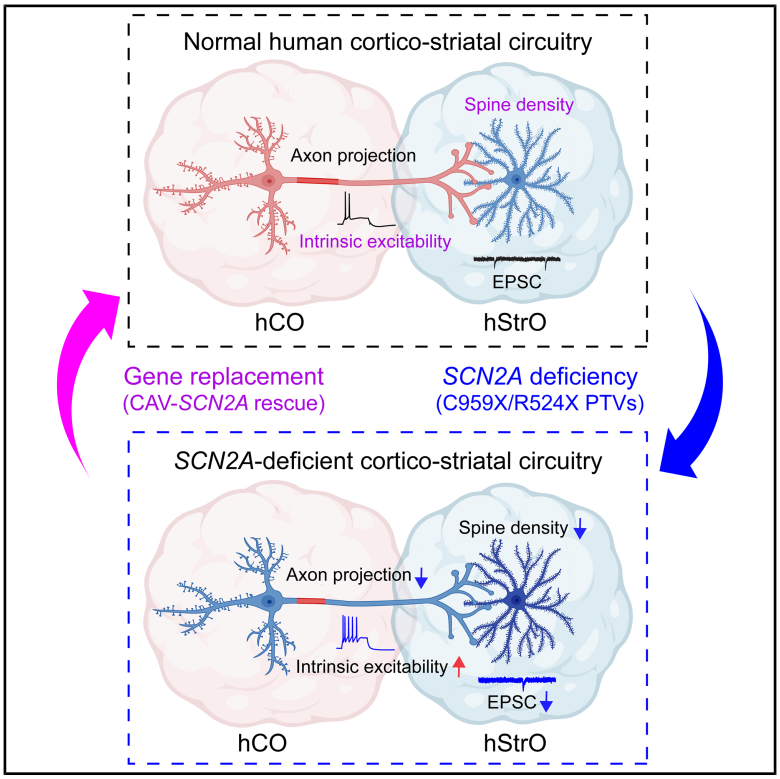
Neuron

Article

Autism-associated *SCN2A* deficiency disrupts cortico-striatal circuitry in human brain assembloids

Graphical abstract



Highlights

- Human assembloids enable the study of circuit mechanisms in neurodevelopmental disorders
- *SCN2A* PTVs impair cortical projections and reduce excitatory input to the striatum
- Both cortical and striatal defects contribute to reduced dendritic spine density
- *SCN2A* delivery via CAV-2 mitigates synaptic deficits and normalizes elevated firing

Authors

Xiaoling Chen, Jingliang Zhang, Jiaxiang Wu, ..., William C. Skarnes, Eric J. Kremer, Yang Yang

Correspondence

yangyang@purdue.edu

In brief

Chen et al. show that *SCN2A* protein-truncating variants disrupt cortico-striatal circuitry while increasing neuronal excitability in human brain assembloids. CAV-2-mediated *SCN2A* restoration mitigates intrinsic hyperexcitability and circuit deficits, supporting targeted gene replacement as a potential therapeutic strategy for *SCN2A*-related neurodevelopmental disorders.

Chen et al., 2027, Neuron *115*, 1–14
March 3, 2027 © 2026 Elsevier Inc. All rights are reserved, including those for text and data mining, AI training, and similar technologies.
https://doi.org/10.1016/j.neuron.2026.08.031

CellPress

Please cite this article in press as: Chen et al., Autism-associated *SCN2A* deficiency disrupts cortico-striatal circuitry in human brain assembloids, Neuron (2026), https://doi.org/10.1016/j.neuron.2026.08.031

Neuron

CellPress

Article

Autism-associated *SCN2A* deficiency disrupts cortico-striatal circuitry in human brain assembloids

Xiaoling Chen,[1,2,11] Jingliang Zhang,[1,2,11] Jiaxiang Wu,[1,2] Morgan J. Robinson,[1,2,3] Harish Kothandaraman,[4] Ye-Eun Yoo,[1,2] Iria M. Gonzalez Dopeso-Reyes,[5] Thomas D. Buffenoir,[5] Manasi S. Halurkar,[1,2] Hui Yang,[1,2] Zaiyang Zhang,[1,2] Muhan Wang,[1,2] Erin N. Creager,[6] Harris D. Giles,[7] Yuanrui Zhao,[1,2] Maria I. Olivero-Acosta,[1,2] Kyle W. Wettschurack,[1,2] Zhefu Que,[1,2] Jing Liu,[7] Chongli Yuan,[2,3] Allison J. Schaser,[2,8] Nadia A. Lanman,[4,9] Jean-Christophe Rochet,[1,2] William C. Skarnes,[10] Eric J. Kremer,[5,12] and Yang Yang[1,2,4,12,13,*]

[1]Borch Department of Medicinal Chemistry and Molecular Pharmacology, College of Pharmacy, Purdue University, West Lafayette, IN 47907, USA
[2]Purdue Institute for Integrative Neuroscience, Purdue University, West Lafayette, IN 47907, USA
[3]Davidson School of Chemical Engineering, Purdue University, West Lafayette, IN 47907, USA
[4]Purdue Institute for Cancer Research, Purdue University, West Lafayette, IN 47907, USA
[5]Institut de Génétique Moléculaire de Montpellier, Université de Montpellier, CNRS UMR 5535, 34090 Montpellier, France
[6]College of Science, Purdue University, West Lafayette, IN 47907, USA
[7]Department of Physics and Astronomy, Purdue University, West Lafayette, IN 47907, USA
[8]Department of Speech, Language, and Hearing Sciences, Purdue University, West Lafayette, IN 47907, USA
[9]Department of Comparative Pathobiology, College of Veterinary Medicine, Purdue University, West Lafayette, IN 47907, USA
[10]The Jackson Laboratory for Genomic Medicine, Farmington, CT 06032, USA
[11]These authors contributed equally
[12]Senior author
[13]Lead contact
*Correspondence: yangyang@purdue.edu
https://doi.org/10.1016/j.neuron.2026.08.031

SUMMARY

Profound autism spectrum disorder (ASD) is frequently attributable to single-gene mutations, with *SCN2A*, encoding the voltage-gated sodium channel $Na_V1.2$, among the most penetrant. Cortico-striatal circuitry is a key node implicated in ASD, yet how *SCN2A* deficiency alters human neural circuits remains unclear. Using a human cortico-striatal assembloid model, we show that autism-causing heterozygous *SCN2A* protein-truncating variants (PTVs) impair long-range cortical axonal projections, reduce striatal spine density, and attenuate excitatory cortico-striatal synaptic transmission. Genotype-defined assembloids reveal contributions from both impaired cortical projections and intrinsic striatal vulnerability. Paradoxically, despite these connectivity deficits, *SCN2A*-deficient neurons exhibit increased intrinsic excitability, and assembloids show elevated spontaneous network firing, suggesting a potentially distinctive feature of human neural models. Notably, canine adenovirus type 2-mediated delivery of human *SCN2A* rescued cellular and circuit deficits. Collectively, our study unveils human circuit dysfunction caused by *SCN2A* deficiency and supports the therapeutic potential of targeted gene replacement for *SCN2A*-related ASD.

INTRODUCTION

Autism spectrum disorder (ASD) affects about 1 in 31 children in the United States.[1] Although etiologically heterogeneous,[2] profound forms of ASD often result from rare, highly penetrant variants in single genes.[3] Among these, loss-of-function (LoF) mutations in *SCN2A*, which encodes the voltage-gated sodium channel $Na_V1.2$, have emerged as a leading cause of monogenic ASD.[4,5] The *de novo* nonsense mutation *SCN2A c.2877C>A* (p.Cys959Ter; C959X), for example, produces a protein-truncating variant (PTV) associated with severe clinical consequences.[4,6,7] $Na_V1.2$ is predominantly localized at the axon initial segment (AIS) and supports action potential (AP) initiation and propagation in developing neurons, while rodent studies also implicate $Na_V1.2$ in synaptic transmission and dendritic function.[8,9] However, how *SCN2A* deficiency disrupts human neuronal communication, particularly the cortico-striatal circuitry, a key circuit involved in ASD,[10,11] remains poorly understood.

The emerging human induced pluripotent stem cell (hiPSC)-derived brain organoids have revolutionized the study of human

All rights are reserved, including those for text and data mining, AI training, and similar technologies.

Please cite this article in press as: Chen et al., Autism-associated *SCN2A* deficiency disrupts cortico-striatal circuitry in human brain assembloids, Neuron (2026), https://doi.org/10.1016/j.neuron.2026.08.031

neural development and neurodevelopmental disorders *in vitro*.[12,13] Brain assembloids integrating region-specific organoids further enable modeling of human interregional connectivity and circuit function.[14–19] We leveraged assembloid technology to reconstruct a cortico-striatal network comprising cortical pyramidal neurons and striatal medium spiny neurons (MSNs) to examine the consequences of $Na_V1.2$ deficiency on the human cortico-striatal circuit. For disorders caused by gene deficiency, gene replacement represents a promising therapeutic approach to restore gene function and alleviate disease phenotypes. Because the full-length *SCN2A* gene exceeds the packaging capacity (~4.7 kb) of widely used adeno-associated virus (AAV) vectors, we constructed CAV-*SCN2A*, a canine adenovirus type 2 (CAV-2) vector harboring a codon-optimized human *SCN2A* expression cassette. CAV-2 vectors can accommodate large genetic payloads (~34 kb) and exhibit other favorable features, including low immunogenicity, efficient retrograde transport, and sustained long-term expression.[20]

Here, we first confirmed the expected regional cell-type composition and organization of human cortical organoids (hCOs) and striatal organoids (hStrOs) by spatial transcriptomic profiling. Using hCO-hStrO assembloids, we then showed that cortical axonal innervation promotes synapse formation and functional connectivity with striatal neurons, establishing a circuit model to investigate how *SCN2A* haploinsufficiency disrupts human circuit assembly and function. Through imaging, electrophysiological, and bulk transcriptomic analyses, we found that assembloids carrying the *SCN2A*-C959X mutation exhibited impaired long-range cortical projections, reduced striatal spine density, and weakened excitatory cortico-striatal synaptic transmission. Genotype-defined mix-and-match assembloids further revealed that both the cortical presynaptic and striatal postsynaptic mechanisms contribute to reduced striatal spine density. Unexpectedly, despite these connectivity deficits, *SCN2A*-deficient neurons displayed increased intrinsic excitability, and assembloids exhibited elevated spontaneous network firing. An independent *SCN2A* PTV line, *SCN2A*-R524X, recapitulated key phenotypes, including reduced cortical projections, impaired striatal spinogenesis, and neuronal hyperexcitability. Importantly, CAV-2-mediated delivery of human *SCN2A* rescued these cellular and circuit deficits in *SCN2A*-mutant assembloids. Collectively, our findings provide critical insight into the molecular and circuit-level manifestations of *SCN2A* deficiency, demonstrate the utility of human brain assembloids for modeling ASD-associated circuit dysfunction, and highlight a promising gene replacement strategy for profound ASD.

RESULTS

Cortical projections promote striatal synapse formation and function in brain assembloids

To model human cortico-striatal circuitry *in vitro*, we generated hCOs and hStrOs from hiPSCs following established protocols (Figure S1A).[14] Immunostaining confirmed cortical identity in hCOs (day 85), with abundant expression of T-box brain transcription factor 1 (TBR1) and COUP-TF-interacting protein 2 (CTIP2) and minimal glutamic acid decarboxylase 67 (GAD67) labeling (Figure S1B). Special AT-rich sequence binding protein-2 $(SATB2)^+$ intratelencephalic-like neurons and $CTIP2^+$ deep-layer corticofugal-like neurons were also present, supporting the generation of cortical populations relevant to cortico-striatal projection formation. $SATB2^+$ cells became progressively more segregated from $CTIP2^+$ populations over time and were enriched toward outer cortical-like regions (Figure S1C). Xenium-based spatial profiling further identified *SATB2*$^+$, *BCL11B*$^+$ (encoding CTIP2), and *TBR1*$^+$ glutamatergic neuronal subgroups with corresponding spatial organization (Figure S1D). In parallel, hStrOs (day 120) expressed GAD67, dopamine- and cAMP-regulated phosphoprotein 32 (DARPP32), vesicular GABA transporter (VGAT), and neuronal nuclei (NeuN), consistent with the presence of striatal MSNs[14] and a GABAergic-enriched striatal identity (Figures S1B and S1E). Cell-type-resolved spatial profiling further identified MSN-like GABAergic neurons, together with non-MSN GABAergic neurons, progenitors, glutamatergic neurons, astroglia, and other cell types (Figure S1F).

We then fused hCOs and hStrOs to generate hCO-hStrO assembloids (Figure 1A). $SATB2^+$ nuclei were enriched in the hCO compartment, whereas DARPP32 immunoreactivity was markedly enriched in the hStrO compartment (Figure 1B), supporting preservation of regional identities after fusion. Although DARPP32 is expressed at low levels in cortical layer VI neurons,[21,22] its substantially stronger enrichment in hStrOs, together with the abundance of $GABA^+$ cells in hStrOs but not hCOs, further supported striatal identity (Figures S2A and S2B). Minimal cleaved caspase-3 (CC3) staining indicated low levels of apoptosis in both compartments (Figure S2C). To assess cortico-striatal connectivity, hCOs were transduced with AAV1-hSyn::Cre and hStrOs with AAV1-Ef1a-DIO-mScarlet (Ef1a, elongation factor 1 alpha; DIO, double-floxed inverted open reading frame) and AAV9-hSyn-EGFP. In this system, anterograde transfer of Cre from cortical neurons to striatal target cells induces mScarlet expression in connected hStrO neurons, while EGFP serves as a striatal compartment marker (Figure 1Ci). After fusion, $EGFP^+$/$mScarlet^+$ cells were detected in the hStrO compartment, indicating cortical projection to and synaptic engagement of striatal neurons. This connectivity was independently supported by retrograde labeling, in which hStrO-derived Cre labeled hCO neurons projecting to the hStrO compartment (Figure 1Cii).

To determine whether cortico-striatal connections were functional, we combined chemogenetic activation with whole-cell patch-clamp recording. hCOs were transduced with AAV9-hSyn-hM3D(Gq)-mCherry to express an excitatory Gq-coupled designer receptor exclusively activated by designer drugs (DREADD), and hStrOs were labeled with AAV9-hSyn-EGFP for compartment identification (Figure 1Di). Bath application of clozapine-N-oxide (CNO) increased spontaneous excitatory postsynaptic current (sEPSC) frequency in striatal neurons, an effect reversed during washout (Figures 1Dii–1Div). In addition, electrical stimulation of the cortical compartment evoked EPSCs in striatal neurons (Figure S2D). Together, these results demonstrate functional excitatory cortico-striatal synaptic transmission in hCO-hStrO assembloids.

Please cite this article in press as: Chen et al., Autism-associated *SCN2A* deficiency disrupts cortico-striatal circuitry in human brain assembloids, Neuron (2026), https://doi.org/10.1016/j.neuron.2026.08.031

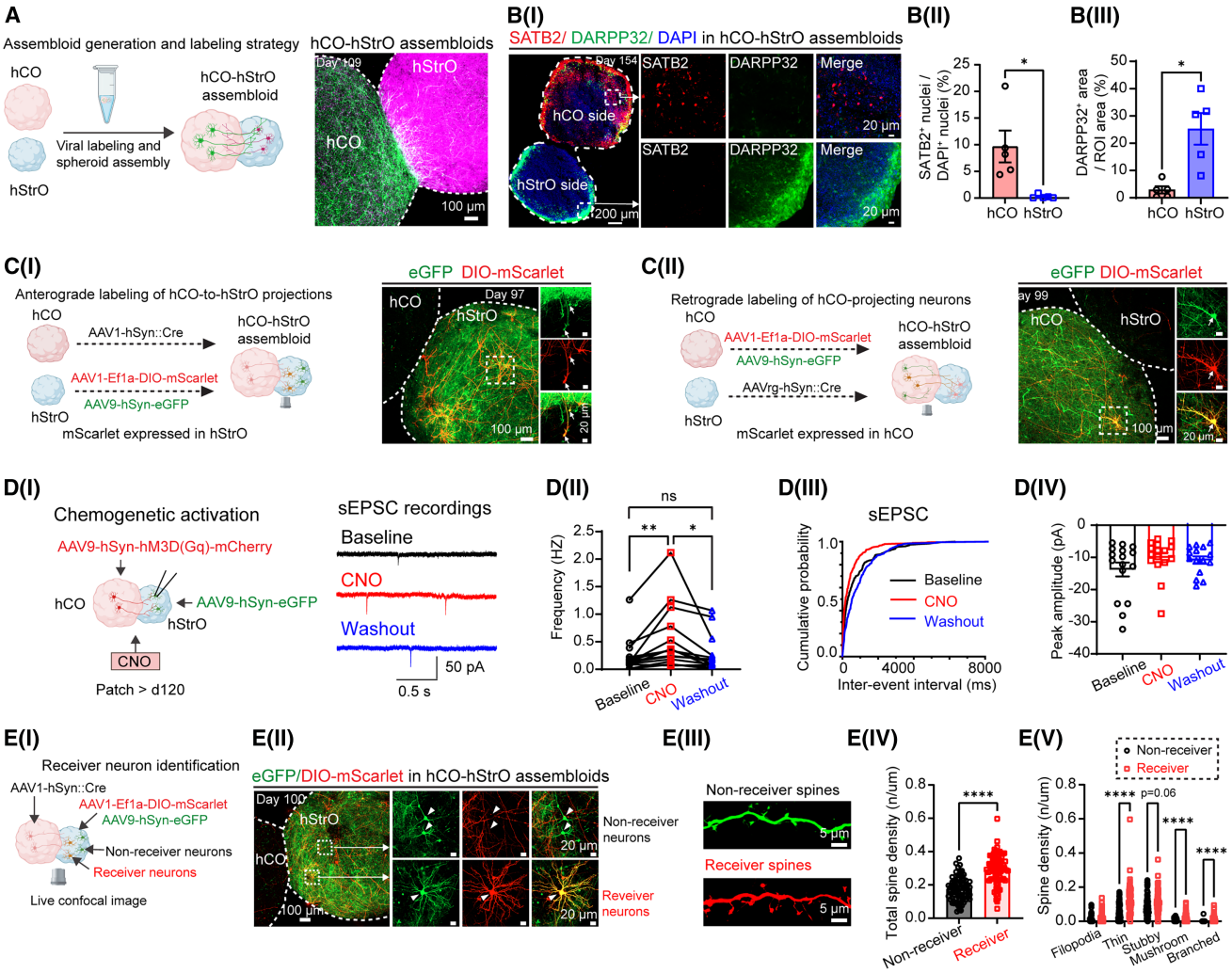


Figure 1. Cortical projections promote striatal synapse formation and function in human cortico-striatal assembloids

(A) Schematic of human cortico-striatal (hCO-hStrO) assembloid generation and representative confocal image of a day 109 assembloid showing the hCO (green) and hStrO (magenta) compartments. Scale bar: 100 μm.

(B) Compartment-enriched marker expression in hCO-hStrO assembloids. (i) Representative images of SATB2 (red), DARPP32 (green), and DAPI (blue) in day 154 assembloids. Dashed outlines mark the hCO and hStrO compartments, and boxed regions indicate matched regions of interest (ROIs) used for high-magnification images and quantification. Scale bars: 200 μm (overview) and 20 μm (magnified images). (ii) Quantification of SATB2$^+$ nuclei among DAPI$^+$ nuclei. (iii) Quantification of DARPP32$^+$ area. n = 5 assembloids from 3 WT hiPSC lines. Paired t test.

(C) Viral tracing of directed hCO-to-hStrO connectivity. (i) Anterograde tracing showing EGFP-labeled hStrO neurons (green) and Cre-dependent mScarlet labeling (red) in receiver neurons. Scale bars: 100 μm (overview) and 20 μm (insets). (ii) Retrograde tracing showing EGFP-labeled cortical neurons (green) and retrogradely labeled mScarlet$^+$ projection neurons (red). Scale bars: 100 μm (overview) and 20 μm (insets). n = 3 assembloids for (i) and n = 4 assembloids for (ii), with similar results from 2 WT hiPSC lines.

(D) Chemogenetic activation of hCO increases excitatory synaptic input onto hStrO neurons. (i) Schematic and representative spontaneous excitatory postsynaptic current (sEPSC) traces recorded from hStrO neurons under baseline, CNO, and washout conditions. (ii) sEPSC frequency. (iii) Cumulative probability plot of sEPSC inter-event intervals. (iv) sEPSC peak amplitude. n = 16 cells from 6 assembloids across 3 WT hiPSC lines. Mixed-effects analysis with Geisser-Greenhouse correction and Tukey's multiple comparisons test for (ii) and (iv).

(E) Receiver striatal neurons exhibit increased dendritic spine density in hCO-hStrO assembloids. (i) Schematic of live-cell imaging of non-receiver and receiver neurons in the hStrO compartment. (ii) Representative neurons. Scale bars: 100 μm (overview) and 20 μm (magnified images). (iii) Representative dendritic spines. Scale bars: 5 μm. (iv) Total spine density. (v) Spine subtype densities. Non-receiver: n = 69 dendrites; receiver: n = 81 dendrites from 9 assembloids across 3 WT hiPSC lines. Welch's t test for (iv) and multiple Mann-Whitney tests with Holm-Šidák correction for (v).

See also Figures S1 and S2. Data are represented as mean ± SEM. ns, not significant; *p < 0.05, **p < 0.01, ***p < 0.001, ****p < 0.0001.

Because cortical glutamatergic projections contribute to striatal MSN maturation,[23] we next examined how cortical input affects striatal synaptic properties. Striatal neurons in hCO-hStrO assembloids exhibited higher EPSC frequency than those in age-matched standalone hStrOs (Figure S2E), suggesting that cortical input enhances striatal synaptic connectivity. We then

Please cite this article in press as: Chen et al., Autism-associated *SCN2A* deficiency disrupts cortico-striatal circuitry in human brain assembloids, Neuron (2026), https://doi.org/10.1016/j.neuron.2026.08.031

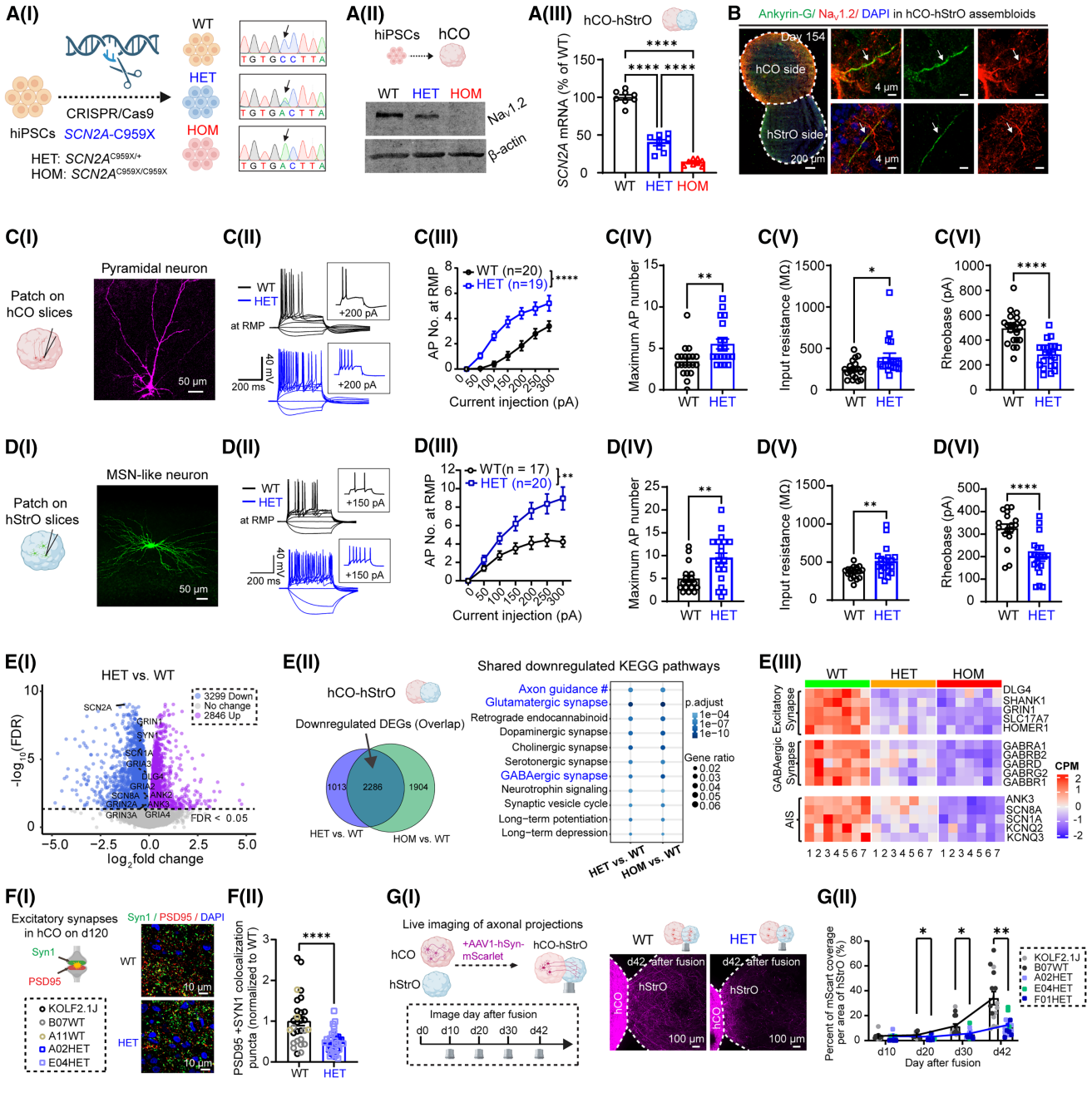


Figure 2. *SCN2A*-C959X increases neuronal excitability and disrupts cortico-striatal connectivity

(A) Validation of isogenic *SCN2A*-C959X hiPSC lines and reduced *SCN2A* expression. (i) CRISPR-Cas9 editing generated heterozygous (HET, $SCN2A^{C959X/+}$) and homozygous (HOM, $SCN2A^{C959X/C959X}$) mutant lines, confirmed by Sanger sequencing. (ii) Western blot of $Na_V1.2$ expression in WT, HET, and HOM hCOs. (iii) *SCN2A* mRNA levels in hCO-hStrO assembloids. $n = 8$ assembloids/group from 3 hiPSC lines; one-way ANOVA with Tukey's test.

(B) Ankyrin-G (green), $Na_V1.2$ (red), and DAPI staining in day 154 hCO-hStrO assembloids showing $Na_V1.2$ localization at the axon initial segment (AIS). Scale bars: 200 μm (overview) and 4 μm (magnified images). $n = 3$ assembloids from 2 hiPSC lines with similar results.

(C) Increased intrinsic excitability of HET cortical neurons in hCO slices. (i and ii) Representative neurobiotin-filled pyramidal-like neuron and firing traces at resting membrane potential (RMP). Scale bar: 50 μm in (i). (iii) Evoked action potential (AP) number across current injections. WT: $n = 20$ cells across 3 hiPSC lines; HET: $n = 19$ cells across 2 hiPSC lines; two-way ANOVA. (iv–vi) Quantification of maximal AP number, input resistance, and rheobase at RMP. Mann-Whitney tests for (iv) and (v); Welch's *t* test for (vi).

(D) Increased intrinsic excitability of HET striatal neurons in hStrO slices. (i and ii) Representative neurobiotin-filled MSN-like neuron and firing traces at RMP. Scale bar: 50 μm in (i). (iii) Evoked AP number. WT: $n = 17$ cells across 2 hiPSC lines; HET: $n = 20$ cells across 2 hiPSC lines; two-way ANOVA. (iv–vi) Maximal AP number, input resistance, and rheobase at RMP. Mann-Whitney tests for (iv) and (v); Welch's *t* test for (vi).

(legend continued on next page)

Please cite this article in press as: Chen et al., Autism-associated *SCN2A* deficiency disrupts cortico-striatal circuitry in human brain assembloids, Neuron (2026), https://doi.org/10.1016/j.neuron.2026.08.031

used dual viral labeling to distinguish striatal neurons receiving direct cortical input ("receiver") from those without detectable input ("non-receiver") (Figure 1Ei). Specifically, hCOs were labeled with AAV1-hSyn::Cre, while hStrOs were labeled with AAV1-Ef1a-DIO-mScarlet and AAV9-hSyn-EGFP. Receiver neurons ($EGFP^+$/$mScarlet^+$) exhibited higher dendritic spine density and a greater proportion of relatively mature spine morphologies than non-receiver neurons ($EGFP^+$ only) (Figures 1Eii–1Ev). Together, these findings show that cortical innervation promotes the functional and structural maturation of striatal neurons, establishing hiPSC-derived cortico-striatal assembloids as a human model for studying circuit assembly and dysfunction in neurodevelopmental disorders.

SCN2A-C959X neurons show enhanced intrinsic excitability

SCN2A is robustly expressed in the cortico-striatal circuitry,[24] which is critically implicated in ASD.[10,11] To investigate how ASD-associated *SCN2A* deficiency affects neuronal function in this circuitry, we introduced the *SCN2A*-C959X mutation, previously identified in children with profound autism,[4,6,7] into KOLF2.1J iPSCs using CRISPR-Cas9 genome editing (Figure 2Ai). Sanger sequencing confirmed the expected C-to-A substitution in heterozygous (HET) and homozygous (HOM) mutant lines, together with isogenic wild-type (WT) controls (Figure 2Ai). Western blotting revealed reduced $Na_V1.2$ protein levels in HET and HOM hCOs (Figure 2Aii), and qPCR further showed a gene-dose-dependent reduction in *SCN2A* mRNA in hCO-hStrO assembloids (Figure 2Aiii), consistent with a LoF/deficiency phenotype.

Previous immunohistological studies in the mouse brain localized the $Na_V1.2$ signal to the AIS, the site of AP initiation.[8] Consistently, $Na_V1.2$ colocalized with the AIS marker ankyrin-G in both hCO and hStrO neurons (Figure 2B). To determine how *SCN2A* deficiency affects AIS organization, we quantified AIS length and found shorter AISs in *SCN2A*-C959X HET neurons in hCO slices than in WT neurons (Figure S3D), indicating altered AIS structural organization. Given the role of the AIS in regulating neuronal output,[25–27] we next examined intrinsic excitability. Unexpectedly, whole-cell patch-clamp recordings revealed enhanced firing in *SCN2A*-deficient cortical pyramidal-like and striatal MSN-like neurons relative to WT controls, with elevated maximum evoked firing number, increased input resistance, and reduced rheobase for AP generation (Figures 2C, 2D, and S3A). These changes were accompanied by reduced AP amplitude and membrane capacitance, indicating altered AP waveform and passive membrane properties (Figures S3A–S3C). Together, these results indicate that *SCN2A* deficiency alters AIS organization and remodels intrinsic neuronal output in both cortical and striatal neurons.

SCN2A-C959X impairs excitatory synaptogenesis and long-range cortico-striatal projections

To gain insight into molecular alterations associated with *SCN2A* deficiency, we conducted bulk RNA sequencing (RNA-seq) of hCO-hStrO assembloids (Figure S3Ei). Consistent with our genetic and protein analyses, *SCN2A* expression was significantly reduced in mutant assembloids (Figure S3Ei). We identified 6,145 differentially expressed genes (DEGs) in *SCN2A*-C959X HET versus WT assembloids (2,846 upregulated; 3,299 downregulated; Figure 2Ei) and 8,907 DEGs in HOM versus WT assembloids (4,717 upregulated; 4,190 downregulated; Figure S3Eii). We then focused on overlapping DEGs shared between HET and HOM groups, as these changes may represent core transcriptional alterations associated with *SCN2A* deficiency. Kyoto Encyclopedia of Genes and Genomes (KEGG) analysis of 2,286 overlapping downregulated genes revealed enrichment in axon guidance, synaptic signaling, and neuronal connectivity pathways, including genes involved in AIS organization, ion channels, and excitatory synapses, such as *ANK3* (encoding ankyrin-G) and *DLG4* (encoding postsynaptic density protein 95 [PSD95]) (Figures 2Eii, 2Eiii, S3Eiii, and S3Eiv). Overlapping upregulated genes were enriched in RNA-processing and nonsense-mediated decay pathways (Figures S3Ev and S3Evi), consistent with the premature stop codon. These transcriptomic signatures suggested broad alterations in axonal and synaptic programs in *SCN2A*-deficient assembloids, prompting us to examine excitatory synapse formation and long-range cortical projections.

To assess excitatory synapse formation, we labeled presynaptic terminals with synapsin 1 (Syn1) and postsynaptic sites with PSD95. Compared with WT controls, *SCN2A*-C959X HET neurons showed substantially reduced $Syn1^+$/$PSD95^+$ colocalization, indicating impaired excitatory synapse formation or maintenance (Figure 2F). To assess long-range cortico-striatal projection development, we performed longitudinal live-cell imaging to track cortical axonal projections into the striatal compartment. In WT assembloids, we observed a progressive increase in unidirectional $mScarlet^+$ projections from hCOs into hStrOs after fusion (Figures 2Gi and S3F). *SCN2A*-C959X HET assembloids also showed increasing cortical axonal projections over time, indicating ongoing projection growth; however, projection coverage within hStrOs remained lower than WT at days 20, 30, and 42 after fusion (Figure 2Gii). These results show that *SCN2A* deficiency impairs excitatory synaptogenesis and long-range cortico-striatal projection maturation.

(E) Transcriptomic alterations in *SCN2A*-mutant hCO-hStrO assembloids. (i) Volcano plot of differentially expressed genes (DEGs) in HET versus WT assembloids. (ii) Overlap of downregulated genes in HET and HOM assembloids, with KEGG enrichment of shared downregulated genes. (iii) Heatmap of the top 5 representative genes associated with excitatory synapses, GABAergic synapses, and the AIS. $n = 7$ assembloids per genotype from 3 hiPSC lines and 2 independent differentiation batches; false discovery rate (FDR) < 0.05, Benjamini-Hochberg correction.

(F) Reduced excitatory synapse formation in HET hCOs. (i) Syn1 (green, presynaptic), PSD95 (red, postsynaptic), and DAPI (blue) staining in day 120 hCOs. Scale bars: 10 μm. (ii) $PSD95^+$/$Syn1^+$ colocalized puncta normalized to WT. WT: $n = 29$ images from 9 organoids across 3 hiPSC lines; HET: $n = 37$ images from 10 organoids across 2 hiPSC lines. Mann-Whitney test.

(G) Reduced cortical axonal projection into the striatal compartment in HET assembloids. (i) Schematic of mScarlet labeling and imaging timeline, and representative images on day 42 after fusion. Scale bars: 100 μm. (ii) Quantification of $mScarlet^+$ coverage in hStrO from days 10 to 42. WT: $n = 15$ assembloids from 2 lines; HET: $n = 16$ assembloids from 3 lines. Mixed-effects analysis with Geisser-Greenhouse correction and Šídák's test.

See also Figure S3. Data are represented as mean ± SEM. $^*p < 0.05$, $^{**}p < 0.01$, $^{***}p < 0.001$, $^{****}p < 0.0001$.

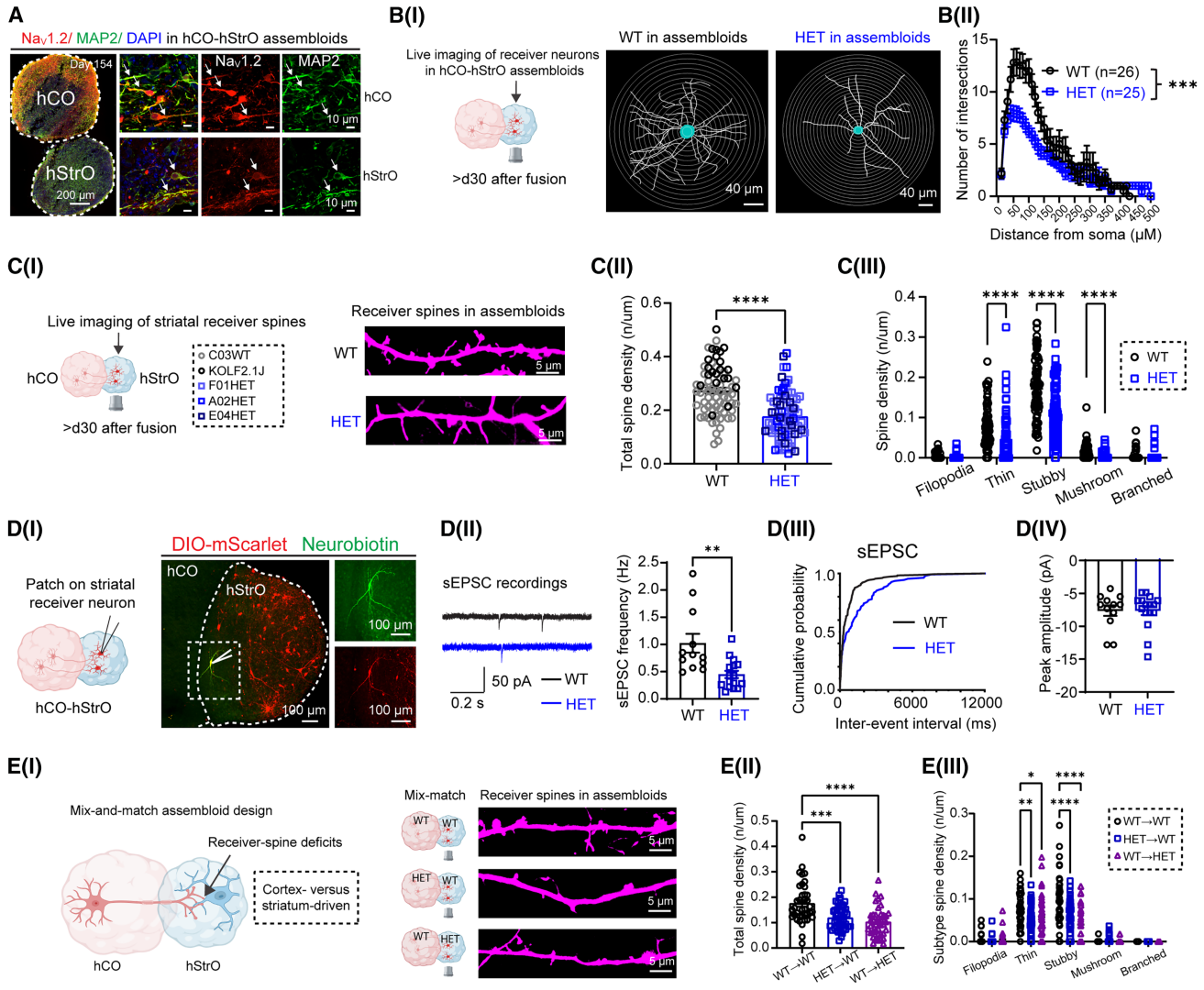


Figure 3. *SCN2A*-C959X reduces dendritic complexity, spine density, and excitatory synaptic input in striatal receiver neurons

HET denotes the heterozygous *SCN2A*-C959X line throughout this figure.

(A) Immunostaining for Na$_V$1.2 (red), MAP2 (green), and DAPI (blue) in day 154 hCO-hStrO assembloids, showing Na$_V$1.2 localization in neuronal processes within the hCO and hStrO compartments. Scale bars: 200 μm (overview) and 10 μm (magnified images). n = 3 assembloids from 2 hiPSC lines with similar results.

(B) Reduced dendritic complexity of HET striatal receiver neurons. (i) Live-cell imaging strategy and representative reconstructions of WT and HET receiver neurons >30 days after fusion. Scale bars: 40 μm. (ii) Sholl analysis of dendritic intersections. WT: n = 26 neurons across 4 hiPSC lines; HET: n = 25 neurons across 3 hiPSC lines; two-way ANOVA.

(C) Reduced dendritic spine density of HET striatal receiver neurons. (i) Live imaging strategy and representative dendritic segments. Scale bars: 5 μm. (ii) Total spine density. WT: n = 74 dendrites from 9 assembloids across 3 hiPSC lines; HET: n = 86 dendrites from 9 assembloids across 3 hiPSC lines. Welch's t test. (iii) Spine subtype densities. Same sample sizes as in (ii). Multiple Mann-Whitney tests with Holm-Šidák correction.

(D) Reduced excitatory synaptic input onto HET striatal receiver neurons. (i) Schematic of patch-clamp recording and image of a DIO-mScarlet-labeled receiver neuron filled with neurobiotin. Scale bars: 100 μm. (ii) Representative sEPSC traces and sEPSC frequency. WT: n = 12 cells from 7 assembloids across 2 hiPSC lines; HET: n = 16 cells from 7 assembloids across 2 hiPSC lines. Unpaired t test. (iii) Cumulative probability plot of sEPSC inter-event intervals. (iv) sEPSC peak amplitude. Same sample sizes as in (ii). Unpaired t test.

(E) Mix-and-match assembloids reveal cortical and striatal contributions to receiver-neuron spine defects. (i) Strategy and representative receiver dendritic segments from WT→WT, HET→WT, and WT→HET assembloids. Scale bars: 5 μm. (ii) Total spine density. WT→WT: n = 38 dendrites from 10 assembloids; HET→WT: n = 46 dendrites from 14 assembloids; WT→HET: n = 41 dendrites from 11 assembloids. One-way ANOVA with Dunnett's test. (iii) Spine subtype densities. Same sample sizes as in (ii). Two-way ANOVA with Šídák's test.

See also Figure S4. Data are represented as mean ± SEM. *p < 0.05, **p < 0.01, ***p < 0.001, ****p < 0.0001.

Please cite this article in press as: Chen et al., Autism-associated *SCN2A* deficiency disrupts cortico-striatal circuitry in human brain assembloids, Neuron (2026), https://doi.org/10.1016/j.neuron.2026.08.031

CellPress

SCN2A-C959X disrupts the cortico-striatal circuit in assembloids

In addition to its AIS localization, studies in the mouse brain suggest that $Na_V1.2$ is also present in somatodendritic compartments.[9] Consistently, $Na_V1.2$ immunoreactivity colocalized with somata ($NeuN^+$) and dendrites (microtubule-associated protein 2 $[MAP2]^+$) in both hCO and hStrO compartments, with a higher normalized $Na_V1.2$ signal in hCOs (Figures 3A and S4A). This somatodendritic distribution raised the possibility that *SCN2A* deficiency affects not only cortical axonal projections but also striatal receiver-neuron maturation. To test this, we analyzed hStrO receiver neurons innervated by cortical input using dual AAV labeling. Before fusion, hCOs were transduced with AAV1-hSyn::Cre and hStrOs with AAV1-Ef1a-DIO-mScarlet. One month after fusion, Sholl analysis revealed reduced dendritic complexity in *SCN2A*-C959X HET receiver neurons ($mScarlet^+$), including shorter dendritic length and fewer dendritic intersections (Figures 3B, S4Bi, and S4Bii).

We next characterized dendritic spines, the primary sites of excitatory synaptic input, in live hCO-hStrO assembloids. *SCN2A*-C959X HET receiver neurons ($mScarlet^+$) exhibited reduced spine density, with thin, stubby, and mature mushroom spines particularly affected (Figure 3C). Whole-cell patch-clamp recordings from receiver neurons ($mScarlet^+$) in assembloid slices further revealed decreased EPSC frequency in *SCN2A*-C959X HET neurons (Figures 3Di–3Div), indicating weakened excitatory synaptic transmission. Notably, the same receiver-neuron population showed increased intrinsic firing (Figure S4C), consistent with the enhanced excitability observed in standalone hStrO preparations (Figure 2D). Post hoc reconstruction of recorded neurons further confirmed reduced dendritic spine density (Figure S4D).

To determine whether receiver-neuron spine defects arise from cortical projection abnormalities, intrinsic striatal vulnerability, or both, we generated genotype-defined mix-and-match assembloids (Figure 3Ei). Both HET-to-WT and WT-to-HET assembloids showed reduced receiver-neuron spine density relative to WT-to-WT controls, indicating contributions from both mutant cortical input and intrinsic striatal vulnerability (Figures 3Eii and 3Eiii).

We further examined assembloids carrying the *SCN2A*-C959X HOM mutation and observed similar phenotypes, including impaired cortical axonal projections (Figure S3G) and reduced spine density (Figures S4Biii and S4Biv). Collectively, these findings demonstrate that *SCN2A*-C959X disrupts cortico-striatal circuit assembly through both presynaptic cortical projection deficits and postsynaptic striatal receiver-neuron abnormalities, leading to impaired excitatory synaptic structure and function.

An independent *SCN2A*-R524X mutation increases neuronal firing and disrupts cortico-striatal connectivity

To determine whether the circuit abnormalities observed in *SCN2A*-C959X assembloids extend to an independent, clinically observed *SCN2A* PTV, we examined assembloids carrying *SCN2A c.1570C>T* (p.Arg524Ter; R524X).[28] Similar to C959X, R524X neurons showed decreased $Na_V1.2$ protein expression and increased intrinsic firing relative to WT controls (Figures 4A and 4B), indicating a shared neuronal phenotype across independent *SCN2A* LoF variants.

We next assessed cortico-striatal circuit assembly in R524X assembloids. Longitudinal imaging revealed diminished cortical axonal projections into the striatal compartment compared with WT assembloids (Figure 4C), indicating impaired long-range cortico-striatal connectivity. Consistent with this projection deficit, R524X HET-to-HET assembloids exhibited lower receiver-neuron spine density than WT-to-WT controls (Figure 4D). Genotype-defined mix-and-match assembloids further revealed reduced spine density in both HET-to-WT and WT-to-HET combinations, indicating contributions from both mutant cortical input and intrinsic striatal vulnerability (Figure 4D).

Together, these results show that an independent *SCN2A* PTV recapitulates several major abnormalities observed in *SCN2A*-C959X assembloids, including neuronal hyperexcitability, impaired cortical axonal projection, and reduced receiver-neuron spine density. These findings support human cortico-striatal circuit dysfunction as a reproducible consequence of *SCN2A* deficiency.

CAV-2-mediated delivery of human *SCN2A* normalizes neuronal hyperexcitability and rescues spine density in cortico-striatal assembloids

Gene replacement represents a promising therapeutic strategy for disorders caused by LoF mutations. To test the feasibility of this approach for *SCN2A* deficiency, we created CAV-*SCN2A*, a CAV-2 vector capable of delivering a full-length codon-optimized human *SCN2A* expression cassette (Figure 5Ai). A C-terminal hemagglutinin (HA) tag was included to distinguish exogenous from endogenous $Na_V1.2$ and was previously shown not to affect sodium channel activity.[29] Biophysical recordings further confirmed that HA tagging did not alter $Na_V1.2$ current density or activation and inactivation properties compared with untagged $Na_V1.2$ (Figure S5A).

We next evaluated CAV-*SCN2A* expression in *SCN2A*-C959X HET assembloids by treating them with CAV-*SCN2A* or a control vector expressing mCitrine (CAV-Ctrl). qPCR using primers selective for codon-optimized *SCN2A* or total *SCN2A* confirmed increased exogenous (optimized) and total *SCN2A* transcripts following CAV-*SCN2A* treatment (Figure 5A). Western blotting further showed restoration of $Na_V1.2$ protein toward WT levels (Figure 5B). In hCO-derived monolayer neurons (>110 days old), HA-tagged $Na_V1.2$ colocalized with the AIS marker ankyrin-G, supporting appropriate localization of exogenous $Na_V1.2$ (Figure 5C). Together, these results validate CAV-*SCN2A*-mediated expression and localization of human $Na_V1.2$.

We then asked whether restoring $Na_V1.2$ expression could mitigate neuronal hyperexcitability in *SCN2A*-deficient neurons. Whole-cell patch-clamp recordings from $mCitrine^+$ neurons in *SCN2A*-C959X HET cultures co-treated with CAV-*SCN2A* and CAV-Ctrl showed reduced excessive AP firing, decreased input resistance, and a shift in rheobase toward WT levels (Figure 5D). $Na_V1.2$ restoration also increased spine density in striatal receiver neurons approaching WT levels, with recovery of thin and stubby spines (Figure 5E). However, $mScarlet^+$ receiver-neuron coverage within the hStrO compartment remained unchanged (Figure S5B). Because this measure reflects the extent of striatal neuron engagement by long-range cortical inputs, these findings suggest that CAV-*SCN2A* preferentially improved

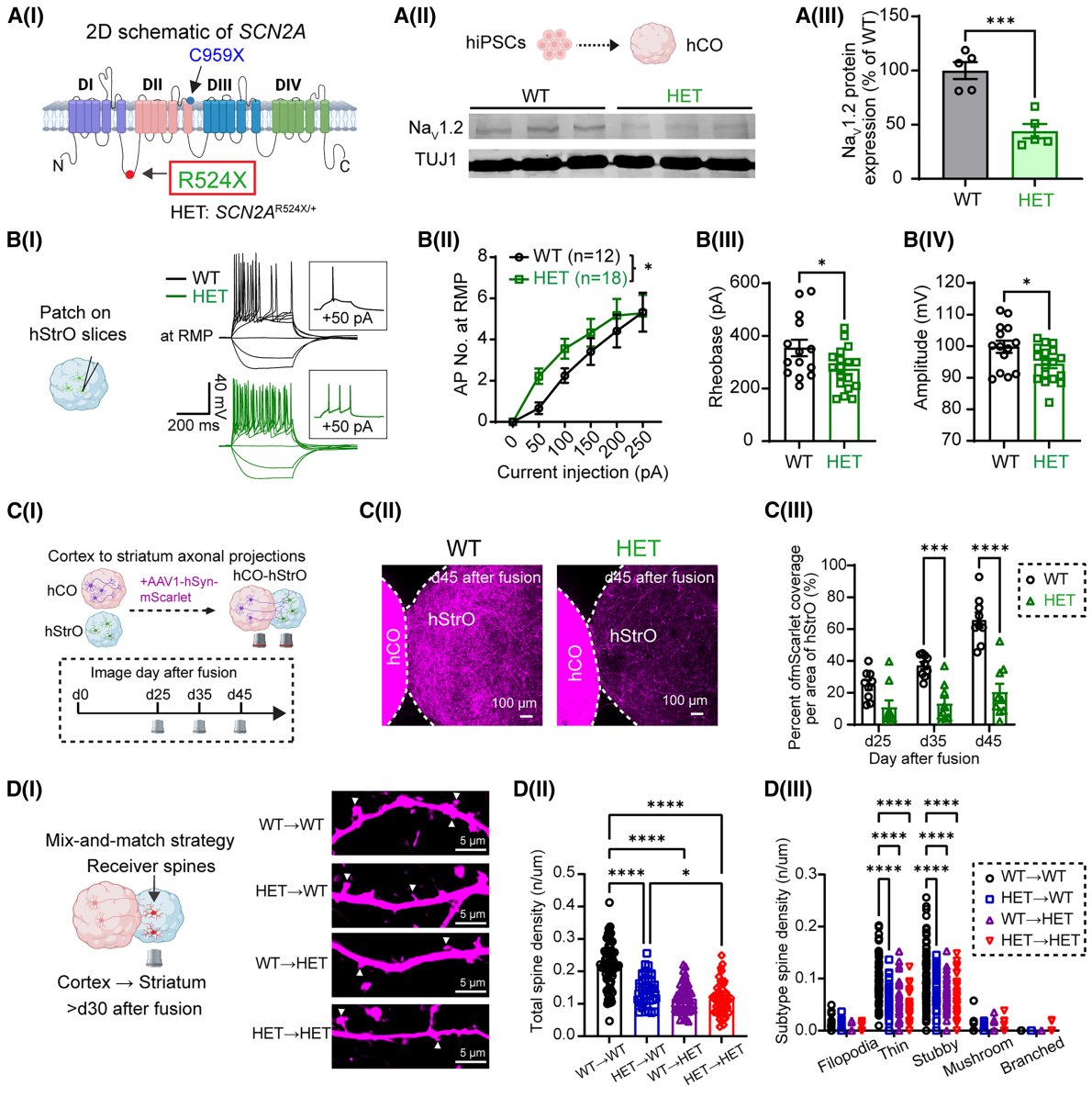


Figure 4. An independent *SCN2A*-R524X mutation increases neuronal excitability and disrupts cortico-striatal connectivity

HET denotes the heterozygous *SCN2A*-R524X line throughout this figure.

(A) Validation of the independent *SCN2A*-R524X HET line. (i) Schematic of $Na_V1.2$ showing the positions of C959X and R524X variants. (ii) Immunoblot of $Na_V1.2$ in WT and HET hCOs, with class III β-tubulin (detected using TUJ1) as a neuronal loading control. (iii) $Na_V1.2$ protein expression normalized to WT. $n = 5$ hCOs per group; Welch's t test.

(B) Increased intrinsic excitability of HET striatal neurons in hStrO slices. (i) Whole-cell patch-clamp recording from hStrO slices at >120 days and representative firing traces at RMP. (ii) Evoked AP number across current injections. WT: $n = 12$ cells from 4 organoids across 3 hiPSC lines; HET: $n = 18$ cells from 4 organoids from 1 hiPSC line; two-way ANOVA. (iii and iv) Rheobase and AP amplitude at RMP; unpaired t test.

(C) Reduced cortical axonal projection into the striatal compartment in HET assembloids. (i) mScarlet labeling strategy and imaging timeline after hCO-hStrO fusion. (ii and iii) Representative images and mScarlet$^+$ coverage within the hStrO on days 25, 35, and 45. Scale bars: 100 µm in (ii). WT: $n = 9$ assembloids across 2 WT lines; HET: $n = 9$ assembloids from 1 line; two-way ANOVA with Šídák's test.

(D) Mix-and-match assembloids reveal cortical and striatal contributions to receiver spine defects. (i) Strategy and representative receiver dendritic segments from WT→WT, HET→WT, WT→HET, and HET→HET assembloids. Scale bars: 5 µm. (ii) Total spine density. WT→WT: $n = 68$ dendrites from 10 assembloids; HET→WT: $n = 41$ dendrites from 7 assembloids; WT→HET: $n = 51$ dendrites from 10 assembloids; HET→HET: $n = 52$ dendrites from 9 assembloids; one-way ANOVA with Tukey's test. (iii) Spine subtype densities. Same n as in (ii). Two-way ANOVA with Šídák's test.

Data are represented as mean ± SEM. $^*p < 0.05$, $^{**}p < 0.01$, $^{***}p < 0.001$, $^{****}p < 0.0001$.

Please cite this article in press as: Chen et al., Autism-associated *SCN2A* deficiency disrupts cortico-striatal circuitry in human brain assembloids, Neuron (2026), https://doi.org/10.1016/j.neuron.2026.08.031

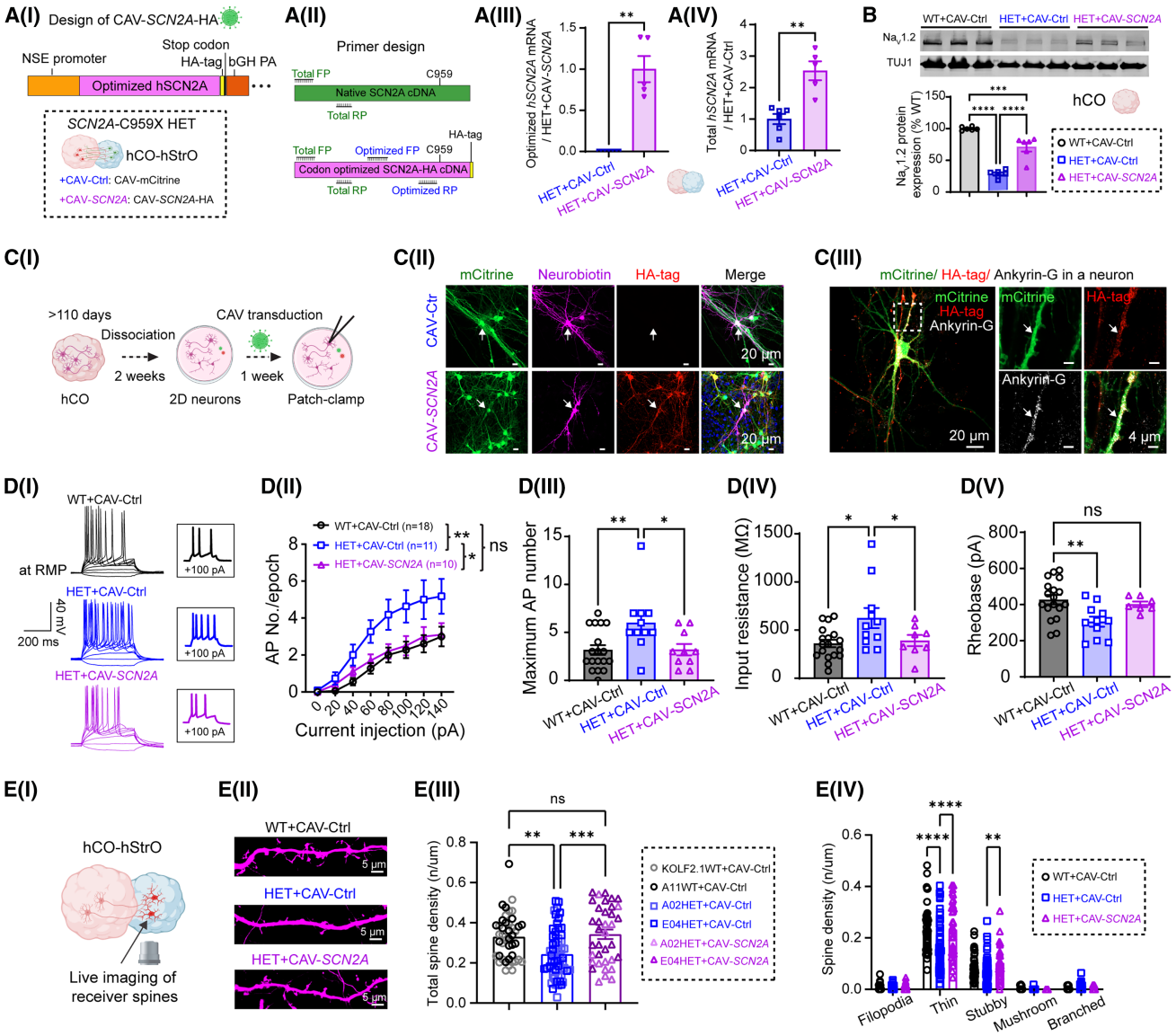


Figure 5. Exogenous *SCN2A* expression via CAV-2 delivery mitigates hyperexcitability and increases spine density

HET denotes the heterozygous *SCN2A*-C959X line throughout this figure.

(A) Design and validation of CAV-*SCN2A* rescue vector. (i) Schematic of codon-optimized human *SCN2A* with a C-terminal HA-tag delivered by CAV-2 to HET hCO-hStrO assembloids, with CAV-mCitrine as control. (ii) Primer design to distinguish total and codon-optimized *SCN2A* transcripts. (iii) Codon-optimized exogenous *hSCN2A* mRNA; Welch's *t* test. (iv) Total *hSCN2A* mRNA; unpaired *t* test. HET+CAV-Ctrl: $n = 6$ assembloids, HET+CAV-*SCN2A*: $n = 5$ assembloids.

(B) *hSCN2A* restoration partially rescues $Na_V1.2$ protein in HET hCOs. Immunoblot of $Na_V1.2$ in WT+CAV-Ctrl, HET+CAV-Ctrl, and HET+CAV-*SCN2A* hCOs, with TUJ1 as a loading control. $n = 6$ hCOs per group; one-way ANOVA with Tukey's test.

(C) Expression and localization of CAV-*SCN2A*-HA-encoded HA-tagged $Na_V1.2$ in dissociated cortical neurons. (i) Experimental timeline. (ii) mCitrine, neurobiotin, and HA-tag staining showing expression of CAV-Ctrl and CAV-*SCN2A* in patched neurons. Scale bars: 20 μm. (iii) HA-tag colocalization with ankyrin-G at the axon initial segment (AIS). Scale bars: 20 μm (overview) and 4 μm (magnified images).

(D) CAV-*SCN2A* mitigates increased repetitive firing in HET cortical neurons at RMP. (i) Representative current-clamp traces. (ii) Evoked AP number across current injections. WT+CAV-Ctrl: $n = 18$ cells; HET+CAV-Ctrl: $n = 11$ cells; HET+CAV-*SCN2A*: $n = 10$ cells; two-way ANOVA with Tukey's test. (iii–v) Maximal AP number, input resistance, and rheobase; one-way ANOVA with Holm-Šídák's test.

(E) CAV-*SCN2A* increases receiver spine density in HET hCO-hStrO assembloids. (i and ii) Live imaging strategy and representative dendritic segments. Scale bars: 5 μm. (iii) Total spine density. WT+CAV-Ctrl: $n = 43$ dendrites from 12 assembloids; HET+CAV-Ctrl: $n = 60$ dendrites from 14 assembloids; HET+CAV-*SCN2A*: $n = 36$ dendrites from 14 assembloids; one-way ANOVA with Tukey's test. (iv) Spine subtype densities. Same *n* as in (iii). Two-way ANOVA with Tukey's test.

See also Figure S5. Data are represented as mean ± SEM. ns, not significant; $^*p < 0.05$, $^{**}p < 0.01$, $^{***}p < 0.001$, $^{****}p < 0.0001$.

Please cite this article in press as: Chen et al., Autism-associated *SCN2A* deficiency disrupts cortico-striatal circuitry in human brain assembloids, Neuron (2026), https://doi.org/10.1016/j.neuron.2026.08.031

spine maturation without detectably expanding cortico-striatal engagement in this assay. To assess the impact of *SCN2A* restoration on population-level spontaneous activity, we performed multielectrode array (MEA) recordings. *SCN2A*-C959X HET + CAV-Ctrl assembloids showed elevated network firing compared with WT controls, whereas CAV-*SCN2A* treatment normalized this hyperactivity (Figure S5C). Together, these findings demonstrate that targeted *SCN2A* restoration mitigates morphological and electrophysiological deficits in *SCN2A*-deficient human assembloids, supporting the therapeutic potential of the gene replacement approach. Notably, *SCN2A* overexpression in WT neurons increased excitability (Figure S5D), highlighting the importance of precise regulation and dose optimization for future clinical translation.

DISCUSSION

ASD is a complex neurodevelopmental condition, and defining the molecular and circuit-level consequences of monogenic causes such as *SCN2A* can provide valuable insight into disease pathophysiology. Here, we used human cortico-striatal assembloids to investigate how *SCN2A* PTVs alter neuronal function and circuit connectivity. We found that *SCN2A* deficiency impaired cortical axonal projections, striatal receiver dendritic and spine maturation, and excitatory synaptic transmission while increasing intrinsic neuronal firing. These abnormalities were observed in *SCN2A*-C959X assembloids and recapitulated by the independent *SCN2A*-R524X variant, supporting cortico-striatal circuit dysfunction as a reproducible consequence of *SCN2A* LoF. Importantly, leveraging the large cargo capacity of CAV-2, we delivered full-length human *SCN2A* and mitigated several morphological and electrophysiological deficits, supporting CAV-2-mediated gene replacement as a potential therapeutic strategy for *SCN2A*-related neurodevelopmental disorders.

$Na_V1.2$ plays multiple roles in neurons: it is enriched at the AIS and axons, where it contributes to AP initiation and propagation, but also extends into somatodendritic compartments, where it can regulate dendritic excitability and AP backpropagation.[8,9] Consistently, $Na_V1.2$ colocalized with ankyrin-G at the AIS, NeuN in neuronal somata, and MAP2 in dendrites in human cortico-striatal assembloids (Figures 2 and S4). This broad distribution suggests that *SCN2A* deficiency is unlikely to produce a single compartment-restricted defect. Indeed, *SCN2A* PTVs disrupted cortical axonal projections into the striatal compartment and reduced dendritic complexity, spine density, and synaptic transmission in striatal receiver MSN-like neurons (Figures 2, 3, and 4). However, these phenotypes alone could not distinguish whether receiver-neuron spine defects arose from impaired cortical input, intrinsic striatal vulnerability, or both. Our genotype-defined mix-and-match assembloids suggested contributions from both brain regions to these spine defects. Because cortical projection and EPSC analyses were not performed across all genotype-mixing conditions, the corresponding functional deficits remain to be established. Although our *ANK3*/ankyrin-G analysis focused on AIS length and did not directly assess ankyrin localization at $PSD95^+$ synapses,[9] reduced $PSD95^+$ synaptic puncta and EPSC frequency indicate broader impairment of excitatory synaptic structure and function. Such defects may involve downstream postsynaptic mechanisms, including dendritic ankyrins such as *ANK2* or shorter *ANK3* isoforms.[30]

Our findings also reveal a complex relationship between AIS structure and intrinsic excitability. *SCN2A*-C959X cortical neurons exhibited shortened ankyrin-G-defined AISs, which might be expected to reduce excitability because longer AISs are often associated with greater sodium conductance and lower AP threshold.[27] Nevertheless, *SCN2A*-deficient cortical and striatal neurons, including cortical input-receiving striatal neurons, displayed enhanced intrinsic firing (Figures 2 and S4). The counterintuitive hyperexcitability was accompanied by reduced rheobase and AP amplitude and transcriptional downregulation of potassium channel genes (Figure S3). These observations suggest that compensatory ion-channel remodeling and altered membrane properties may outweigh reduced $Na_V1.2$ expression and shift neurons toward increased firing, consistent with our previous work in *Scn2a*-deficient mice.[24] Notably, the same receiver-neuron population showed both reduced excitatory synaptic input and increased intrinsic firing, indicating that impaired synaptic communication and enhanced intrinsic excitability can coexist. MEA recordings similarly revealed elevated spontaneous network firing in *SCN2A*-C959X assembloids despite weakened excitatory transmission, and this phenotype was partially normalized by CAV-*SCN2A* (Figure S5C). These network changes may reflect compensatory remodeling or transcriptional dysregulation of excitatory and inhibitory signaling pathways (Figure 2), consistent with our previous finding that *Scn2a*-deficient mice show both synaptic impairments and enhanced neuronal firing *in vivo*.[31] Future studies comparing receiver and non-receiver striatal neurons and manipulating candidate potassium channels or AIS components will clarify how cortical innervation and ion-channel remodeling shape excitability in *SCN2A*-deficient circuits. They could also determine whether circuit-level deficits in axonal projection, spine maturation, and synaptic transmission are more closely linked to ASD pathogenesis than intrinsic excitability alone, and whether impaired neuronal communication drives compensatory increases in intrinsic firing.

The phenotypes captured in our study highlight the value of human 3D models for studying *SCN2A* deficiency. In our brain organoids and assembloids, HET *SCN2A* nonsense mutations that reduced *SCN2A* expression by approximately 50% were sufficient to increase neuronal firing. By contrast, mouse models may require a greater reduction in *Scn2a* expression to reveal a similar phenotype.[24,32] Human 3D models can also mature over extended periods (hundreds of days), allowing neurons to develop more complex morphologies[33] and electrophysiological properties[34] that more closely approximate physiological conditions.[35] Extended maturation may therefore contribute to differences from 2D-cultured $SCN2A^{+/-}$ hiPSC-derived neurons, in which increased AIS length and reduced neuronal excitability were reported.[36] Because monolayer cultures often represent relatively earlier developmental stages,[37] human 3D models may uncover disease phenotypes not readily detected in less mature systems.

Nevertheless, our hStrO model should not be interpreted as a fully mature or highly purified MSN system. MSN-like cells represented only a subset of the hStrO population, alongside other neuronal, progenitor, and glial populations. Although hStrOs

Please cite this article in press as: Chen et al., Autism-associated *SCN2A* deficiency disrupts cortico-striatal circuitry in human brain assembloids, Neuron (2026), https://doi.org/10.1016/j.neuron.2026.08.031

showed striatal regional identity at the marker and organoid-compartment levels, recorded neurons did not yet display fully mature MSN-defining intrinsic electrophysiological features. Accordingly, the transcriptomic, imaging, and electrophysiological phenotypes reported here should be interpreted within an immature MSN-containing striatal organoid system rather than as definitive abnormalities of mature MSNs.

SCN2A mutations in patients are HET. The *SCN2A*-C959X nonsense mutation introduces a premature stop codon that likely triggers nonsense-mediated decay,[7,38] resulting in reduced *SCN2A* expression and haploinsufficiency. Consistent with this interpretation, mutant assembloids showed reduced *SCN2A* mRNA and $Na_V1.2$ protein levels (Figure 2), and RNA-seq revealed enrichment of RNA-processing and nonsense-mediated decay pathways (Figure S3). These findings support loss of expression from the mutant allele, leaving insufficient total *SCN2A* dosage as a major pathogenic mechanism for the PTVs modeled here. However, *SCN2A* LoF variants may act through distinct mechanisms depending on variant class. Some missense variants, for example, may exert dominant-negative effects by producing mutant proteins that interfere with WT $Na_V1.2$ function.[39–41] The *SCN2A*-C959X HOM model does not reproduce the HET state observed in patients but provides an extreme *SCN2A*-deficiency condition for examining gene dose-dependent $Na_V1.2$ functions in human neurons and circuits.

AAV is widely used for approved gene therapies, but its limited genome capacity (~4.7 kb)[42] precludes the delivery of large genes such as the full-length *SCN2A* (~6.0 kb) in a single vector. Alternatively, CAV-2 vectors can accommodate substantially larger transgenes (~34 kb) and support neuronal transgene expression.[29] Leveraging this capacity, we delivered codon-optimized human *SCN2A* and mitigated key *SCN2A*-C959X-associated deficits in human brain assembloids, including reduced dendritic spine density and elevated intrinsic and network firing. These findings extend the utility of human assembloids from disease modeling to evaluating the reversibility of circuit-level phenotypes. Together with our recent mouse study showing that regional *Scn2a* restoration, achieved by removing the gene trap, reduces ASD-associated phenotypes in *Scn2a*-deficient mice,[31] these studies support the therapeutic potential of restoring *SCN2A* function across species and model systems. However, *SCN2A* overexpression in WT neurons increased excitability, emphasizing the need for precise dose control. Future studies should define therapeutic expression windows, optimize cell-type-specific and developmentally timed delivery, and evaluate the efficacy and safety of CAV-*SCN2A* *in vivo*.

In summary, our study demonstrates that the ASD-causing *SCN2A* PTVs disrupt human cortico-striatal circuit assembly by impairing cortical axonal projections and cortico-striatal synaptic connectivity, while increasing intrinsic and network firing. The successful rescue of these deficits through targeted *SCN2A* restoration highlights the potential of gene replacement therapy for monogenic ASD. Conceptually, our work advances beyond prior *Scn2a* mouse model studies by directly linking human-relevant neural circuitry disruptions with functional outcomes relevant to human pathology. More broadly, these findings underscore the power of human brain organoids/assembloids in modeling neurodevelopmental disorders and advancing precision medicine approaches, laying a foundational framework applicable to other monogenic ASDs.[43]

RESOURCE AVAILABILITY

Lead contact

Requests for further information and resources should be directed to and will be fulfilled by the lead contact, Yang Yang (yangyang@purdue.edu).

Materials availability

The gene-edited *SCN2A*-C959X and *SCN2A*-R524X hiPSC lines, including the corresponding isogenic WT control lines generated in this study, are available from the lead contact upon reasonable request and completion of a material transfer agreement. CAV-2-NSE-*SCN2A*-HA and the corresponding expression cassette are available from the lead contact upon reasonable request, subject to a material transfer agreement and restrictions related to a pending patent application. CAV-2-NSE-mCitrine and the *hSCN2A*-HA plasmid generated in this study are available from the lead contact upon reasonable request and completion of a material transfer agreement.

Data and code availability

- The bulk RNA sequencing and Xenium spatial transcriptomic datasets generated in this study have been deposited in the Gene Expression Omnibus (GEO) under accession numbers GEO: GSE330433 and GEO: GSE343854, respectively, and are publicly available as of the date of publication.
- Custom analysis scripts have been deposited and are publicly available at Zenodo: https://doi.org/10.5281/zenodo.22031620.
- Any additional information required to reanalyze the data reported in this paper is available from the lead contact upon request.

ACKNOWLEDGMENTS

Research reported in this publication was partially supported by the National Institute of Neurological Disorders and Stroke of the National Institutes of Health under award numbers R01NS117585, R01NS123154, and R56NS144233 to Y.Y. The authors gratefully acknowledge support from the Purdue Institute for Drug Discovery and the Purdue Institute for Integrative Neuroscience. X.C. was supported by the AES Postdoctoral Research Fellowship. J.Z. was supported by the Uplifting Athletes Young Investigator Draft grant. The Yang lab is grateful to the FamilieSCN2A Foundation for the Hodgkin-Huxley Research Award to Y.Y. and support from the Action Potential Grant to X.C., J.Z., and Y.-E.Y. The Yang lab appreciates the bioinformatics support of the Collaborative Core for Cancer Bioinformatics (C^3B) with support from the Indiana University Simon Comprehensive Cancer Center (grant P30CA082709), the Purdue Institute for Cancer Research (grant P30CA023168), and the Walther Cancer Foundation. The content is solely the responsibility of the authors and does not necessarily represent the official views of the sponsors.

AUTHOR CONTRIBUTIONS

X.C., J.Z., and Y.Y. conceived the study and designed the experiments. X.C. generated the organoids and cortico-striatal assembloids and led the viral tracing, CAV-2 rescue, imaging and morphometric analyses, and molecular, transcriptomic, and MEA experiments. J.Z. led the patch-clamp studies of intrinsic excitability and synaptic connectivity. M.J.R. contributed to the MEA experiments and data analysis. M.S.H. performed western blotting, and H.Y. performed the biophysical validation of *hSCN2A*-HA. W.C.S. generated and provided the *SCN2A* gene-edited hiPSC lines. I.M.G.D.-R. and T.D.B. generated and provided the CAV-2 vectors under E.J.K.'s supervision. H.K. performed and N.A.L. supervised the bulk RNA-seq analysis. H.D.G. and J.L. provided the Xenium slides and analyzed the Xenium data. J.W., Y.-E.Y., Z.Z., M.W., E.N.C., Y.Z., M.I.O.-A., K.W.W., and Z.Q. contributed to experiments and data analysis. X.C. and J.Z. analyzed and interpreted the

data and prepared the figures. C.Y., A.J.S., and J.-C.R. provided intellectual input and revised the manuscript. Y.Y. acquired funding, supervised the project, and interpreted the data. X.C., J.Z., and Y.Y. wrote the manuscript, which all authors reviewed and approved.

DECLARATION OF INTERESTS

A provisional patent application entitled "A Vector, Composition, and Method to Provide Exogenous $Na_V1.2$ Activity via CAV-2-Mediated Delivery of an *SCN2A* Expression Cassette" has been filed.

DECLARATION OF GENERATIVE AI AND AI-ASSISTED TECHNOLOGIES IN THE WRITING PROCESS

During the preparation of this work, the authors used ChatGPT to improve the readability and language in this manuscript while ensuring that the main conclusions remained unchanged. After using this tool, the authors reviewed and edited the wording as necessary and take full responsibility for the content of the publication.

STAR★METHODS

Detailed methods are provided in the online version of this paper and include the following:

- KEY RESOURCES TABLE
- EXPERIMENTAL MODEL AND STUDY PARTICIPANT DETAILS
  - The hiPSC lines
- METHOD DETAILS
  - Antibodies
  - Genotyping
  - Generation of hStrOs and hCOs from hiPSCs
  - Viral labeling and live-cell imaging of cortico-striatal assembloids
  - Patch-clamp recordings
  - High-density microelectrode array (HD-MEA) recording of cortico-striatal assembloids
  - Cryoprotection, immunocytochemistry, and imaging analysis
  - Western blotting
  - RNA isolation, reverse transcription, and qPCR analysis
  - Xenium spatial transcriptomic profiling and analysis
  - Bulk RNA sequencing and analysis
- QUANTIFICATION AND STATISTICAL ANALYSIS

SUPPLEMENTAL INFORMATION

Supplemental information can be found online at https://doi.org/10.1016/j.neuron.2026.08.031.

Received: May 22, 2025
Revised: May 6, 2026
Accepted: August 31, 2026

REFERENCES

1. Shaw, K.A., Williams, S., Patrick, M.E., Valencia-Prado, M., Durkin, M.S., Howerton, E.M., Ladd-Acosta, C.M., Pas, E.T., Bakian, A.V., Bartholomew, P., et al. (2025). Prevalence and early identification of autism spectrum disorder among children aged 4 and 8 years–Autism and Developmental Disabilities Monitoring Network, 16 sites, United States, 2022. MMWR Surveill. Summ. *74*, 1–22. https://doi.org/10.15585/mmwr.ss7402a1.
2. Klei, L., Sanders, S.J., Murtha, M.T., Hus, V., Lowe, J.K., Willsey, A.J., Moreno-De-Luca, D., Yu, T.W., Fombonne, E., Geschwind, D., et al. (2012). Common genetic variants, acting additively, are a major source of risk for autism. Mol. Autism *3*, 9. https://doi.org/10.1186/2040-2392-3-9.
3. O'Roak, B.J., Deriziotis, P., Lee, C., Vives, L., Schwartz, J.J., Girirajan, S., Karakoc, E., MacKenzie, A.P., Ng, S.B., Baker, C., et al. (2011). Exome sequencing in sporadic autism spectrum disorders identifies severe *de novo* mutations. Nat. Genet. *43*, 585–589. https://doi.org/10.1038/ng.835.
4. Sanders, S.J., Murtha, M.T., Gupta, A.R., Murdoch, J.D., Raubeson, M.J., Willsey, A.J., Ercan-Sencicek, A.G., DiLullo, N.M., Parikshak, N.N., Stein, J.L., et al. (2012). *De novo* mutations revealed by whole-exome sequencing are strongly associated with autism. Nature *485*, 237–241. https://doi.org/10.1038/nature10945.
5. Satterstrom, F.K., Kosmicki, J.A., Wang, J., Breen, M.S., De Rubeis, S., An, J.Y., Peng, M., Collins, R., Grove, J., Klei, L., et al. (2020). Large-Scale Exome Sequencing Study Implicates Both Developmental and Functional Changes in the Neurobiology of Autism. Cell *180*, 568–584.e23. https://doi.org/10.1016/j.cell.2019.12.036.
6. Uddin, M., Tammimies, K., Pellecchia, G., Alipanahi, B., Hu, P., Wang, Z., Pinto, D., Lau, L., Nalpathamkalam, T., Marshall, C.R., et al. (2014). Brain-expressed exons under purifying selection are enriched for *de novo* mutations in autism spectrum disorder. Nat. Genet. *46*, 742–747. https://doi.org/10.1038/ng.2980.
7. Ben-Shalom, R., Keeshen, C.M., Berrios, K.N., An, J.Y., Sanders, S.J., and Bender, K.J. (2017). Opposing Effects on $Na_V1.2$ Function Underlie Differences Between SCN2A Variants Observed in Individuals With Autism Spectrum Disorder or Infantile Seizures. Biol. Psychiatry *82*, 224–232. https://doi.org/10.1016/j.biopsych.2017.01.009.
8. Spratt, P.W.E., Ben-Shalom, R., Keeshen, C.M., Burke, K.J., Jr., Clarkson, R.L., Sanders, S.J., and Bender, K.J. (2019). The Autism-Associated Gene *Scn2a* Contributes to Dendritic Excitability and Synaptic Function in the Prefrontal Cortex. Neuron *103*, 673–685.e5. https://doi.org/10.1016/j.neuron.2019.05.037.
9. Nelson, A.D., Catalfio, A.M., Gupta, J.P., Min, L., Caballero-Florán, R.N., Dean, K.P., Elvira, C.C., Derderian, K.D., Kyoung, H., Sahagun, A., et al. (2024). Physical and functional convergence of the autism risk genes *Scn2a* and *Ank2* in neocortical pyramidal cell dendrites. Neuron *112*, 1133–1149.e6. https://doi.org/10.1016/j.neuron.2024.01.003.
10. Murugan, M., Jang, H.J., Park, M., Miller, E.M., Cox, J., Taliaferro, J.P., Parker, N.F., Bhave, V., Hur, H., Liang, Y., et al. (2017). Combined Social and Spatial Coding in a Descending Projection from the Prefrontal Cortex. Cell *171*, 1663–1677.e16. https://doi.org/10.1016/j.cell.2017.11.002.
11. Ma, Z.-H., Lu, B., Li, X., Mei, T., Guo, Y.-Q., Yang, L., Wang, H., Tang, X.-Z., Ji, Z.-Z., Liu, J.-R., et al. (2022). Atypicalities in the developmental trajectory of cortico-striatal functional connectivity in autism spectrum disorder. Autism *26*, 1108–1122. https://doi.org/10.1177/13623613211041904.
12. Jourdon, A., Wu, F., Mariani, J., Capauto, D., Norton, S., Tomasini, L., Amiri, A., Suvakov, M., Schreiner, J.D., Jang, Y., et al. (2023). Modeling idiopathic autism in forebrain organoids reveals an imbalance of excitatory cortical neuron subtypes during early neurogenesis. Nat. Neurosci. *26*, 1505–1515. https://doi.org/10.1038/s41593-023-01399-0.
13. Huang, W.K., Wong, S.Z.H., Pather, S.R., Nguyen, P.T.T., Zhang, F., Zhang, D.Y., Zhang, Z., Lu, L., Fang, W., Chen, L., et al. (2021). Generation of hypothalamic arcuate organoids from human induced pluripotent stem cells. Cell Stem Cell *28*, 1657–1670.e10. https://doi.org/10.1016/j.stem.2021.04.006.
14. Miura, Y., Li, M.Y., Birey, F., Ikeda, K., Revah, O., Thete, M.V., Park, J.Y., Puno, A., Lee, S.H., Porteus, M.H., and Pasca, S.P. (2020). Generation of human striatal organoids and cortico-striatal assembloids from human pluripotent stem cells. Nat. Biotechnol. *38*, 1421–1430. https://doi.org/10.1038/s41587-020-00763-w.
15. Andersen, J., Revah, O., Miura, Y., Thom, N., Amin, N.D., Kelley, K.W., Singh, M., Chen, X., Thete, M.V., Walczak, E.M., et al. (2020). Generation of Functional Human 3D Cortico-Motor Assembloids. Cell *183*, 1913–1929.e26. https://doi.org/10.1016/j.cell.2020.11.017.

Please cite this article in press as: Chen et al., Autism-associated *SCN2A* deficiency disrupts cortico-striatal circuitry in human brain assembloids, Neuron (2026), https://doi.org/10.1016/j.neuron.2026.08.031

16. Miura, Y., Li, M.-Y., Revah, O., Yoon, S.-J., Narazaki, G., and Pașca, S.P. (2022). Engineering brain assembloids to interrogate human neural circuits. Nat. Protoc. *17*, 15–35. https://doi.org/10.1038/s41596-021-00632-z.

17. Birey, F., Li, M.Y., Gordon, A., Thete, M.V., Valencia, A.M., Revah, O., Pașca, A.M., Geschwind, D.H., and Pașca, S.P. (2022). Dissecting the molecular basis of human interneuron migration in forebrain assembloids from Timothy syndrome. Cell Stem Cell *29*, 248–264.e7. https://doi.org/10.1016/j.stem.2021.11.011.

18. Kim, J.I., Miura, Y., Li, M.Y., Revah, O., Selvaraj, S., Birey, F., Meng, X., Thete, M.V., Pavlov, S.D., Andersen, J., et al. (2024). Human assembloids reveal the consequences of *CACNA1G* gene variants in the thalamocortical pathway. Neuron *112*, 4048–4059.e7. https://doi.org/10.1016/j.neuron.2024.09.020.

19. Onesto, M.M., Kim, J.I., and Pasca, S.P. (2024). Assembloid models of cell-cell interaction to study tissue and disease biology. Cell Stem Cell *31*, 1563–1573. https://doi.org/10.1016/j.stem.2024.09.017.

20. Del Rio, D., Beucher, B., Lavigne, M., Wehbi, A., Gonzalez Dopeso-Reyes, I., Saggio, I., and Kremer, E.J. (2019). CAV-2 Vector Development and Gene Transfer in the Central and Peripheral Nervous Systems. Front. Mol. Neurosci. *12*, 71. https://doi.org/10.3389/fnmol.2019.00071.

21. Yger, M., and Girault, J.A. (2011). DARPP-32, Jack of All Trades… Master of Which? Front. Behav. Neurosci. *5*, 56. https://doi.org/10.3389/fnbeh.2011.00056.

22. Onn, S.P., Lin, M., Liu, J.J., and Grace, A.A. (2008). Dopamine and cyclic-AMP regulated phosphoprotein-32-dependent modulation of prefrontal cortical input and intercellular coupling in mouse accumbens spiny and aspiny neurons. Neuroscience *151*, 802–816. https://doi.org/10.1016/j.neuroscience.2007.11.019.

23. H. Steiner, and K.Y. Tseng, eds. (2016). Handbook of Basal Ganglia Structure and Function, Second Edition (Academic Press).

24. Zhang, J., Chen, X., Eaton, M., Wu, J., Ma, Z., Lai, S., Park, A., Ahmad, T.S., Que, Z., Lee, J.H., et al. (2021). Severe deficiency of the voltage-gated sodium channel $Na_V1.2$ elevates neuronal excitability in adult mice. Cell Rep. *36*, 109495. https://doi.org/10.1016/j.celrep.2021.109495.

25. Kole, M.H.P., and Stuart, G.J. (2012). Signal processing in the axon initial segment. Neuron *73*, 235–247. https://doi.org/10.1016/j.neuron.2012.01.007.

26. Yamada, R., and Kuba, H. (2016). Structural and functional plasticity at the axon initial segment. Front. Cell. Neurosci. *10*, 250. https://doi.org/10.3389/fncel.2016.00250.

27. Harley, P., Kerins, C., Gatt, A., Neves, G., Riccio, F., Machado, C.B., Cheesbrough, A., R'Bibo, L., Burrone, J., and Lieberam, I. (2023). Aberrant axon initial segment plasticity and intrinsic excitability of ALS hiPSC motor neurons. Cell Rep. *42*, 113509. https://doi.org/10.1016/j.celrep.2023.113509.

28. Berg, A.T., Thompson, C.H., Myers, L.S., Anderson, E., Evans, L., Kaiser, A.J.E., Paltell, K., Nili, A.N., DeKeyser, J.-M.L., Abramova, T.V., et al. (2024). Expanded clinical phenotype spectrum correlates with variant function in *SCN2A*-related disorders. Brain *147*, 2761–2774. https://doi.org/10.1093/brain/awae125.

29. Fadila, S., Beucher, B., Dopeso-Reyes, I.G., Mavashov, A., Brusel, M., Anderson, K., Ismeurt, C., Goldberg, E.M., Ricobaraza, A., Hernandez-Alcoceba, R., et al. (2023). Viral vector-mediated expression of $Na_V1.1$, after seizure onset, reduces epilepsy in mice with Dravet syndrome. J. Clin. Investig. *133*, e159316. https://doi.org/10.1172/JCI159316.

30. Smith, K.R., Kopeikina, K.J., Fawcett-Patel, J.M., Leaderbrand, K., Gao, R., Schürmann, B., Myczek, K., Radulovic, J., Swanson, G.T., and Penzes, P. (2014). Psychiatric risk factor ANK3/ankyrin-G nanodomains regulate the structure and function of glutamatergic synapses. Neuron *84*, 399–415. https://doi.org/10.1016/j.neuron.2014.10.010.

31. Zhang, J., Eaton, M., Chen, X., Zhao, Y., Kant, S., Deming, B.A., Harish, K., Nguyen, H.P., Shu, Y., Lai, S., et al. (2025). Restoration of excitation/inhibition balance enhances neuronal signal-to-noise ratio and rescues social deficits in autism-associated *Scn2a*-deficiency. Preprint at bioRxiv. https://doi.org/10.1101/2025.03.04.641498.

32. Spratt, P.W.E., Alexander, R.P.D., Ben-Shalom, R., Sahagun, A., Kyoung, H., Keeshen, C.M., Sanders, S.J., and Bender, K.J. (2021). Paradoxical hyperexcitability from $Na_V1.2$ sodium channel loss in neocortical pyramidal cells. Cell Rep. *36*, 109483. https://doi.org/10.1016/j.celrep.2021.109483.

33. Quadrato, G., Nguyen, T., Macosko, E.Z., Sherwood, J.L., Min Yang, S., Berger, D.R., Maria, N., Scholvin, J., Goldman, M., Kinney, J.P., et al. (2017). Cell diversity and network dynamics in photosensitive human brain organoids. Nature *545*, 48–53. https://doi.org/10.1038/nature22047.

34. Fair, S.R., Julian, D., Hartlaub, A.M., Pusuluri, S.T., Malik, G., Summerfied, T.L., Zhao, G., Hester, A.B., Ackerman, W.E., Hollingsworth, E.W., et al. (2020). Electrophysiological Maturation of Cerebral Organoids Correlates with Dynamic Morphological and Cellular Development. Stem Cell Rep. *15*, 855–868. https://doi.org/10.1016/j.stemcr.2020.08.017.

35. Pașca, A.M., Sloan, S.A., Clarke, L.E., Tian, Y., Makinson, C.D., Huber, N., Kim, C.H., Park, J.-Y., O'Rourke, N.A., Nguyen, K.D., et al. (2015). Functional cortical neurons and astrocytes from human pluripotent stem cells in 3D culture. Nat. Methods *12*, 671–678. https://doi.org/10.1038/nmeth.3415.

36. Tamura, S., Nelson, A.D., Spratt, P.W.E., Hamada, E.C., Zhou, X., Kyoung, H., Li, Z., Arnould, C., Barskyi, V., Krupkin, B., et al. (2025). CRISPR activation for *SCN2A*-related neurodevelopmental disorders. Nature *646*, 983–991. https://doi.org/10.1038/s41586-025-09522-w.

37. Nunes, C., Gorczyca, G., Mendoza-deGyves, E., Ponti, J., Bogni, A., Carpi, D., Bal-Price, A., and Pistollato, F. (2022). Upscaling biological complexity to boost neuronal and oligodendroglia maturation and improve *in vitro* developmental neurotoxicity (DNT) evaluation. Reprod. Toxicol. *110*, 124–140. https://doi.org/10.1016/j.reprotox.2022.03.017.

38. Sanders, S.J., Campbell, A.J., Cottrell, J.R., Moller, R.S., Wagner, F.F., Auldridge, A.L., Bernier, R.A., Catterall, W.A., Chung, W.K., Empfield, J.R., et al. (2018). Progress in Understanding and Treating *SCN2A*-Mediated Disorders. Trends Neurosci. *41*, 442–456. https://doi.org/10.1016/j.tins.2018.03.011.

39. Epifanio, R., Giorda, R., Merlano, M.C., Zanotta, N., Romaniello, R., Marelli, S., Russo, S., Cogliati, F., Bassi, M.T., and Zucca, C. (2021). *SCN2A* Pathogenic Variants and Epilepsy: Heterogeneous Clinical, Genetic and Diagnostic Features. Brain Sci. *12*, 18. https://doi.org/10.3390/brainsci12010018.

40. Carvill, G.L., Matheny, T., Hesselberth, J., and Demarest, S. (2021). Haploinsufficiency, Dominant Negative, and Gain-of-Function Mechanisms in Epilepsy: Matching Therapeutic Approach to the Pathophysiology. Neurotherapeutics *18*, 1500–1514. https://doi.org/10.1007/s13311-021-01137-z.

41. Gao, Y., Shonai, D., Trn, M., Zhao, J., Soderblom, E.J., Garcia-Moreno, S.A., Gersbach, C.A., Wetsel, W.C., Dawson, G., Velmeshev, D., et al. (2024). Proximity analysis of native proteomes reveals phenotypic modifiers in a mouse model of autism and related neurodevelopmental conditions. Nat. Commun. *15*, 6801. https://doi.org/10.1038/s41467-024-51037-x.

42. Hirsch, M.L., Agbandje-McKenna, M., and Samulski, R.J. (2010). Little vector, big gene transduction: fragmented genome reassembly of adeno-associated virus. Mol. Ther. *18*, 6–8. https://doi.org/10.1038/mt.2009.280.

43. Yang, Y. (2025). What we can learn from the first personalized CRISPR-treated baby to tackle genetic brain disorders. Neuron *113*, 3697–3702. https://doi.org/10.1016/j.neuron.2025.10.023.

44. Marshel, J.H., Kim, Y.S., Machado, T.A., Quirin, S., Benson, B., Kadmon, J., Raja, C., Chibukhchyan, A., Ramakrishnan, C., Inoue, M., et al. (2019). Cortical layer–specific critical dynamics triggering perception. Science *365*, eaaw5202. https://doi.org/10.1126/science.aaw5202.

45. Pantazis, C.B., Yang, A., Lara, E., McDonough, J.A., Blauwendraat, C., Peng, L., Oguro, H., Kanaujiya, J., Zou, J., Sebesta, D., et al. (2022). A reference human induced pluripotent stem cell line for large-scale

Please cite this article in press as: Chen et al., Autism-associated *SCN2A* deficiency disrupts cortico-striatal circuitry in human brain assembloids, Neuron (2026), https://doi.org/10.1016/j.neuron.2026.08.031

collaborative studies. Cell Stem Cell *29*, 1685–1702.e22. https://doi.org/10.1016/j.stem.2022.11.004.

46. Que, Z., Olivero-Acosta, M.I., Zhang, J., Eaton, M., Tukker, A.M., Chen, X., Wu, J., Xie, J., Xiao, T., Wettschurack, K., et al. (2021). Hyperexcitability and pharmacological responsiveness of cortical neurons derived from human iPSCs carrying epilepsy-associated sodium channel $Na_V1.2$-L1342P genetic variant. J. Neurosci. *41*, 10194–10208. https://doi.org/10.1523/JNEUROSCI.0564-21.2021.
47. Wolf, F.A., Angerer, P., and Theis, F.J. (2018). SCANPY: large-scale single-cell gene expression data analysis. Genome Biol. *19*, 15. https://doi.org/10.1186/s13059-017-1382-0.
48. Traag, V.A., Waltman, L., and van Eck, N.J. (2019). From Louvain to Leiden: guaranteeing well-connected communities. Sci. Rep. *9*, 5233. https://doi.org/10.1038/s41598-019-41695-z.
49. Chen, S., Zhou, Y., Chen, Y., and Gu, J. (2018). fastp: an ultra-fast all-in-one FASTQ preprocessor. Bioinformatics *34*, i884–i890. https://doi.org/10.1093/bioinformatics/bty560.
50. Dobin, A., Davis, C.A., Schlesinger, F., Drenkow, J., Zaleski, C., Jha, S., Batut, P., Chaisson, M., and Gingeras, T.R. (2013). STAR: ultrafast universal RNA-seq aligner. Bioinformatics *29*, 15–21. https://doi.org/10.1093/bioinformatics/bts635.
51. McKenna, A., Hanna, M., Banks, E., Sivachenko, A., Cibulskis, K., Kernytsky, A., Garimella, K., Altshuler, D., Gabriel, S., Daly, M., and DePristo, M.A. (2010). The Genome Analysis Toolkit: a MapReduce framework for analyzing next-generation DNA sequencing data. Genome Res. *20*, 1297–1303. https://doi.org/10.1101/gr.107524.110.
52. Brouard, J.S., Schenkel, F., Marete, A., and Bissonnette, N. (2019). The GATK joint genotyping workflow is appropriate for calling variants in RNA-seq experiments. J. Anim. Sci. Biotechnol. *10*, 44. https://doi.org/10.1186/s40104-019-0359-0.
53. Liao, Y., Smyth, G.K., and Shi, W. (2014). featureCounts: an efficient general purpose program for assigning sequence reads to genomic features. Bioinformatics *30*, 923–930. https://doi.org/10.1093/bioinformatics/btt656.
54. Love, M.I., Huber, W., and Anders, S. (2014). Moderated estimation of fold change and dispersion for RNA-seq data with DESeq2. Genome Biol. *15*, 550. https://doi.org/10.1186/s13059-014-0550-8.
55. Ihaka, R., and Gentleman, R. (1996). R: a language for data analysis and graphics. J. Comput. Graph. Stat. *5*, 299–314. https://doi.org/10.1080/10618600.1996.10474713.
56. Risso, D., Ngai, J., Speed, T.P., and Dudoit, S. (2014). Normalization of RNA-seq data using factor analysis of control genes or samples. Nat. Biotechnol. *32*, 896–902. https://doi.org/10.1038/nbt.2931.
57. Robinson, M.D., McCarthy, D.J., and Smyth, G.K. (2010). edgeR: a Bioconductor package for differential expression analysis of digital gene expression data. Bioinformatics *26*, 139–140. https://doi.org/10.1093/bioinformatics/btp616.
58. Yu, G., Wang, L.G., Han, Y., and He, Q.Y. (2012). clusterProfiler: an R package for comparing biological themes among gene clusters. Omics *16*, 284–287. https://doi.org/10.1089/omi.2011.0118.
59. Krämer, A., Green, J., Pollard, J., Jr., and Tugendreich, S. (2014). Causal analysis approaches in Ingenuity Pathway Analysis. Bioinformatics *30*, 523–530. https://doi.org/10.1093/bioinformatics/btt703.
60. Gu, Z. (2022). Complex heatmap visualization. iMeta *1*, e43. https://doi.org/10.1002/imt2.43.
61. Blighe, K., Rana, S., and Lewis, M. (2022). EnhancedVolcano: Publication-Ready Volcano Plots with Enhanced Colouring and Labeling. R Package Version 1.16.0. https://doi.org/10.18129/B9.bioc.EnhancedVolcano.
62. Korsunsky, I., Millard, N., Fan, J., Slowikowski, K., Zhang, F., Wei, K., Baglaenko, Y., Brenner, M., Loh, P.-R., and Raychaudhuri, S. (2019). Fast, sensitive and accurate integration of single-cell data with Harmony. Nat. Methods *16*, 1289–1296. https://doi.org/10.1038/s41592-019-0619-0.
63. Skarnes, W.C., Pellegrino, E., and McDonough, J.A. (2019). Improving homology-directed repair efficiency in human stem cells. Methods *164–165*, 18–28. https://doi.org/10.1016/j.ymeth.2019.06.016.
64. Skarnes, W.C., Ning, G., Giansiracusa, S., Cruz, A.S., Blauwendraat, C., Saavedra, B., Holden, K., Cookson, M.R., Ward, M.E., and McDonough, J.A. (2021). Controlling homology-directed repair outcomes in human stem cells with dCas9. Preprint at bioRxiv. https://doi.org/10.1101/2021.12.16.472942.
65. Paşca, S.P., Arlotta, P., Bateup, H.S., Camp, J.G., Cappello, S., Gage, F.H., Knoblich, J.A., Kriegstein, A.R., Lancaster, M.A., Ming, G.L., et al. (2025). A framework for neural organoids, assembloids and transplantation studies. Nature *639*, 315–320. https://doi.org/10.1038/s41586-024-08487-6.
66. Zhang, J., Zhang, C., Chen, X., Wang, B., Ma, W., Yang, Y., Zheng, R., and Huang, Z. (2021). PKA-RIIβ autophosphorylation modulates PKA activity and seizure phenotypes in mice. Commun. Biol. *4*, 263. https://doi.org/10.1038/s42003-021-01748-4.
67. Wang, J., He, X., Meng, H., Li, Y., Dmitriev, P., Tian, F., Page, J.C., Lu, Q.R., and He, Z. (2020). Robust myelination of regenerated axons induced by combined manipulations of GPR17 and microglia. Neuron *108*, 876–886.e4. https://doi.org/10.1016/j.neuron.2020.09.016.

Please cite this article in press as: Chen et al., Autism-associated *SCN2A* deficiency disrupts cortico-striatal circuitry in human brain assembloids, Neuron (2026), https://doi.org/10.1016/j.neuron.2026.08.031

STAR★METHODS

KEY RESOURCES TABLE

REAGENT or RESOURCE	SOURCE	IDENTIFIER
Antibodies		
Chicken anti-NeuN antibody	GeneTex	Cat# GTX00837; RRID:AB_2937041
Rabbit anti-NeuN antibody	Cell Signaling Technology	Cat# 24307S; equivalent base Cat#24307; Clone D4G4O; RRID:AB_2651140
Rabbit anti-TBR1 antibody	Abcam	Cat# ab31940; RRID:AB_2200219
Chicken anti-MAP2 antibody	Novus Biologicals	Cat# NB300-213; RRID:AB_2138178
Mouse anti-MAP2 antibody	Millipore	Cat# MAB378; RRID:AB_94967
Rabbit anti-GABA antibody	Sigma-Aldrich	Cat# A2052; RRID:AB_477652
Mouse anti-GAD67 antibody	Sigma-Aldrich/MilliporeSigma	Cat# MAB5406-25UG; equivalent base Cat#MAB5406; Clone 1G10.2; RRID:AB_2278725
Rat anti-CTIP2 antibody	Abcam	Cat# ab18465; Clone 25B6; RRID:AB_2064130
Rabbit anti-DARPP32 antibody	Abcam	Cat# ab40801; Clone EP720Y; RRID:AB_731843
Mouse anti-Ankyrin-G antibody	Antibodies Inc./NeuroMab	Cat# 75-146-020; equivalent base Cat#75-146; Clone N106/36; RRID:AB_10673030
Rabbit anti-*SCN2A*/$Na_V1.2$ antibody	Sigma-Aldrich/MilliporeSigma	Cat# ZRB1300; Clone 3F19; RRID:AB_3751956
Rabbit anti-HA-tag antibody	Cell Signaling Technology	Cat# 3724T; Clone C29F4; RRID:AB_1549585
Mouse anti-Synapsin 1 antibody	Synaptic Systems	Cat# 106011; RRID:AB_2619772
Rabbit anti-PSD-95 antibody	Thermo Fisher Scientific/Invitrogen	Cat# 51-6900; RRID:AB_2533914
Mouse anti-SATB2 antibody	Abcam	Cat# ab51502; Clone SATBA4B10; RRID:AB_882455
Mouse anti-VGAT antibody	Synaptic Systems	Cat# 131011; RRID:AB_887872
Rabbit anti-cleaved caspase-3 (Asp175) antibody	Cell Signaling Technology	Cat# 9661; RRID:AB_2341188
Rabbit anti-*SCN2A*/$Na_V1.2$ antibody	Alomone Labs	Cat# ASC-002; RRID:AB_2040005
Mouse anti-TUJ1 antibody	BioLegend	Cat# 801202; Clone TUJ1; RRID:AB_2313773
Mouse anti-beta-Actin antibody	Thermo Fisher Scientific/Invitrogen	Cat# MA5-15739; Clone BA3R; RRID:AB_10979409
Goat anti-Chicken Alexa Fluor 647 secondary antibody	Thermo Fisher Scientific/Invitrogen	Cat# A32933; RRID:AB_2762845
Goat anti-Rabbit Alexa Fluor 647 secondary antibody	Thermo Fisher Scientific/Invitrogen	Cat# A21244; RRID:AB_2535812
Goat anti-Mouse Alexa Fluor 647 secondary antibody	Thermo Fisher Scientific/Invitrogen	Cat# A21235; RRID:AB_2535804
Goat anti-Rat Alexa Fluor 555 secondary antibody	Thermo Fisher Scientific/Invitrogen	Cat# A21434; RRID:AB_2535855
Goat anti-Rabbit Alexa Fluor 488 secondary antibody	Thermo Fisher Scientific/Invitrogen	Cat# A11034; RRID:AB_2576217
Goat anti-Rabbit Alexa Fluor Plus 555 secondary antibody	Thermo Fisher Scientific/Invitrogen	Cat# A32732; RRID:AB_2633281
Goat anti-Mouse Alexa Fluor Plus 555 secondary antibody	Thermo Fisher Scientific/Invitrogen	Cat# A32727; RRID:AB_2633276
Goat anti-Mouse Alexa Fluor 488 secondary antibody	Thermo Fisher Scientific/Invitrogen	Cat# A11001; RRID:AB_2534069
IRDye 800CW Goat anti-Rabbit IgG	LI-COR Biosciences/LICORbio	Cat# 926-32211; RRID:AB_621843

(*Continued on next page*)

Please cite this article in press as: Chen et al., Autism-associated *SCN2A* deficiency disrupts cortico-striatal circuitry in human brain assembloids, Neuron (2026), https://doi.org/10.1016/j.neuron.2026.08.031

Continued

REAGENT or RESOURCE	SOURCE	IDENTIFIER
IRDye 800CW Goat anti-Mouse IgG	LI-COR Biosciences/LICORbio	Cat# 926-32210; RRID:AB_621842
Bacterial and virus strains		
pENN.AAV.hSyn.Cre.WPRE.hGH, AAV1 viral prep (AAV1-hSyn::Cre)	James M. Wilson, unpublished	Addgene viral prep #105553-AAV1; RRID:Addgene_105553
pENN.AAV.hSyn.Cre.WPRE.hGH, AAVrg viral prep (AAVrg-hSyn::Cre)	James M. Wilson; unpublished	Addgene viral prep #105553-AAVrg; RRID:Addgene_105553
pAAV-Ef1a-DIO-mScarlet	Marshel et al.[44]	Addgene viral prep #131002-AAV1; RRID:Addgene_131002
pAAV-hSyn-mScarlet	Marshel et al.[44]	Addgene viral prep #131001-AAV1; RRID:Addgene_131001
pAAV-hSyn-EGFP	Bryan Roth; unpublished	Addgene viral prep #50465-AAV9; RRID:Addgene_50465
pAAV-hSyn-hM3D(Gq)-mCherry	Bryan Roth; unpublished	Addgene viral prep #50474-AAV9; RRID:Addgene_50474
CAV-2-NSE-*SCN2A*-HA (CAV-*SCN2A*)	This paper; Kremer laboratory/IGMM Montpellier	N/A
CAV-2-NSE-mCitrine (CAV-Ctrl)	This paper; Kremer laboratory/IGMM Montpellier	N/A
Biological samples		
Human cortical organoids (hCOs)	This paper	N/A
Human striatal organoids (hStrOs)	This paper	N/A
Human cortico-striatal assembloids (hCO-hStrO)	This paper	N/A
Dissociated hCO-derived neurons	This paper	N/A
Chemicals, peptides, and recombinant proteins		
Matrigel basement membrane matrix	Corning	Cat# 354230
StemFlex medium	Thermo Fisher Scientific	Cat# A3349401
Versene solution	Thermo Fisher Scientific	Cat# 15040066
Accutase	Thermo Fisher Scientific / Fisher Scientific	Cat#NC9839010; equivalent Thermo Fisher Cat#00-4555-56
Essential 8 medium	Thermo Fisher Scientific	Cat# A1517001
ROCK inhibitor Y-27632	Selleck Chemicals	Cat# S1049
Essential 6 medium	Thermo Fisher Scientific	Cat# A1516401
Dorsomorphin	Sigma-Aldrich	Cat# P5499
SB-431542	R&D Systems	Cat# 1614
XAV-939	Tocris	Cat# 3748
Neurobasal-A medium	Thermo Fisher Scientific	Cat# 10888022
B-27 supplement without vitamin A	Thermo Fisher Scientific	Cat# 12587010
GlutaMAX Supplement	Thermo Fisher Scientific	Cat# 35050061
Penicillin–streptomycin	Thermo Fisher Scientific	Cat# 15140122
Recombinant human FGF basic/FGF2	R&D Systems	Cat# 233-FB-500
Recombinant human EGF protein	R&D Systems	Cat# 236-EG
WNT inhibitor IWP-2	Selleck Chemicals	Cat# S7085
Recombinant Activin A	PeproTech	Cat# 120-14P
SR11237	Tocris	Cat# 3411
BDNF	PeproTech	Cat# 450-02
NT-3	PeproTech	Cat# 450-03
Ascorbic acid	Wako	Cat# 323-44822
Dibutyryl-cAMP	Santa Cruz Biotechnology	Cat# sc-201567A
DHA	MilliporeSigma	Cat# D2534

(*Continued on next page*)

Please cite this article in press as: Chen et al., Autism-associated *SCN2A* deficiency disrupts cortico-striatal circuitry in human brain assembloids, Neuron (2026), https://doi.org/10.1016/j.neuron.2026.08.031

Continued

REAGENT or RESOURCE	SOURCE	IDENTIFIER
DAPT	STEMCELL Technologies	Cat# 72082
B-27 Plus Supplement	Thermo Fisher Scientific	Cat# A3582801
BrainPhys medium	STEMCELL Technologies	Cat# 5790
Laminin from human fibroblasts	Sigma-Aldrich	Cat# L4544
Clozapine N-oxide dihydrochloride	Tocris Bioscience	Cat# 6329
Agarose	Sigma-Aldrich	Cat# A9539
Neurobiotin	Vector Laboratories	Cat# SP-1120
Alexa Fluor 647-conjugated streptavidin	Thermo Fisher Scientific	Cat# S32357
DMEM/F-12	Thermo Fisher Scientific/Gibco	Cat# 11320082
Fetal Bovine Serum, USDA Certified	MidSci/Harvest	Cat# USDAFBSHI
0.25% trypsin	Corning	Cat# 25-053-CI
Poly-D-lysine-coated coverslips	Corning	Cat# 354086
Poly-L-ornithine	Sigma-Aldrich	Cat# P4957
Tergazyme	Alconox	Cat# 1304-1
Optimal cutting temperature (OCT) compound	Sakura Finetek	Cat# 4583
VECTASHIELD Antifade Mounting Medium with DAPI	Vector Laboratories	Cat# H-2000
Block-Ace	Dainippon Sumitomo Pharma	Cat# UK-B80
RIPA buffer	Thermo Fisher Scientific	Cat# 89901
Protease and phosphatase inhibitors	Thermo Fisher Scientific	Cat# A32953
PVDF membrane	Thermo Fisher Scientific	Cat# PB9220
Intercept T20 (TBS) Antibody Diluent	LI-COR Biosciences	Cat# 927-65001
Critical commercial assays		
NucleoSpin DNA RapidLyse	Macherey-Nagel	Cat# 740100.250
Liquid Proteinase K	Macherey-Nagel	Cat# 740396
Quick Taq HS DyeMix	TOYOBO	Cat# DTM-101
Papain Dissociation System	Worthington Biochemical Corporation	Cat# LK003150
Q5 High-Fidelity DNA Polymerase	New England Biolabs	Cat# M0491
Gibson Assembly Master Mix	New England Biolabs	Cat# E2611S
QIAprep Spin Miniprep Kit	QIAGEN	Cat# 27106
Lipofectamine 3000 Transfection Reagent	Thermo Fisher Scientific	Cat# L3000001
Pierce BCA Protein Assay Kit	Thermo Fisher Scientific	Cat# 23225
RNeasy Mini Kit	QIAGEN	Cat# 74104
Maxima First Strand cDNA Synthesis Kit	Thermo Fisher Scientific	Cat# K1672
THUNDERBIRD SYBR qPCR Mix	TOYOBO	Code QPS-201
Xenium Prime 5K Human Pan Tissue and Pathways Panel	10x Genomics	PN: 1000671
Xenium Slides & Sample Prep Reagents	10x Genomics	PN: 1000460
Xenium Cell Segmentation Staining Reagents	10x Genomics	PN: 1000661
Xenium slide	10x Genomics	PN: 3000941
NEBNext Poly(A) mRNA Magnetic Isolation Module	New England Biolabs	Cat# E7490
xGen RNA Library Preparation Kit	Integrated DNA Technologies (IDT)	Cat# 10009814
Infinium Global Diversity Array with Cytogenetics-8 (GDA Cyto)	Illumina	Cat# 20066509
Deposited data		
Bulk RNA-seq raw and processed data	This paper	GEO: GSE330433
Xenium spatial transcriptomic raw and processed data	This paper	GEO: GSE343854

(*Continued on next page*)

Continued

REAGENT or RESOURCE	SOURCE	IDENTIFIER
Human reference genome GRCh38/hg38 and gene annotation	Ensembl/Genome Reference Consortium	Ensembl release 104
Human reference genome hg19	Genome Reference Consortium/UCSC	hg19; used for cytogenetic microarray analysis
Experimental models: Cell lines		
Human: KOLF2.1J WT parental reference hiPSC line; male	The Jackson Laboratory/Cellular Engineering; Pantazis et al.[45]	RRID:CVCL_B5P3
Human: A11 WT isogenic control hiPSC line (C959X series); male	This paper	N/A
Human: B07 WT isogenic control hiPSC line (C959X series); male	This paper	N/A
Human: C03 WT isogenic control hiPSC line (C959X series); male	This paper	N/A
Human: A02 hiPSC line: *SCN2A* c.2877C>A (p.Cys959Ter), heterozygous; male	This paper	N/A
Human: E04 hiPSC line: *SCN2A* c.2877C>A (p.Cys959Ter), heterozygous; male	This paper	N/A
Human: F01 hiPSC line: *SCN2A* c.2877C>A (p.Cys959Ter), heterozygous; male	This paper	N/A
Human: A03 hiPSC line: *SCN2A* c.2877C>A (p.Cys959Ter), homozygous; male	This paper	N/A
Human: D06 hiPSC line: *SCN2A* c.2877C>A (p.Cys959Ter), homozygous; male	This paper	N/A
Human: F03 hiPSC line: *SCN2A* c.2877C>A (p.Cys959Ter), homozygous; male	This paper	N/A
Human: B5 WT isogenic control hiPSC line (R524X series); male	This paper	N/A
Human: C2 WT isogenic control hiPSC line (R524X series); male	This paper	N/A
Human: D6 WT isogenic control hiPSC line (R524X series); male	This paper	N/A
Human: E6 hiPSC line: *SCN2A* c.1570C>T (p.Arg524Ter), heterozygous; male	This paper	N/A
Human: HEK293-derived tsA201 cells; female	Laboratory stock	RRID:CVCL_2737
Oligonucleotides		
Human *SCN2A*-C959X genotyping primer, forward (5′–3′): TTGAGACAGTTACCTGTACATTTGC	Integrated DNA Technologies (IDT)	N/A
Human *SCN2A*-C959X genotyping primer, reverse (5′–3′): TAATAGACAATAGGAAGTGGCCTTG	Integrated DNA Technologies (IDT)	N/A
Human *SCN2A*-R524X genotyping primer, forward (5′–3′): ACATACTTTGCGCCCTTC	Integrated DNA Technologies (IDT)	N/A
Human *SCN2A*-R524X genotyping primer, reverse (5′–3′): CATTGTGCCATCCAGGTG	Integrated DNA Technologies (IDT)	N/A
Human Internal *SCN2A* qPCR primer, forward (5′–3′): GAGACCATGTGGGACTGTATG	Integrated DNA Technologies (IDT)	N/A
Human Internal *SCN2A* qPCR primer, reverse (5′–3′): AAGGCCAAGAAGAGGTTCAG	Integrated DNA Technologies (IDT)	N/A
Human Codon-optimized *SCN2A* qPCR primer, forward (5′–3′): GTGTTTTGCCTCTCCGTGTT	Integrated DNA Technologies (IDT)	N/A

(*Continued on next page*)

Please cite this article in press as: Chen et al., Autism-associated *SCN2A* deficiency disrupts cortico-striatal circuitry in human brain assembloids, Neuron (2026), https://doi.org/10.1016/j.neuron.2026.08.031

Continued

REAGENT or RESOURCE	SOURCE	IDENTIFIER
Human Codon-optimized *SCN2A* qPCR primer, reverse (5′–3′): ATTTCCGTCCAGGGAGTTGT	Integrated DNA Technologies (IDT)	N/A
Total *SCN2A* qPCR primer, forward (5′–3′): GGATACATCTGTGTGAAGGC	Integrated DNA Technologies (IDT)	N/A
Total *SCN2A* qPCR primer, reverse (5′–3′): CTGTTCCTCATAGGCCAT	Integrated DNA Technologies (IDT)	N/A
Human GAPDH qPCR primers, forward (5′–3′): CGCTCTCTGCTCCTCCTGTT	Integrated DNA Technologies (IDT)	N/A
Human GAPDH qPCR primers, reverse (5′–3′): CCATGGTGTCTGAGCGATGT	Integrated DNA Technologies (IDT)	N/A
Recombinant DNA		
CMV promoter-driven untagged tetrodotoxin-resistant human *SCN2A* plasmid with GFP-2A reporter	Gift from Stephen Waxman (Yale University); Que et al.[46]	N/A
CMV promoter-driven C-terminal HA-tagged human *SCN2A* plasmid (*hSCN2A*-HA); generated from the untagged *hSCN2A* plasmid by PCR/Gibson assembly	This paper	N/A
CAV-NSE-*SCN2A*-HA expression cassette	This paper; Kremer laboratory, IGMM Montpellier	N/A
CAV-NSE-mCitrine expression cassette	This paper; Kremer laboratory, IGMM Montpellier	N/A
Software and algorithms		
GraphPad Prism, version 10.4.1	GraphPad Software	https://www.graphpad.com/scientific-software/prism/; RRID:SCR_002798
ImageJ, version 1.53t	National Institutes of Health	https://imagej.nih.gov/ij/; RRID:SCR_003070
Fiji, version 2.18.0	Fiji development team	https://imagej.net/software/fiji/downloads; RRID:SCR_002285
Neurolucida 360, version 2023.1.1	MBF Bioscience	https://www.mbfbioscience.com/products/neurolucida-360/; RRID:SCR_001775
Neurolucida Explorer, version 2022.2.1	MBF Bioscience	https://www.mbfbioscience.com/products/neurolucida-explorer
pCLAMP Software Suite (including Clampfit), version 11.4	Molecular Devices	https://support.moleculardevices.com/s/article/Axon-pCLAMP-11-Electrophysiology-Data-Acquisition-Analysis-Software-Download-Page; RRID:SCR_011323
Mini Analysis Program, version 6.08	Synaptosoft	http://www.synaptosoft.com/MiniAnalysis/; RRID:SCR_002184
PATCHMASTER, version 2x92	HEKA Elektronik	https://www.heka.com/downloads/downloads_main.html; RRID:SCR_000034
BrainWave 5, version 5.6	3Brain AG	https://www.3brain.com/products/software/brainwave5
CFX Maestro Software, version 4.1.2433.1219	Bio-Rad	https://www.bio-rad.com/en-us/product/cfx-maestro-software-for-cfx-real-time-pcr-instruments?ID=OKZP7E15
Bionano VIA software, version 7.0	Bionano Genomics	https://bionano.com/software-products-support/
Python, version 3.14.3	Python Software Foundation	https://www.python.org/; RRID:SCR_008394
Scanpy, version 1.12	Wolf et al.[47]	https://scanpy.readthedocs.io/; RRID:SCR_018139
igraph, version 1.0.0 (Leiden clustering)	Traag et al.[48]	https://igraph.org/python/
Matplotlib, version 3.10.8	Matplotlib Development Team	https://matplotlib.org/; RRID:SCR_008624

(*Continued on next page*)

Please cite this article in press as: Chen et al., Autism-associated *SCN2A* deficiency disrupts cortico-striatal circuitry in human brain assembloids, Neuron (2026), https://doi.org/10.1016/j.neuron.2026.08.031

Continued

REAGENT or RESOURCE	SOURCE	IDENTIFIER
fastp, version 0.23.2	Chen et al.[49]	https://github.com/OpenGene/fastp; RRID:SCR_016962
STAR, version 2.7.10a	Dobin et al.[50]	https://github.com/alexdobin/STAR; RRID:SCR_004463
GATK HaplotypeCaller, version 4.2.2.0	McKenna et al.[51]; Brouard et al.[52]	https://gatk.broadinstitute.org/hc/en-us/articles/360037225632-HaplotypeCaller; RRID:SCR_001876
featureCounts, version 1.6.1	Liao et al.[53]	https://subread.sourceforge.net/; RRID:SCR_012919
DESeq2, version 1.34.0	Love et al.[54]	https://bioconductor.org/packages/DESeq2/; RRID:SCR_015687
R, versions 4.1.3, 4.2.1, and 4.3.2	R Foundation; Ihaka and Gentleman[55]	https://www.r-project.org/; RRID:SCR_001905
RUVSeq, version 1.28.0	Risso et al.[56]	https://bioconductor.org/packages/RUVSeq/; RRID:SCR_006263
edgeR, version 3.36.0	Robinson et al.[57]	https://bioconductor.org/packages/edgeR/; RRID:SCR_012802
clusterProfiler, version 4.10.0	Yu et al.[58]	https://bioconductor.org/packages/clusterProfiler/; RRID:SCR_016884
Ingenuity Pathway Analysis	QIAGEN; Kramer et al.[59]	https://digitalinsights.qiagen.com/ipa; RRID:SCR_008653
ComplexHeatmap, version 2.14.0	Gu et al.[60]	https://bioconductor.org/packages/ComplexHeatmap/
EnhancedVolcano, version 1.16.0	Blighe et al.[61]	https://bioconductor.org/packages/EnhancedVolcano/
enrichplot, version 1.22.0	Bioconductor	https://bioconductor.org/packages/enrichplot/
Xenium Explorer, version 4.1.1	10x Genomics	https://www.10xgenomics.com/support/software/xenium-explorer
harmonypy, version 0.0.10	Korsunsky et al.[62]	https://github.com/slowkow/harmonypy
ZEN 3.1 (blue edition)	Carl Zeiss Microscopy GmbH	https://www.zeiss.com/microscopy/en/products/software/zeiss-zen.html; RRID:SCR_013672
Custom analysis scripts	This paper	Zenodo: https://doi.org/10.5281/zenodo.22031620
Other		
Zeiss LSM 900 confocal microscope	Carl Zeiss	Model: LSM 900
Leica VT1200 S vibratome	Leica Microsystems	Model: VT1200 S
Olympus BX-51WI microscope	Olympus	Model: BX-51WI
IR-2000 camera	Dage-MTI	Model: IR-2000
P-1000 micropipette puller	Sutter Instruments	Model: P-1000
Thin-wall borosilicate glass pipettes	Sutter Instruments	Cat# BF150-110-10
Axon MultiClamp 700B amplifier	Molecular Devices	Model: MultiClamp 700B
Digidata 1550B plus HumSilencer digitizer	Molecular Devices	Model: Digidata 1550B plus HumSilencer
Digitimer DS3 stimulator	Digitimer	Model: DS3
Stimulus Isolator	World Precision Instruments	Model: ISOSTIM A320
EPC10 amplifier	HEKA Elektronik	Model: EPC10
3Brain HyperCAM Alpha multi-well system	3Brain AG	Model: HyperCAM Alpha
CorePlate 6W 38/60 HD-MEA plates	3Brain AG	Model: CorePlate 6W 38/60; 6-well HD-MEA plate; 60 μm electrode pitch
Leica CM1850 cryostat	Leica Microsystems	Model: CM1850
Odyssey CLx Imaging System	LI-COR Biosciences	Model: Odyssey CLx

(*Continued on next page*)

Please cite this article in press as: Chen et al., Autism-associated *SCN2A* deficiency disrupts cortico-striatal circuitry in human brain assembloids, Neuron (2026), https://doi.org/10.1016/j.neuron.2026.08.031

Continued

REAGENT or RESOURCE	SOURCE	IDENTIFIER
NanoDrop spectrophotometer	Thermo Fisher Scientific	Model: NanoDrop One
T100 Thermal Cycler	Bio-Rad	Model: T100
CFX96 Real-Time PCR Detection System	Bio-Rad	Model: CFX96
C1000 Touch PCR thermal cycler	Bio-Rad	Model: C1000 Touch
Illumina NovaSeq X+ system	Illumina	Model: NovaSeq X+
Xenium in situ platform	10x Genomics	Model: Xenium platform
Ultralow-attachment 96-well plates	Corning	Cat# CLS7007
Ultralow-attachment 6-well plates	Corning	Cat# 3471
Glass-bottom 24-well plates	Cellvis	Cat# P24-0-N
40 micrometer cell strainer	CELLTREAT Scientific Products	Cat# 229481
12-mm round coverslips	Neuvitro	Cat# GG-12-1.5-Pre

EXPERIMENTAL MODEL AND STUDY PARTICIPANT DETAILS

The hiPSC lines

SCN2A c.2877C>A (p.Cys959Ter; C959X) mutant hiPSC lines were generated using CRISPR/Cas9-mediated genome editing[63,64] in early passage (p2) KOLF2.1J reference iPSCs.[45] Candidate edited clones were screened by PCR and validated by Sanger sequencing. Heterozygous clones were identified by overlapping C/A peaks at the edited nucleotide, whereas homozygous clones showed a complete C-to-A substitution, consistent with the introduction of a premature stop codon. Correctly edited clones were expanded and assessed for genome integrity to ensure the quality of hiPSCs.[65] This study used the parental KOLF2.1J reference line and three CRISPR-derived isogenic WT control clones (C03, B07, and A11), along with three *SCN2A*-C959X heterozygous mutant lines (A02, E04, and F01), and three *SCN2A*-C959X homozygous mutant lines (A03, D06, and F03). Genotypes were confirmed by Sanger sequencing and batch genotyping for each batch of hiPSC-derived organoids or assembloids.

In addition to the *SCN2A*-C959X series, an independent *SCN2A c.1570C>T* (p.Arg524Ter; R524X) hiPSC series was included for validation of key phenotypes across an additional *SCN2A* truncating mutation. This series comprised three isogenic WT control lines (B5, C2, and D6) and one *SCN2A*-R524X heterozygous mutant line (E6). Genotypes were confirmed by Sanger sequencing and batch genotyping after differentiation. KOLF2.1J served as the common parental reference line from which edited clones were derived. Isogenic relationships among WT and mutant lines are summarized in Table S1, and experiment-specific line usage is summarized in Table S2.

Feeder-free hiPSC colonies were maintained on Matrigel-coated plates (Corning, #354230) in StemFlex medium (Thermo Fisher Scientific, #A3349401) at 37°C in a humidified incubator with 5% CO_2. Medium was changed daily, and cells were passaged every 4–5 days using Versene solution (Thermo Fisher Scientific, #15040066). HiPSCs were used for organoid differentiation between passages 2 and 15 after thawing.

Cytogenetic microarray quality control

Genome integrity of representative edited hiPSC lines was evaluated by high-density cytogenetic microarray analysis performed by JAX Cellular Engineering (The Jackson Laboratory for Genomic Medicine) using the Illumina Infinium Global Diversity Array with Cytogenetics-8 (GDA Cyto). Data were analyzed against the hg19 reference genome using VIA software v7.0 (Bionano Genomics). Copy-number variation (CNV) calling was performed using SNP FASST2 segmentation with a minimum of 50 probes per segment and a significance threshold of 1.00×10^{-13}. The tested lines included KOLF2.1J WT, A11 WT, A02 HET, F01 HET, D06 HOM, and F03 HOM. All tested lines passed array quality control, and no novel sample-specific CNVs were detected. All identified CNVs corresponded only to known background variants in the KOLF2-C1/KOLF2.1J reference line. Detailed results are provided in Table S3.

METHOD DETAILS

Antibodies

For immunostaining, primary antibodies used include Anti-NeuN (Chicken, GeneTex, GTX00837, 1:1000; Rabbit, Cell Signaling, 24307S, 1:1000), Anti-TBR1 (Rabbit, Abcam, ab31940, 1:300), Anti-MAP2 (Chicken, Novus Biologicals, NB300-213, 1:1000; Mouse, Millipore, MAB378, 1:200), Anti-GABA (Rabbit, Sigma-Aldrich, A2052, 1:1000), Anti-GAD67 (Mouse, Sigma-Aldrich, MAB5406-25UG, 1:100), Anti-CTIP2 (Rat, Abcam, ab18465, 1:300), Anti-DARPP32 (Rabbit, Abcam, ab40801, 1:200), Anti-Ankyrin-G (Mouse, Antibodies Inc., 75-146-020, 1:200), Anti-*SCN2A* (Rabbit, Sigma-Aldrich, ZRB1300, 1:200), HA-Tag (Rabbit, Cell Signaling, 3724T, 1:200), Synapsin 1 (Mouse, Synaptic Systems, 106011, 1:800), PSD-95 (Rabbit, Thermo Fisher, 51-6900, 1:800), Anti-SATB2 (Mouse, Abcam, ab51502, 1:300), Anti-VGAT (Mouse, Synaptic Systems, 131011, 1:1000), Anti-Cleaved Caspase-3 (Asp175) (Rabbit, Cell Signaling, 9661, 1:500). Secondary antibodies included Goat anti-Chicken Alexa Fluor 647 (Thermo Fisher, A32933, 1:500), Goat anti-Rabbit Alexa Fluor 647 (A21244, 1:500), Goat anti-Mouse Alexa Fluor 647 (A21235, 1:500), Goat anti-Rat Alexa Fluor 555

Please cite this article in press as: Chen et al., Autism-associated *SCN2A* deficiency disrupts cortico-striatal circuitry in human brain assembloids, Neuron (2026), https://doi.org/10.1016/j.neuron.2026.08.031

(A21434, 1:500), Goat anti-Rabbit Alexa Fluor 488 (A11034, 1:500), Goat anti-Rabbit Alexa Fluor Plus 555 (A32732, 1:500), Goat anti-Mouse Alexa Fluor Plus 555 (A32727, 1:500), and Goat anti-Mouse Alexa Fluor 488 (A11001, 1:500).

For western blotting, primary antibodies included Rabbit anti-SCN2A ($Na_V1.2$) (Alomone Labs, ASC-002, 1:200), Rabbit anti-*SCN2A* (Sigma-Aldrich, ZRB1300, 1:200), Mouse anti-TUJ1 (BioLegend, 801202, 1:1000), and Mouse anti-β-Actin (Thermo Fisher, MA5-15739, 1:1000). Secondary antibodies used were IRDye 800CW Goat anti-Rabbit IgG (LI-COR, 926-32211, 1:2500) and IRDye 800CW Goat anti-Mouse IgG (926-32210, 1:5000).

Genotyping

Genomic DNA was extracted from hiPSCs, organoids, and assembloids using a tissue DNA extraction kit (Macherey-Nagel, Bethlehem, PA, USA). The *SCN2A c.2877C>A* (C959X) variant was genotyped by locus-specific PCR using the following primers: forward, 5′-TTGAGACAGTTACCTGTACATTTGC-3′; and reverse, 5′-TAATAGACAATAGGAAGTGGCCTTG-3′. PCR reactions were prepared in a total volume of 25 μL using PCR Master Mix, primers, template DNA, and nuclease-free water. Amplification was performed at 95°C for 2 min, followed by 35 cycles of 95°C for 30 s, 55°C for 30 s, and 72°C for 1 min, with a final extension at 72°C for 10 min and a hold at 4°C. The resulting 700-bp amplicon was analyzed by Sanger sequencing. WT lines retained cytosine (C) at the variant site, heterozygous lines displayed overlapping C and A peaks, and homozygous lines showed complete substitution of C with A, introducing a premature stop codon. The *SCN2A c.1570C>T* (R524X) variant was similarly genotyped by locus-specific PCR followed by Sanger sequencing. The following primers were used: forward, 5′-ACATACTTTGCGCCCTTC-3′; and reverse, 5′-CATTGTGCCATCCAGGTG-3′.

Generation of hStrOs and hCOs from hiPSCs

Generation of 3D neural organoids

Feeder-free hiPSCs were maintained on Matrigel in StemFlex medium and passaged every 4–5 days as described above. Quality control assessments included Sanger sequencing, karyotyping, and immunocytochemistry. Undifferentiated hiPSC colonies displayed normal and homogeneous morphology with defined edges and minimal spontaneous differentiation. A differentiation batch was defined as an independent differentiation initiated on a separate date.

Organoids were generated using a modified version of the protocol described by Miura et al.[16] hiPSCs were dissociated into single cells using Accutase (Thermo Fisher, #NC9839010) and seeded at 10,000 cells/well in ultralow-attachment 96-well plates (Corning, #CLS7007) with Essential 8 medium (Thermo Fisher, #A1517001) supplemented with 10 μM ROCK inhibitor Y-27632 (Selleck Chemicals, #S1049). Plates were centrifuged at 100 × g for 3 min and incubated at 37°C with 5% CO_2. After 24 h, organoids were transferred to Essential 6 medium (Thermo Fisher, #A1516401) supplemented with 2.5 μM dorsomorphin (Sigma-Aldrich, #P5499), 10 μM SB-431542 (R&D Systems, #1614), and 1.25 μM XAV-939 (Tocris, #3748) for 5 days with daily media changes.

Patterning and differentiation into hCOs and hStrOs

On day 6, organoids were transferred into ultralow-attachment 6-well plates (Corning, #3471) and maintained on an orbital shaker at 80 rpm thereafter. From day 6 to day 21, organoids were cultured in neural medium containing Neurobasal-A (Thermo Fisher, #10888022), B-27 without vitamin A (Thermo Fisher, #12587010), GlutaMAX (1:100, Thermo Fisher, #35050061), and penicillin-streptomycin (1:100, Thermo Fisher, #15140122). For hCOs, this medium was supplemented with 20 ng/mL FGF2 (R&D Systems, #233-FB-500) and 20 ng/mL EGF (R&D Systems, #236-EG). For hStrOs, this medium was supplemented with 2.5 μM WNT inhibitor IWP-2 (Selleck Chemicals, #S7085) and 50 ng/mL recombinant Activin A (PeproTech, #120-14P). From day 12 to day 21, hStrOs were treated with 100 nM SR11237 (Tocris, catalog no. 3411).

Neuronal differentiation and maturation

From day 22 to day 45, neural progenitors were differentiated into neurons for both hCOs and hStrOs by supplementing the neural medium with BDNF (20 ng/mL, PeproTech, #450-02), NT-3 (20 ng/mL, PeproTech, #450-03), ascorbic acid (200 μM, Wako, #323-44822), Dibutyryl-cAMP (50 μM, Santa Cruz, #sc-201567A), and DHA (10 μM, MilliporeSigma, #D2534). From day 43 to day 45, 2.5 μM DAPT (Stemcell Technologies, #72082) was additionally added to hStrO along with BDNF, NT-3, ascorbic acid, cAMP, and DHA. From day 46 onward, cultures were maintained in a neural medium containing B-27 Plus Supplement (Thermo Fisher, #A3582801) with medium changes every 4–5 days.

Viral labeling and live-cell imaging of cortico-striatal assembloids

Unless otherwise indicated, each AAV vector was added at 1 μL per organoid (5×10^{12} vg/mL; 5×10^{9} vg/organoid).

Generation of cortico-striatal assembloids

To generate cortico-striatal assembloids, virally labeled organoids were washed three times with fresh medium to remove residual extracellular viral particles before fusion. One hCO and one hStrO were transferred into a 1.5-mL Eppendorf tube containing 1 mL neural medium and incubated at 37°C for 3–4 days with a complete medium change on day 2.[14] Once formed, assembloids were transferred to ultralow-attachment plates using a P1000 pipette with a cut tip to accommodate their size. Assembly was conducted between days 60–76 of differentiation.

Generation of genotype-defined mix-and-match cortico-striatal assembloids

To distinguish cortical and striatal contributions to *SCN2A*-dependent phenotypes, genotype-defined mix-and-match cortico-striatal assembloids were generated by combining hCOs and hStrOs of different genotypes. Depending on the experiment, hCOs and

Please cite this article in press as: Chen et al., Autism-associated *SCN2A* deficiency disrupts cortico-striatal circuitry in human brain assembloids, Neuron (2026), https://doi.org/10.1016/j.neuron.2026.08.031

hStrOs were paired to generate WT hCO–WT hStrO, HET hCO–WT hStrO, WT hCO–HET hStrO, or HET hCO–HET hStrO assembloids. hCOs were transduced with AAV1-hSyn::Cre, and hStrOs were transduced with AAV1-Ef1a-DIO-mScarlet. Organoids were fused between days 60–76 of differentiation as described above. Dendritic spine imaging of mScarlet-positive striatal receiver neurons was performed at least 30 days after fusion. Spine density was quantified by Neurolucida 360 and Neurolucida Explorer (MBF Bioscience). Experiment-specific line usage is summarized in Table S2.

Anterograde and retrograde tracing

For anterograde labeling, on day 60, hCOs were labeled with AAV1-hSyn::Cre (Addgene viral prep #105553-AAV1), while hStrOs were labeled with AAV1-Ef1a-DIO-mScarlet (Addgene viral prep #131002-AAV1) and AAV9-hSyn-EGFP (Addgene viral prep #50465-AAV9). For retrograde labeling, hStrOs were labeled with AAVrg-hSyn::Cre (Addgene viral prep #105553-AAVrg), while hCOs were labeled with AAV1-Ef1a-DIO-mScarlet and AAV9-hSyn-EGFP. Assembloids were maintained in culture with medium changes every 4 days. After 1 month, labeled assembloids were transferred to glass-bottom 24-well plates (Cellvis, #P24-0-N) in BrainPhys medium (STEMCELL, #5790) and imaged using a Zeiss LSM 900 confocal microscope (10× objective, Z-stack scanning) following a 15-min equilibration at 37°C and 5% CO_2.

Axonal projection imaging

To assess projections from hCO to hStrO, hCOs were labeled with AAV1-hSyn-mScarlet (Addgene viral prep #131001-AAV1) on day 60, assembled with hStrO on day 65, and imaged on days 10, 20, 30, and 42 post-fusion for the *SCN2A*-C959X series and on days 25, 35, and 45 post-fusion for the *SCN2A*-R524X series using a Zeiss LSM 900 confocal microscope with a 10× objective and 0–500 μm Z-stack scanning. Confocal Z-stacks were converted into two-dimensional Z-projection images using ZEN software (Carl Zeiss). The hStrO compartment was manually delineated as a two-dimensional ROI, and the mScarlet-positive area within the ROI was quantified using Fiji/ImageJ (v1.53t; NIH), with the same fluorescence threshold for all images within each experimental batch. Projection coverage was calculated as the percentage of mScarlet-positive area relative to the total hStrO ROI area. WT and mutant assembloids were processed, transduced, imaged, and analyzed in parallel using the same viral preparation, viral dose, transduction timing, culture conditions, imaging settings, and quantification pipeline to minimize potential systematic differences in viral labeling or image acquisition.

Receiver and non-receiver neuron labeling and live-cell dendritic spine imaging

hCOs were labeled with AAV1-hSyn::Cre, while hStrOs were labeled with AAV1-Ef1a-DIO-mScarlet and AAV9-hSyn-EGFP on day 60, followed by fusion on day 65. After 1 month, $EGFP^+$/$mScarlet^-$ neurons were classified as non-receivers, whereas mScarlet-positive hStrO neurons were classified as receivers based on Cre-dependent labeling. For live-cell dendritic spine imaging, assembloids were transferred to BrainPhys medium and imaged using a Zeiss LSM 900 confocal microscope at 0–500 μm depth Z-stack scanning with a 20× objective and 6× zoom. For receiver-only spine imaging experiments, hCOs were labeled with AAV1-hSyn::Cre, while hStrOs were labeled with AAV1-Ef1a-DIO-mScarlet before fusion, and mScarlet-positive striatal receiver neurons were imaged under the same conditions.

CAV-2 vector transduction

Brain organoids were transduced with either control CAV-2-NSE-mCitrine (CAV-Ctrl) or CAV-2-NSE-*SCN2A*-HA (CAV-*SCN2A*). Both vector preparations were normalized to a titer of 5×10^{11} physical particles (pp)/mL. Depending on organoid size, control organoids received 1–2 μL of CAV-Ctrl, whereas rescue organoids received 1–2 μL of CAV-*SCN2A*. Vectors were added directly to the culture medium on day 60, and organoids were incubated for 24–48 h before assembly. Samples were collected on day 120 for qPCR and western blotting. For dissociated 2D cultures used for electrophysiological recordings, control cultures received CAV-Ctrl alone, whereas rescue cultures were co-transduced with CAV-Ctrl and CAV-*SCN2A* to enable targeted patch-clamp recording from mCitrine-positive neurons. CAV-2 vectors were applied at 400–800 pp per cell for 24–48 h, and electrophysiological recordings were performed 7 days after transduction.

Patch-clamp recordings

Acute slice preparations

Slices were prepared from 3- to 12-month-old brain organoids and hCO-hStrO assembloids. Organoids and assembloids were rapidly embedded in 4% agarose in slicing solution containing (in mM): 110 choline chloride, 2.5 KCl, 1.25 NaH_2PO_4, 25 $NaHCO_3$, 0.5 $CaCl_2$, 7 $MgCl_2$, 25 glucose, 1 sodium ascorbate, and 3.1 sodium pyruvate (pH 7.4, 305–315 mOsm, bubbled with 95% O_2 and 5% CO_2). 200-μm slices were prepared using a vibratome (Leica VT1200 S, Germany). Slices were incubated for 10 min at 33°C in slicing solution, then transferred to artificial cerebrospinal fluid (aCSF; in mM; 125 NaCl, 2.5 KCl, 1.25 NaH_2PO_4, 25 $NaHCO_3$, 2.0 $CaCl_2$, 2.0 $MgCl_2$, 10 glucose; pH 7.4, 305–315 mOsm, bubbled with 95% O_2 and 5% CO_2) for 10–20 min at 33°C before storage at room temperature for at least 30 min prior to recording.

Whole-cell electrophysiology in organoid and assembloid slices

Whole-cell recordings were performed in acute slices prepared from hCOs, hStrOs, and hCO-hStrO assembloids. Slices were transferred to a recording chamber continuously perfused with aCSF at 32–33°C (2–3 mL/min). Neurons were visualized with an IR-DIC microscope (Olympus BX-51WI) equipped with an IR-2000 camera (Dage-MTI). Somatic whole-cell patch-clamp recordings were obtained from cortical pyramidal-like neurons and striatal MSN-like neurons. Cortical pyramidal-like neurons were identified by their characteristic morphology, including a prominent apical dendrite, whereas MSN-like neurons were identified by their medium-sized somata and spiny dendritic morphology. Thin-wall borosilicate pipettes (BF150-110-10, Sutter Instruments) with an open-tip resistance of 3–5 MΩ were fabricated using a P-1000 puller (Sutter Instruments).

Please cite this article in press as: Chen et al., Autism-associated *SCN2A* deficiency disrupts cortico-striatal circuitry in human brain assembloids, Neuron (2026), https://doi.org/10.1016/j.neuron.2026.08.031

For sEPSC recordings, pipettes were filled with a Cs-based internal solution containing the following (in mM): 120 $CsMeSO_3$, 4 $MgCl_2$, 0.2 EGTA, 10 HEPES, 4 Na_2ATP, 0.3 $Tris_3$-GTP, 14 $Tris_2$-phosphocreatine, adjusted to pH 7.25 with CsOH (295–305 mOsm). Neurons were voltage-clamped at −80 mV, near the estimated chloride reversal potential under these recording conditions, and inward sEPSCs were recorded for 3 min in gap-free mode. Data were acquired using an Axon MultiClamp 700B amplifier, Digidata 1550B plus HumSilencer digitizer, and pClamp 11.4 software (Molecular Devices), filtered at 2 kHz, sampled at 33 kHz, and analyzed using Mini Analysis Program v6.08 (Synaptosoft). Recordings were included only when series resistance remained stable between 15 and 30 MΩ; recordings with Rs changes >20% were excluded.

For chemogenetics experiments, hCOs were labeled with AAV9-hSyn-hM3D(Gq)-mCherry (Addgene viral prep #50474-AAV9), while hStrOs were labeled with AAV9-hSyn-EGFP on day 60, followed by assembly on day 65. After 2 months, assembloids were prepared for sEPSC recordings. EGFP-positive MSN-like neurons in hStrO, surrounded by mCherry-labeled axons, were selected for recording. Baseline activity was recorded for 3 min, followed by bath application of 10 μM CNO for 3 min and a 3-min washout.

For evoked EPSC recordings, striatal receiver neurons in acute hCO–hStrO assembloid slices were identified by viral labeling as described above. A bipolar stimulation electrode was positioned in the hCO compartment near cortical axon bundles projecting toward the hStrO compartment. Brief electrical stimuli were delivered at low frequency, 0.05–0.1 Hz, using a Digitimer DS3 stimulator through an A-M Systems electrode. Stimulation parameters were 800 μs pulse duration and 1–3 mA intensity. Evoked EPSCs were quantified as the peak inward current within a defined post-stimulus window, and responses from repeated trials were averaged for each neuron.

For current-clamp recordings, pipettes were filled with a K-based internal solution containing the following (in mM): 122 $KMeSO_4$, 4 KCl, 2 $MgCl_2$, 0.2 EGTA, 10 HEPES, 4 Na_2ATP, 0.3 Tris-GTP, and 14 Tris-phosphocreatine, adjusted to pH 7.25 with KOH, 295–305 mOsm. Signals were sampled at 50 kHz and filtered at 2 kHz. Sag ratio, input resistance, and firing properties were assessed using 400-ms hyperpolarizing and depolarizing current steps from −100 to +300 pA in 50-pA increments (or from −40 to +140 pA in 20-pA increments depending on recording condition), with 5-s sweep intervals. Recordings were performed at the RMP or a holding potential of −70 mV or −80 mV, as indicated. Input resistance (R_{input}) was calculated from the voltage response to a −100 pA or −20 pA current step using:

$$R_{input} = \frac{(V_{steady-state} - V_{baseline})}{I_{step}}$$

where I_{step} was −100 pA or −20 pA, depending on the protocol used for that cell. $V_{baseline}$ was the RMP or holding potential, and $V_{steady\text{-}state}$ was measured during the final 10 ms of the corresponding hyperpolarizing step. Membrane capacitance (C_m) was obtained from the amplifier membrane test. AP properties were measured from the intact spike evoked by a 20-ms rheobase current step. Sweeps were 1.5 s in duration with 10-s start-to-start intervals, and cells were held at the RMP, −70 mV, or −80 mV as indicated. RMP, AP threshold, amplitude, fast afterhyperpolarization, half-width, maximum rise slope, and maximum decay slope were analyzed in Clampfit 11.4. Threshold was defined as the membrane potential at which d*V*/dt first exceeded 15 V/s.

For post hoc morphology, 0.1%–0.2% neurobiotin was included in the internal solution. After recording (~30 min), slices were fixed in 4% paraformaldehyde (pH 7.4) for 20–30 min at room temperature, washed in PBS, and incubated overnight at 4°C with Alexa 647-conjugated streptavidin (1:250 in blocking solution).[66] Neuronal morphology, including dendritic spines, of patched neurons was imaged under a Zeiss LSM 900 confocal microscope.

Whole-cell electrophysiology in dissociated neurons

Brain organoids were dissociated into single cells using a modified Worthington Papain Dissociation Kit (Papain Dissociation System, Worthington, LK003150). 3–5 randomly selected mature hCOs (>110 days old) were transferred to 60 mm dishes, and the excess medium was aspirated before adding 5 mL of Papain-DNase solution. The tissue was minced into <1 mm pieces and incubated at 37°C, 5% CO_2, shaking at 80 rpm for 30 min, and then gently triturated, followed by an additional 10-min incubation. The resulting suspension was transferred to a 15 mL conical tube, allowed to settle, and the supernatant was mixed with the inhibitor solution before centrifugation at 300 × g for 7 min. The pellet was resuspended in Neurobasal medium, filtered through a 40 μm strainer (CELLTREAT Scientific Products, #229481), and counted. Approximately 1–2 × 10^5 cells were seeded onto 12-mm round coverslips (Neuvitro, #GG-12-1.5-Pre) in 24-well plates. Neurons were cultured in Neurobasal medium with a B-27 supplement (without vitamin A) for 7 days, with half-medium changes every other day. From day 7, cells were maintained in Neurobasal medium with B-27 Plus Supplement, with half-medium changes twice a week.

After 2 weeks, neurons were transduced with a control vector (CAV-2-NSE-mCitrine at 400 or 800 pp per cell) or a 1:2 mixture of the control and *SCN2A*-expressing vectors (CAV-2-NSE-*SCN2A*-HA at 400 or 800 pp per cell). After 1 week of expression, mCitrine-positive neurons from control or CAV-*SCN2A*-treated cultures were selected for somatic whole-cell patch-clamp recordings. Recording solutions, acquisition settings, inclusion criteria, current-step protocols, and electrophysiological parameter analyses were the same as described above for current-clamp recordings in slices.

Biophysical characterization of hSCN2A-*HA*

HEK293-derived tsA201 cells were cultured in DMEM/F-12 supplemented with 10% fetal bovine serum and 1% penicillin–streptomycin. To compare the biophysical properties of untagged and C-terminal HA-tagged human *SCN2A*, cells were transiently transfected with CMV promoter-driven plasmids encoding full-length tetrodotoxin-resistant human *SCN2A* or C-terminal HA-tagged human *SCN2A* (*hSCN2A*-HA). The untagged *hSCN2A* construct was a gift from Stephen Waxman (Yale University) and was previously

Please cite this article in press as: Chen et al., Autism-associated *SCN2A* deficiency disrupts cortico-striatal circuitry in human brain assembloids, Neuron (2026), https://doi.org/10.1016/j.neuron.2026.08.031

described in a piggyBac vector with a GFP-2A reporter linker.[46] *hSCN2A*-HA was generated from this construct by PCR amplification using Q5 High-Fidelity DNA Polymerase (New England Biolabs, M0491), IDT oligonucleotides, and Gibson assembly using Gibson Assembly Master Mix (New England Biolabs, E2611S). Plasmids were purified using the QIAprep Spin Miniprep Kit (Qiagen, 27106) and validated by Sanger sequencing. Cells were transfected with 400 ng plasmid DNA using Lipofectamine 3000 Transfection Reagent (Thermo Fisher Scientific, L3000001). 24 h after transfection, cells were dissociated with 0.25% trypsin (Corning, 25-053-CI) and plated onto poly-D-lysine-coated coverslips (Corning, 354086) for whole-cell patch-clamp recording.

Whole-cell voltage-clamp recordings were performed at room temperature using an EPC10 amplifier and PatchMaster software (HEKA Elektronik). GFP-positive cells were selected for recording. Borosilicate glass pipettes had open-tip resistances of 2–4 MΩ. The extracellular solution contained (in mM): 140 NaCl, 3 KCl, 1 $CaCl_2$, 1 $MgCl_2$, 10 HEPES, and 20 dextrose, adjusted to pH 7.3 with NaOH and 320 mOsm. The internal solution contained (in mM): 140 CsF, 10 NaCl, 1.1 EGTA, 10 HEPES, and 20 dextrose, adjusted to pH 7.3 with CsOH and 310 mOsm. Leak currents were subtracted using a P/N protocol. Sodium currents were evoked from a holding potential of −100 mV using 10 ms depolarizing steps from −80 mV to +50 mV in 5 mV increments. Peak current density was calculated by normalizing peak current amplitude to cell capacitance. Sodium conductance (G_{Na}) was calculated as:

$$G_{Na} = \frac{I_{Na}}{(V_m - V_{rev})}$$

where I_{Na} is the peak sodium current, V_m is the test potential, and V_{rev} is the measured reversal potential. Conductance–voltage relationships were normalized to maximal conductance and fitted with a Boltzmann function to determine the voltage of half-maximal activation (V_{50}) and slope factor. Steady-state fast inactivation was assessed using 500 ms prepulses from −140 to −5 mV, followed by a test pulse to +5 mV. Currents were normalized to maximal current and fitted with a Boltzmann function to determine the voltage of half-maximal fast inactivation (V_{50}) and slope factor.

High-density microelectrode array (HD-MEA) recording of cortico-striatal assembloids

HD-MEA preparation and assembloid seeding

HD-MEAs (3Brain, 6-well plates) were cleaned with 1% Tergazyme (200 μL/well, 37°C, 1 h), rinsed three times with ultrapure water, disinfected in 70% ethanol for 1 h, dried, and incubated overnight in PBS at room temperature. HD-MEAs were coated sequentially with poly-L-ornithine (50 μg/mL; Sigma-Aldrich, #P4957) overnight, washed, and further coated with laminin (50 μg/mL, ≥2 h at 37°C).

Cortico-striatal (hCO-hStrO) assembloids (~4 months old) were transferred onto HD-MEAs using a wide-bore pipette and allowed to settle for 2 h. To promote attachment, 20 μL of medium was added every 2 h for 8 h, followed by 2 mL of medium the next day. Cultures were maintained in BrainPhys medium supplemented with N2, B27 Plus, 50 μM cAMP, and 200 μM ascorbic acid, with twice-weekly media changes. Recordings were conducted after 2 weeks of culture.

Electrophysiological recordings and analysis

On the day of recording, the media was refreshed, and the plate was incubated at 37°C with 5% CO_2 for 15 min. Extracellular activity was recorded for 5 min using Brainwave V software (v5.6, 3Brain AG, Switzerland) on a HyperCAM Alpha multi-well system with CorePlate 6W 38/60 HD-MEA plates. Recordings were acquired from up to 2,304 electrodes per well at a 10 kHz sampling rate using 6-well HD-MEA plates with 60 μm electrode pitch, with 100 Hz high-pass and 20–5000 Hz band-pass filtering. Fast Fourier Transform (FFT) with a Hamming window was applied for spectral analysis.

Spikes were detected using an 8.0 standard deviation threshold, with a peak lifetime of 2.0 ms, a refractory period of 1.0 ms, and a pre-peak wave duration of 1.0 ms. Electrodes with spike frequencies < 0.083 Hz (5 spikes/min) were excluded. Bursts were identified as ≥5 spikes with an interspike interval ≤100 ms, while network bursts were detected via a recruitment-based algorithm requiring ≥10% electrode activation and a minimum burst size of 50 spikes. Spike sorting was performed using Principal Component Analysis (PCA, 3 components) and *K*-Means clustering with Gap Statistics.

Cryoprotection, immunocytochemistry, and imaging analysis

Sample preparation

Brain organoids and assembloids were fixed in 4% paraformaldehyde (PFA) in PBS overnight at 4°C, washed in PBS, and transferred to 30% sucrose-PBS for 2–3 days until fully submerged. Samples were then equilibrated in a 1:1 mixture of optimal cutting temperature (OCT) compound (Tissue-Tek, 4583, Sakura Finetek) and 30% sucrose-PBS before embedding. After embedding, cryosections (20–40 μm thick) were obtained using a Leica CM1850 cryostat. Slices on glass coverslips for the 2D culture were fixed in 4% PFA for 20 min at room temperature.

Immunostaining

Cryosections were washed (3×, 5 min) in PBS, permeabilized, and blocked in either 0.5% Triton X-100 and 5% normal goat serum in PBS or 4% Block-Ace (Dainippon Sumitomo Pharma, UK-B80) with 0.05% Tween-20 in PBS for 1 h at room temperature. Primary antibodies were applied overnight at 4°C, followed by PBS washes (3×, 10 min). Samples were then incubated with Alexa Fluor-conjugated secondary antibodies for 1 h at room temperature in a blocking buffer. Sections were mounted with DAPI-containing Antifade Mounting Medium (VECTASHIELD, H-2000) and sealed with glass coverslips.[67] Images were acquired using an LSM900 confocal fluorescence microscope equipped with an Airyscan module (Carl Zeiss, Jena, Germany).

Please cite this article in press as: Chen et al., Autism-associated *SCN2A* deficiency disrupts cortico-striatal circuitry in human brain assembloids, Neuron (2026), https://doi.org/10.1016/j.neuron.2026.08.031

Axon initial segment (AIS) length quantification

Images were captured using a 63× oil-immersion objective, with Z-stacks collected from at least three regions per organoid. Maximum-intensity projections were generated from Z-stacks spanning the entire AIS. AIS length was defined by ankyrin-G immunofluorescence and measured between the proximal and distal endpoints using the segmented-line tool in Fiji/ImageJ (v1.53t; NIH).[32] Only AISs with clearly defined endpoints were included.

Synaptic density quantification

Synaptic density was assessed using a 63× oil-immersion objective with 1.3× zoom and an Airyscan module. For each organoid, 3–6 regions of interest were imaged using identical acquisition settings across WT and mutant samples. Colocalized excitatory presynaptic (SYN1) and postsynaptic (PSD95) puncta were quantified using ZEN 3.1 Blue Edition software (Carl Zeiss Microscopy) with consistent analysis parameters within each batch. The density of colocalized puncta was normalized to the corresponding WT group to assess genotype-dependent changes.

Quantification of compartment-specific immunostaining

For compartment-specific immunostaining analyses, images were acquired using identical microscope settings within each experiment and analyzed in Fiji software. In hCO–hStrO assembloids, hCO and hStrO compartments were manually outlined as separate ROIs based on morphology and marker distribution. For SATB2 quantification, matched high-magnification ROIs were selected from the hCO and hStrO compartments. Because SATB2 is a nuclear transcription factor, DAPI-positive nuclei were segmented in Fiji/ImageJ to generate nuclear masks. SATB2 fluorescence intensity was then measured within each DAPI-defined nuclear mask using the original, unadjusted images. SATB2-positive nuclei were identified using a conservative batch-level nuclear intensity cutoff derived from the pooled hStrO nuclear SATB2 signal, defined as the mean plus five standard deviations, and the same cutoff was applied to all hCO and hStrO ROIs. SATB2 expression was quantified as the percentage of SATB2-positive nuclei among total DAPI-positive nuclei within each ROI. For DARPP32, because the signal is cytoplasmic and neurite-associated, DARPP32-positive area was measured as the percentage of positive area within each matched ROI using identical thresholding parameters for all images from the same batch. For $Na_V1.2$ compartmental analysis, mean $Na_V1.2$ fluorescence intensity was measured separately in the hCO and hStrO ROIs and normalized to the corresponding NeuN signal from the same compartment within the same assembloid. For apoptosis analysis, CC3-positive nuclei were quantified as a percentage of total DAPI-positive nuclei within the analyzed ROI. For VGAT-associated DARPP32-positive neuron analysis, NeuN-positive neurons were first identified, followed by the identification of DARPP32-positive neurons. Because VGAT labeling appeared as puncta rather than a uniform somatic signal, VGAT association was defined as punctate VGAT fluorescence above local background adjacent to DARPP32-positive neurons, rather than complete somatic overlap. VGAT-associated DARPP32-positive neurons were quantified as a percentage of total NeuN-positive neurons in the analyzed image. For each experiment, multiple ROIs or images were analyzed from each organoid or assembloid using identical acquisition and analysis settings within the same batch. The unit of quantification and sample size are indicated in the corresponding figure legends.

Post hoc spine imaging of patched neurons

For post hoc spine analysis, the internal solution contained 0.1%–0.2% neurobiotin. After whole-cell recording, slices were fixed in 4% paraformaldehyde, washed in PBS, and incubated with Alexa 647-conjugated streptavidin to visualize patched neurons. Dendritic spines were imaged on a Zeiss LSM 900 confocal microscope using a 63× oil-immersion objective.

Sholl analysis and dendritic spine classification

Confocal Z-stacks were converted into two-dimensional Z-projection images using ZEN software (Carl Zeiss). Neuronal morphology and dendritic spines were analyzed from the Z-projection images using Neurolucida 360 v2023.1.1 and Neurolucida Explorer v2022.2.1 (MBF Bioscience). For Sholl analysis, neurons with clearly resolved somata and dendritic arbors were reconstructed, and total dendritic length, branch structure, and Sholl intersections were quantified.

For dendritic spine analysis, fluorescently labeled neurons were imaged either in intact cortico-striatal assembloids by live-cell confocal imaging or from post hoc neurobiotin-filled patched neurons, as indicated in the figure legends. Under genotype-mixing conditions, spine analysis was performed on mScarlet-positive receiver neurons within intact assembloids. Clearly traceable dendritic segments were selected using the same image-quality criteria across genotypes and experimental conditions. When possible, at least three dendritic segments were analyzed per assembloid.

Spine quantification was performed by an investigator blinded to genotype and experimental condition, and dendritic segment selection and spine calls were reviewed by a second blinded investigator. Each protrusion was manually inspected and classified as filopodia, thin, stubby, mushroom, or branched according to standard morphological criteria. Ambiguous puncta, crossing processes, isolated fluorescent structures, or protrusions not clearly continuous with the dendritic shaft were excluded. Total and subtype-specific spine densities were calculated as spine number per micrometer of dendritic length. The unit of quantification and sample size are indicated in the corresponding figure legends.

Western blotting

Organoids and assembloids were homogenized in ice-cold RIPA buffer (Thermo Fisher, 89901) with protease and phosphatase inhibitors (Thermo Fisher, A32953) and centrifuged at 10,000 × g for 20 min at 4°C. Protein concentrations were determined using the Pierce BCA Protein Assay Kit (Thermo Fisher, 23225). Proteins were denatured in 1× Laemmli buffer (62.5 mM Tris-HCl (pH 6.8), 2% SDS, 5% glycerol, 0.05% bromophenol blue) by boiling at 95°C for 5 min. Then, 50 μg of each sample was loaded onto 8% SDS-PAGE gels at 80–120 V and transferred onto PVDF membranes (Thermo Fisher, PB9220) at 300 mA for 2.5 h at 4°C. Membranes

Please cite this article in press as: Chen et al., Autism-associated *SCN2A* deficiency disrupts cortico-striatal circuitry in human brain assembloids, Neuron (2026), https://doi.org/10.1016/j.neuron.2026.08.031

were blocked with 5% nonfat milk in TBST (Tris-buffered saline with 0.1% Tween 20) for 1 h at room temperature and incubated overnight at 4°C with primary antibodies diluted in Intercept T20 (TBS) Antibody Diluent (LI-COR Biosciences, 927-65001). The next day, blots were washed (3×, 10 min) in TBST, incubated with secondary antibodies for 1 h at room temperature, and washed again (3×, 10 min). Immunoreactive bands were visualized using the Odyssey CLx Imaging System (LI-COR Biosciences).

For immunoblot quantification, band intensities were measured in Fiji/ImageJ (v1.53t; NIH) from uncropped images acquired under non-saturating conditions. The $Na_V1.2$ signal was normalized to the corresponding loading control from the same lane. β-actin was used as the loading control for blots from whole organoid or assembloid lysates, whereas TUJ1 was used as a neuronal loading control where indicated. Normalized values were then expressed relative to the WT or control group within each experiment.

RNA isolation, reverse transcription, and qPCR analysis

Total RNA was extracted from hCO-hStrO assembloids using the RNeasy Mini Kit (QIAGEN, #74104) following the manufacturer's protocol. RNA concentration and purity were assessed using a NanoDrop spectrophotometer (Thermo Fisher). cDNA was synthesized using the Maxima First Strand cDNA Synthesis Kit (Thermo Fisher, #K1672) on a T100 Thermal Cycler (Bio-Rad).

Quantitative PCR (qPCR) was performed using THUNDERBIRD SYBR qPCR Mix (TOYOBO, Code QPS-201) and gene-specific primers on a CFX96 Real-Time PCR Detection System with a C1000 Touch Thermal Cycler base (Bio-Rad). qPCR data were analyzed using Bio-Rad CFX Maestro v4.1.2433.1219. Thermal cycling conditions were as follows: initial denaturation at 95°C for 1 min, followed by 45 cycles of 95°C for 15 s and 60°C for 60 s. Primer sets included internal *SCN2A* (forward: GAGACCATGTGGGACTGTATG; reverse: AAGGCCAAGAAGAGGTTCAG), codon-optimized *SCN2A* (forward: GTGTTTTGCCTCTCCGTGTT; reverse: ATTTCCGTCCAGGGAGTTGT), and total *SCN2A* (forward: GGATACATCTGTGTGAAGGC; reverse: CTGTTCCTCATAGGCCAT).

Gene expression levels were normalized to *GAPDH*. Each biological sample was analyzed in technical duplicate, and the mean C_t value was used for calculation. Relative expression was calculated using the $2^{-\Delta\Delta Ct}$ method:

$$\Delta C_t = C_{t,\text{target gene}} - C_{t,GAPDH}$$

$$\Delta\Delta C_t = \Delta C_{t,\text{sample}} - \Delta C_{t,\text{calibrator}}$$

$$\text{Relative expression} = 2^{-\Delta\Delta C_t}$$

The mean ΔC_t of the relevant WT or control group was used as the calibrator.

Xenium spatial transcriptomic profiling and analysis

One hCO collected on day 83 and five hStrOs collected between days 90 and 140 were formalin-fixed, paraffin-embedded, and sectioned for Xenium analysis. One section from each organoid was mounted on a Xenium slide and analyzed using the Xenium *in situ* platform (10x Genomics) with the Xenium Prime 5K Human Pan Tissue and Pathways Panel (10x Genomics, PN:1000671), Xenium Slides & Sample Prep Reagents (10x Genomics, PN:1000460), and Xenium Cell Segmentation Staining Reagents (10x Genomics, PN:1000661), according to the manufacturer's instructions. Primary data processing, including transcript decoding, cell and nuclear segmentation, and image alignment, was performed on the Xenium Analyzer. Data visualization and downstream analysis were performed using Xenium Explorer v4.1.1.

Marker-based cell-type annotation of Xenium data

Xenium output files from individual organoids were imported for downstream analysis. Analysis was performed in Python v3.14.3 using Scanpy v1.12, igraph v1.0.0 for Leiden clustering, and matplotlib v3.10.8 for visualization, following standard preprocessing steps adapted from the 10x Genomics Xenium workflow. For both hCO and hStrO datasets, cells with fewer than 100 detected genes or with total transcript counts above the 98th percentile were excluded. For hCO datasets, genes detected in fewer than 50 cells were also removed; no gene-level filtering was applied to hStrO datasets. Marker positivity was defined as at least one detected transcript per cell. Unsupervised clustering was performed using Leiden clustering.[47,48] Cluster-level marker expression was visualized by dot plots with dendrogram-based hierarchical grouping. For hStrO datasets, all samples were batched together before analysis, and batch correction was performed using HarmonyPy version 0.0.10, based on the Harmony algorithm.[62] The same marker-based hierarchical annotation criteria were applied uniformly across samples, and each annotated cell class was quantified as a percentage of total analyzed cells per organoid.

For hCO datasets, cells were annotated hierarchically by first identifying neurons and then separating glutamatergic and GABAergic populations. Glutamatergic neurons were defined as *STMN2*-positive cells expressing *SLC17A7* and/or *SLC17A6*, whereas GABAergic neurons were defined as *STMN2*-positive cells expressing *GAD1* and/or *GAD2*. Glutamatergic neurons were further subclassified as *SATB2*-enriched, *BCL11B*-enriched, *TBR1*-enriched, or other glutamatergic neurons based on canonical marker expression. For hStrO datasets, MSN-like GABAergic neurons were defined as *GAD1*- or *GAD2*-positive cells co-expressing one or more striatal/MSN-associated markers, including *PPP1R1B*, *BCL11B*, or *FOXP1*. Non-MSN GABAergic neurons were defined as *GAD1*- or *GAD2*-positive cells lacking these MSN-associated markers. Progenitors were defined as cells positive for at least one progenitor marker, including *GSX2*, *ASCL1*, *SOX2*, or *HOPX*. Astroglial cells were defined by *AQP4* expression. Oligodendrocyte-lineage cells were defined by expression of *OLIG2* or *SOX10*. Glutamatergic neurons were defined as *SLC17A7*- and/or

SLC17A6-positive cells lacking *GAD1* and *GAD2* expression. Cells that did not meet criteria for the defined marker-based classes were grouped as Other. For cells with overlapping progenitor, astrocyte, and oligodendrocyte marker expression, cell identity was assigned based on the marker gene with the highest expression z-score. For hCO spatial analyses, annotated glutamatergic neuronal subgroups were used for boundary-distance analysis. For hStrO datasets, each annotated cell class was quantified as a percentage of total analyzed cells per organoid.

Boundary-distance analysis

For hCO spatial analysis, the outer organoid boundary was delineated from the Xenium morphology image. For each annotated glutamatergic neuron, the distance from the cell centroid to the nearest point on the outer organoid boundary was calculated using Python v3.14.3. Distances were reported in micrometers and compared across *SATB2*-, *BCL11B*-, and *TBR1*-enriched neuronal subgroups.

Bulk RNA sequencing and analysis

RNA extraction and library preparation

Total RNA was extracted from 5-month-old hCO-hStrO assembloids using the RNeasy Mini Kit (QIAGEN, Cat# 74104). Samples included 21 assembloids ($n = 7$ per genotype; three hiPSC lines per genotype) from two independent differentiation batches. Polyadenylated (Poly(A)$^+$) RNA was isolated from 100–250 ng of total RNA using the NEBNext Poly(A) mRNA Magnetic Isolation Module (New England Biolabs). RNA fragmentation and elution were performed directly from the oligo dT beads as part of the library construction process using the xGen RNA Library Preparation Kit (Integrated DNA Technologies, IDT) according to the manufacturer's instructions. Prepared libraries were pooled and sequenced on an Illumina NovaSeq X+ system, generating 30–36 million paired-end 2×150 bp reads per sample. The background comprised all genes retained for differential expression analysis.

Preprocessing, alignment, and genotype verification

Raw FASTQ files were processed using fastp (v0.23.2)[49] to remove adapter sequences and trim low-quality bases (Phred score <30). Reads shorter than 50 bp after trimming were discarded. The remaining reads were aligned to the GRCh38 human reference genome (Ensembl release 104) using the STAR Aligner (v2.7.10a)[50] in two-pass mode to improve splice junction detection. To confirm the genotype of the C959X mutation in *SCN2A*, variant calling was performed using GATK HaplotypeCaller (v4.2.2.0)[51] with Joint Genotyping.[52] RNA-seq-derived genotype calls were consistent with the known WT, HET, and HOM genotypes.

Gene quantification and normalization

Read assignment to genomic features was performed using featureCounts (v1.6.1)[53] in paired-end, reverse-stranded mode. Initial exploratory analysis was conducted with DESeq2 (v1.34.0)[54] in R (v4.1.3),[55] to evaluate sample clustering and overall consistency. The raw count matrix was filtered to retain genes with at least five counts in at least two samples. Counts were upper-quartile normalized using the betweenLaneNormalization function in RUVSeq (v1.28.0).[56] Five factors of unwanted variation ($k = 5$) were estimated from deviance residuals using RUVr.

Differential expression and pathway analysis

A generalized linear model (GLM) regression approach was applied to the count data, incorporating mutation genotype as a covariate while adjusting for batch effects using RUVSeq factors ($k = 5$). edgeR (v3.36.0)[57] was used to fit a quasi-likelihood negative binomial model for differential expression analysis. Statistical significance was determined using the Benjamini–Hochberg method for multiple hypothesis correction. Genes with an FDR < 0.05 were classified as differentially expressed genes (DEGs). DE genes were analyzed for enrichment in KEGG and Reactome pathways, as well as Gene Ontology (GO) terms, using clusterProfiler (v4.10.0)[58] in R (v4.3.2). The background gene set included all genes detected after RUVSeq correction. Ingenuity Pathway Analysis (IPA)[59] was performed to provide curated insights into biological pathways and disease associations.

Data visualization

Heatmaps: Batch-effect-corrected counts per million (CPM) values were extracted using edgeR and visualized with the ComplexHeatmap package (v2.14.0)[60] in R (v4.2.1). Volcano Plots: Differential expression results were visualized using the EnhancedVolcano package (v1.16.0).[61] Network and Dot Plots: Pathway enrichment results were displayed using enrichplot (v1.22.0) and clusterProfiler (v4.10.0) to highlight key gene interactions.

QUANTIFICATION AND STATISTICAL ANALYSIS

Statistical analyses were performed using GraphPad Prism v10.4.1. Data distribution and variance similarity were assessed before the application of parametric tests. For comparisons between two groups, a paired *t* test, unpaired *t* test, Welch's *t* test, or Mann-Whitney test was used as appropriate. For comparisons among three or more groups, one-way ANOVA with Tukey's, Bonferroni's, or Dunnett's test was used as indicated. For datasets with two independent variables, two-way ANOVA with Šídák's or Tukey's test was used as indicated. For repeated-measures datasets with missing values or unequal sampling across conditions, mixed-effects analysis with Geisser-Greenhouse correction and Tukey's or Šídák's test was used as indicated. For spine subtype analyses involving multiple nonparametric comparisons, multiple Mann-Whitney tests with Holm-Šidák correction were used. Post hoc multiple-comparison tests were performed where appropriate following the primary analysis. Exact statistical tests, sample sizes, and significance thresholds for each dataset are indicated in the corresponding figure legends. Data are presented as mean ± SEM. Statistical significance was defined as $p < 0.05$. Significance levels are denoted as $^*p < 0.05$, $^{**}p < 0.01$, $^{***}p < 0.001$, and $^{****}p < 0.0001$.

Neuron, Volume *115*

Supplemental information

Autism-associated *SCN2A* deficiency disrupts cortico-striatal circuitry in human brain assembloids

Xiaoling Chen, Jingliang Zhang, Jiaxiang Wu, Morgan J. Robinson, Harish Kothandaraman, Ye-Eun Yoo, Iria M. Gonzalez Dopeso-Reyes, Thomas D. Buffenoir, Manasi S. Halurkar, Hui Yang, Zaiyang Zhang, Muhan Wang, Erin N. Creager, Harris D. Giles, Yuanrui Zhao, Maria I. Olivero-Acosta, Kyle W. Wettschurack, Zhefu Que, Jing Liu, Chongli Yuan, Allison J. Schaser, Nadia A. Lanman, Jean-Christophe Rochet, William C. Skarnes, Eric J. Kremer, and Yang Yang

Supplemental Figures

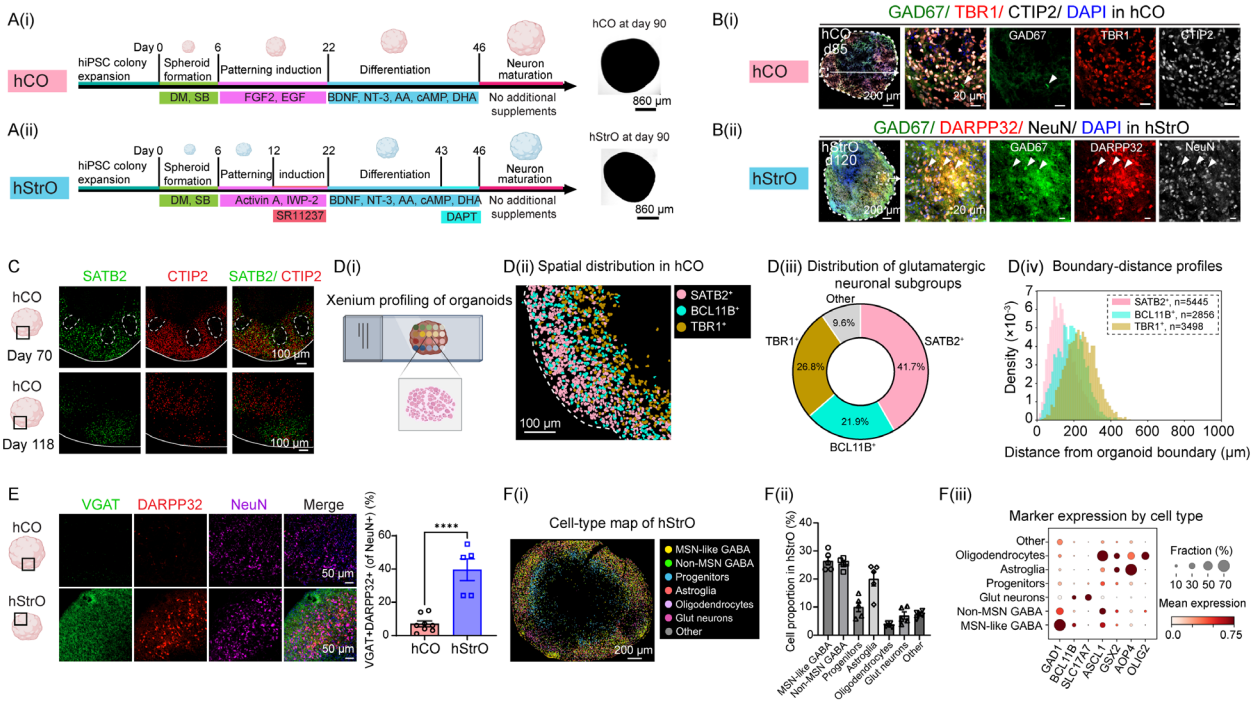


Figure S1. Characterization of human cortical and striatal organoids by immunostaining and spatial transcriptomic profiling, related to Figure 1.

(A) Differentiation schemes for cortical and striatal organoids. (A(i)) Schematic of the human cortical organoid (hCO) differentiation protocol. hiPSCs were directed through spheroid formation, patterning induction, differentiation, and neuronal maturation. Key supplements included dorsomorphin (DM), SB-431542 (SB), fibroblast growth factor 2 (FGF2), epidermal growth factor (EGF), brain-derived neurotrophic factor (BDNF), neurotrophin-3 (NT-3), ascorbic acid (AA), cyclic adenosine monophosphate (cAMP), and docosahexaenoic acid (DHA). A representative bright-field image of a day 90 hCO is shown on the right. Scale bar: 860 µm. (A(ii)) Schematic of the human striatal organoid (hStrO) differentiation protocol. hStrO patterning included recombinant Activin A, the WNT inhibitor IWP-2, and the retinoid X receptor agonist SR11237, followed by the γ-secretase inhibitor DAPT during later differentiation. A representative bright-field image of a day 90 hStrO is shown on the right. Scale bar: 860 µm.

(B) Immunostaining-based validation of cortical and striatal organoid identity. (B(i)) Immunostaining of hCOs showing GAD67 (green), TBR1 (red), CTIP2 (white), and DAPI (blue). hCOs showed sparse GAD67⁺ cells and abundant TBR1⁺ and CTIP2⁺ cortical neuronal markers. Higher-magnification views illustrate marker distribution within the spheroid. (B(ii)) Immunostaining of day 120 hStrOs showing GAD67 (green), DARPP32 (red), NeuN (white), and DAPI (blue). Higher-magnification views highlight enrichment of GAD67⁺ and DARPP32⁺ neuronal populations in hStrOs. Scale bars: 200 µm and 20 µm.

(C) Staining for upper-layer neurons (SATB2, green) and deep-layer neurons (CTIP2, red) in 70- and 118-day-old cortical organoids. Black boxes in the schematics indicate the imaged regions. Dashed outlines in day 70 images indicate progenitor zones. On day 70, progenitor zones are still present, and both neuronal populations reside outside these zones in a relatively disorganized pattern. By day 118, progenitor zones are no longer apparent, and SATB2⁺ and CTIP2⁺ neurons

exhibit a more organized laminar-like arrangement. Solid white lines mark the organoid boundary. Scale bar: 100 μm.

(D) Xenium spatial profiling defines the spatial distribution of glutamatergic neuronal subgroups in hCOs. (D(i)) Schematic of the Xenium spatial profiling workflow for hCO sections. (D(ii)) Representative Xenium image showing the spatial distribution of *SATB2*-enriched, *BCL11B*-enriched, and *TBR1*-enriched glutamatergic neurons in a hCO. Glutamatergic neuronal populations were defined as *STMN2*$^+$ cells expressing either *SLC17A7* or *SLC17A6* and were further subdivided based on *SATB2*, *BCL11B*, or *TBR1* expression. Scale bar: 100 μm. (D(iii)) Distribution of *SATB2*-enriched, *BCL11B*-enriched, and *TBR1*-enriched glutamatergic neurons in hCOs. Cells meeting glutamatergic neuronal criteria but lacking *SATB2*, *BCL11B*, and *TBR1* expression were grouped as Other glutamatergic neurons. (D(iv)) Boundary-distance profiles of *SATB2*-enriched, *BCL11B*-enriched, and *TBR1*-enriched glutamatergic neurons in hCOs. The distance of individual cells from the organoid boundary was quantified to compare the relative spatial distribution of each subgroup. The y-axis shows normalized density.

(E) Immunostaining of hCOs and hStrOs for VGAT (green), DARPP32 (red), and NeuN (magenta), with merged images shown on the right. Quantification shows the percentage of VGAT-associated DARPP32$^+$ cells among NeuN$^+$ neurons in hCOs and hStrOs. hCO, n = 8 organoids from 2 WT hiPSC lines; hStrO, n = 5 organoids from 1 WT hiPSC line. Unpaired t test. Scale bar: 50 μm.

(F) Xenium-based classification of cell populations in hStrOs. (F(i)) Representative Xenium cell-type map of a hStrO showing the spatial distribution of marker-defined cell populations. Cells were classified into MSN-like GABA neurons, non-MSN GABA neurons, progenitors, glutamatergic neurons, astroglia, oligodendrocytes, and Other based on predefined marker rules described in the Methods. Scale bar: 200 μm. (F(ii)) Quantification of the proportion of each annotated cell class in hStrOs across organoids. Total GABAergic neurons were calculated as the sum of MSN-like GABA and non-MSN GABA populations. Each dot represents one organoid; bars indicate mean ± SEM. (F(iii)) Dot plot showing representative marker expression across annotated cell classes. Dot size indicates the fraction of cells in each class expressing the indicated marker, and color indicates the mean expression level.

Data are presented as mean ± SEM. ****$p < 0.0001$.

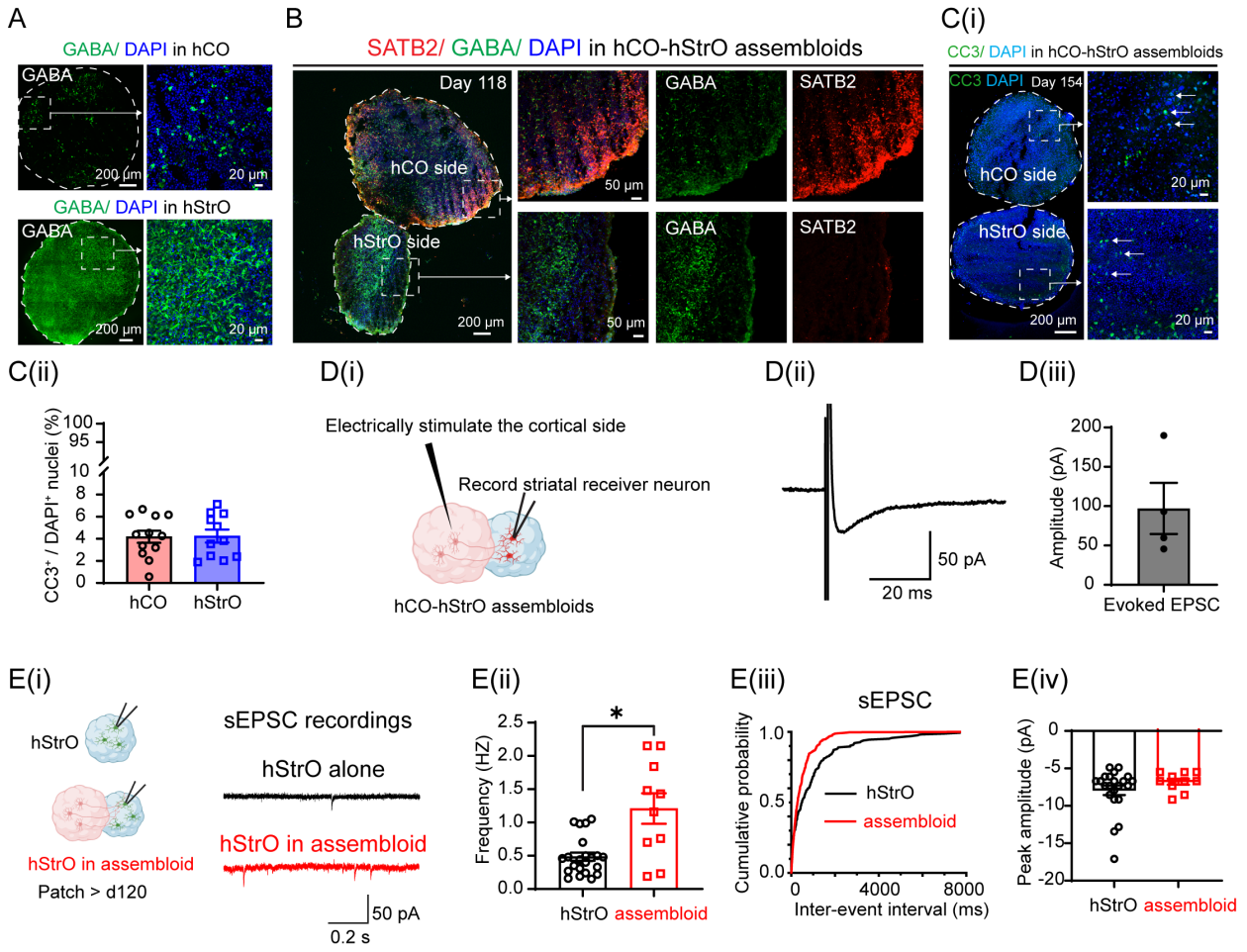


Figure S2. hCO-hStrO assembloids exhibit compartment-enriched GABA immunoreactivity and functional cortico-striatal connectivity, related to Figure 1.

(A) Representative GABA immunostaining in hCO and hStrO. Insets show lower GABA signal in hCOs and higher GABA signal in hStrOs. Dashed lines outline organoid boundaries. Scale bars: 200 μm and 20 μm. *n* = 3 organoids from 2 WT hiPSC lines with similar results.

(B) Representative immunostaining of day 118 hCO-hStrO assembloids for SATB2 (red), GABA (green), and DAPI (blue). Insets show SATB2 enrichment in the hCO side and GABA enrichment in the hStrO side. Scale bars: 200 μm and 50 μm. *n* = 4 assembloids from 3 WT hiPSC lines with similar results.

(C) Apoptosis analysis in hCO-hStrO assembloids. (C(i)) Immunostaining for cleaved caspase-3 (CC3; green) and DAPI (blue) in the hCO and hStrO compartments, with higher-magnification views of the boxed regions shown at right. Dashed lines indicate organoid boundaries. Scale bars: 200 μm and 20 μm. (C(ii)) Quantification of $CC3^+$ nuclei as a percentage of total $DAPI^+$ nuclei in hCOs and hStrOs. hCO: *n* = 12 images; hStrO: *n* = 12 images from 3 assembloids from 2 WT hiPSC lines; unpaired *t* test.

(D) Direct functional assessment of cortico-striatal connectivity by electrical stimulation. (D(i)) Schematic of the experimental design in which the cortical side of an hCO-hStrO assembloid (>120 days) was electrically stimulated while whole-cell patch-clamp recordings were obtained from a striatal receiver neuron. (D(ii)) Representative evoked excitatory postsynaptic current

(EPSC) recorded in a striatal receiver neuron following cortical stimulation. (D(iii)) Quantification of evoked EPSC amplitude. *n* = 4 cells from 4 assembloids from 2 WT hiPSC lines.

(E) Increased excitatory synaptic input onto hStrO neurons in assembloids. (E(i)) Schematic of whole-cell patch-clamp recordings from hStrO neurons in hStrO alone or in hCO-hStrO assembloids at >120 days, with representative spontaneous excitatory postsynaptic current (sEPSC) traces. (E(ii)) Quantification of sEPSC frequency. (E(iii)) Cumulative probability plot of sEPSC inter-event intervals. (E(iv)) Quantification of sEPSC peak amplitude. *n* = 22 cells from 3 hStrOs and *n* = 10 cells from 3 hCO-hStrO assembloids from 2 WT hiPSC lines. Welch's *t* test.

Data are presented as mean ± SEM. *$p < 0.05$.

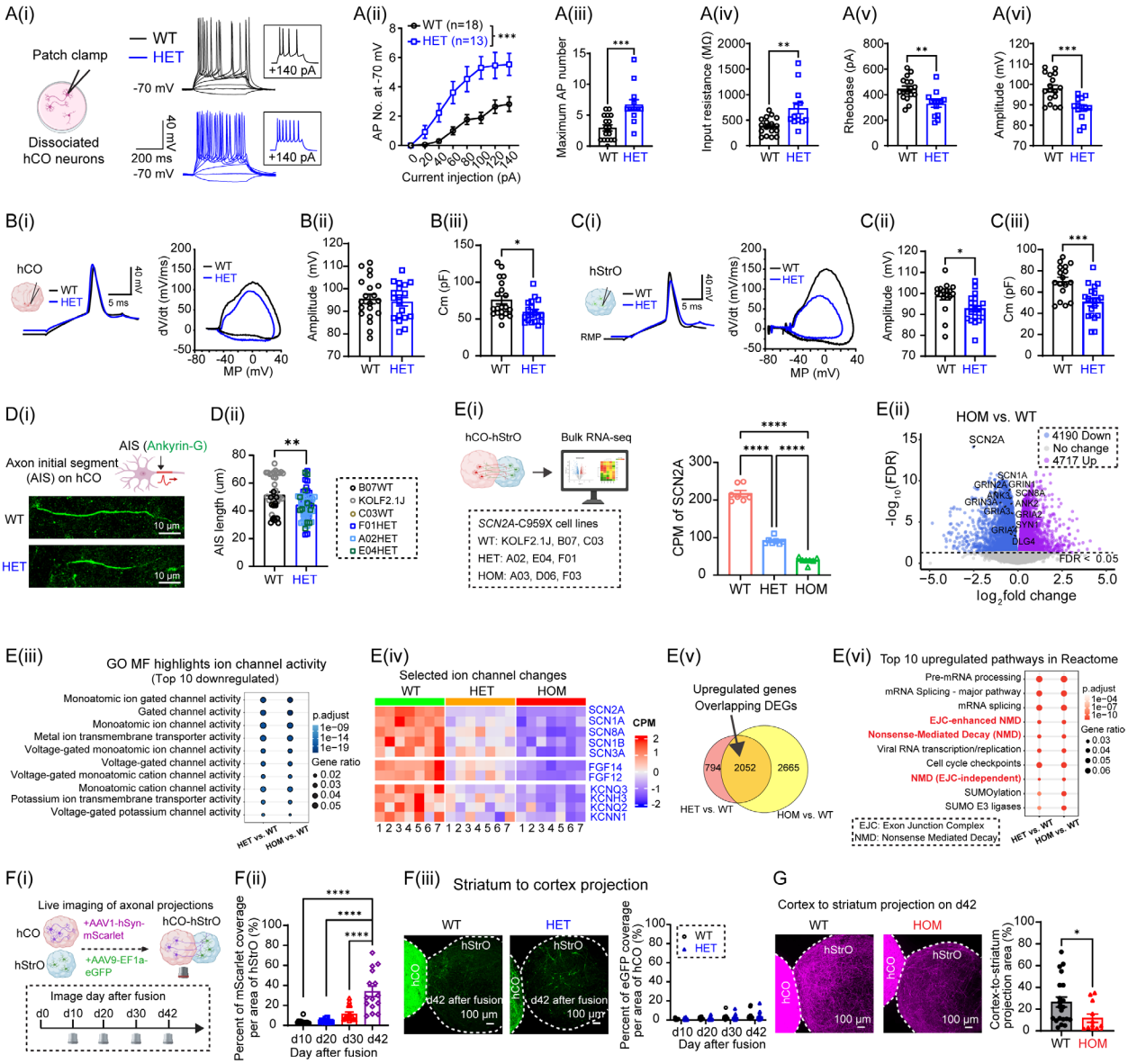


Figure S3. *SCN2A*-C959X increases intrinsic excitability, alters transcriptomic profiles, and impairs axonal projection, related to Figure 2.

HET and HOM denote the heterozygous and homozygous *SCN2A*-C959X lines, respectively.

(A) *SCN2A*-C959X increases intrinsic excitability in 2D dissociated cortical neurons. (A(i)) Schematic of whole-cell patch-clamp recording from 2D dissociated hCO neurons and representative firing traces from WT and HET neurons held at −70 mV and recorded in response to a series of depolarizing current injections. Insets show responses to a +140 pA current injection. (A(ii)) Quantification of evoked AP number across increasing current injections. WT: *n* = 18 cells; HET: *n* = 13 cells. Two-way ANOVA. (A(iii)–A(vi)) Quantification of maximal AP number, input resistance, rheobase, and AP amplitude. Same *n* as in A(ii). Mann–Whitney *U* tests for A(iii) and A(iv); unpaired *t* tests for A(v) and A(vi).

(B) Additional electrophysiological characterization of cortical neurons recorded at RMP. (B(i)) Representative single AP traces and corresponding phase plots from WT and HET hCO neurons.

(B(ii)) Quantification of AP amplitude. WT: *n* = 20 cells; HET: *n* = 19 cells. Welch's *t* test. (B(iii)) Quantification of membrane capacitance (C_m). Same *n* as in B(ii). Mann–Whitney *U* test.

(C) Additional electrophysiological characterization of striatal neurons recorded at RMP. (C(i)) Representative single AP traces and corresponding phase plots from WT and HET hStrO neurons. (C(ii)) Quantification of AP amplitude. WT: *n* = 17 cells; HET: *n* = 20 cells. Mann–Whitney *U* test. (C(iii)) Quantification of membrane capacitance (C_m). Same *n* as in C(ii). Welch's *t* test.

(D) Axon initial segment defects in HET cortical neurons. (D(i)) Representative immunostaining of the axon initial segment (AIS) in hCO neurons labeled for Ankyrin-G (green). Scale bar: 10 µm. (D(ii)) Quantification of AIS length. WT: *n* = 42 neurons from 3 WT hiPSC lines (B07, C03, and KOLF2.1J); HET: *n* = 56 neurons from 3 HET hiPSC lines (F01, A02, and E04). Welch's *t* test.

(E) Bulk RNA-seq analysis of hCO-hStrO assembloids. (E(i)) Schematic of the bulk RNA-seq workflow and *SCN2A* expression measured as counts per million (CPM) in WT, HET, and HOM assembloids. *n* = 7 assembloids per group from 3 hiPSC lines. One-way ANOVA with Tukey's test. (E(ii)) Volcano plot of differentially expressed genes in HOM versus WT assembloids (FDR < 0.05). Downregulated genes are shown in blue, upregulated genes in magenta, and non-significant genes in gray. Selected downregulated genes associated with axon and synapse pathways are labeled. (E(iii)) Gene Ontology molecular function analysis showing overlapping downregulated ion channel-related pathways in HET versus WT and HOM versus WT assembloids. *n* = 7 assembloids per genotype from 3 hiPSC lines and 2 independent differentiation batches; FDR < 0.05, Benjamini–Hochberg correction. (E(iv)) Heatmap of selected ion channel-related gene expression changes across WT, HET, and HOM assembloids. (E(v)) Venn diagram showing overlapping upregulated genes in HET versus WT and HOM versus WT assembloids. (E(vi)) Reactome pathway enrichment analysis of the top 10 overlapping upregulated pathways, with key pathways associated with nonsense-mediated decay (NMD) highlighted in red.

(F) Longitudinal analysis of axonal projections in hCO-hStrO assembloids. (F(i)) Schematic of live-cell imaging of mScarlet-labeled cortical projections and eGFP-labeled striatal compartments at multiple time points after fusion. (F(ii)) Quantification of WT cortical axon coverage within the hStrO area over time. WT: *n* = 15 assembloids from 2 WT hiPSC lines. The same 15 WT assembloids are also included in Figure 2G(ii). One-way ANOVA with Tukey's test. (F(iii)) Representative images of reverse striatum-to-cortex projections on day 42 after fusion and quantification of $eGFP^+$ coverage within the hCO area over time, showing minimal reverse projection. WT: *n* = 15 assembloids from 2 WT hiPSC lines (KOLF2.1J and B07); HET: *n* = 16 assembloids from 3 HET hiPSC lines (A02, E04, and F01). Two-way ANOVA with Šídák's test. Scale bar: 100 µm.

(G) Reduced cortico-striatal projection in HOM assembloids. Representative images of cortical projections into the striatal compartment on day 42 after fusion in WT and HOM hCO-hStrO assembloids and quantification of cortex-to-striatum projection area. WT: *n* = 21 assembloids from 3 WT hiPSC lines; HOM: *n* = 12 assembloids from 3 HOM hiPSC lines. Welch's *t* test. Scale bar: 100 µm.

Data are presented as mean ± SEM. **p* < 0.05, ***p* < 0.01, ****p* < 0.001, *****p* < 0.0001.

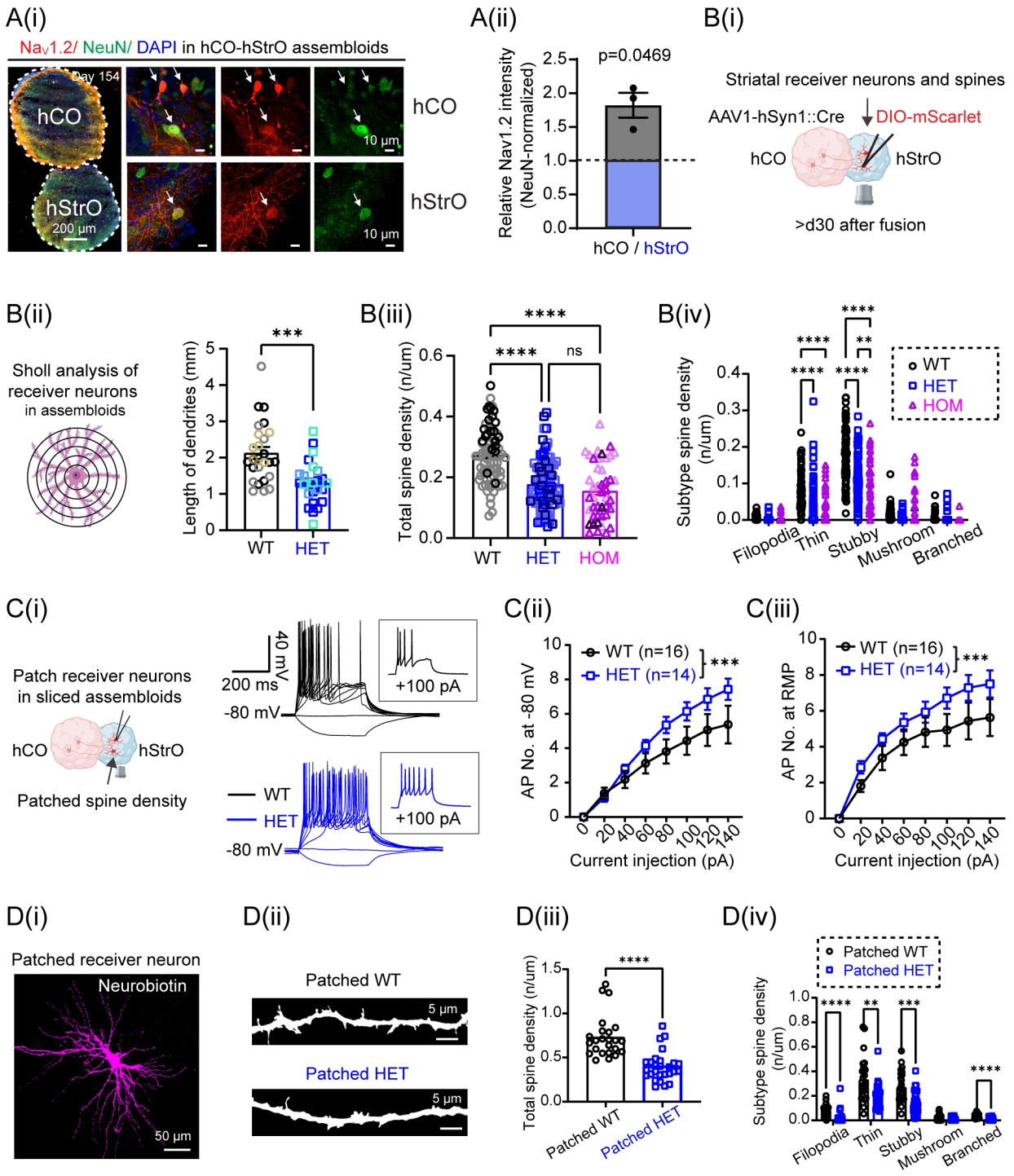


Figure S4. *SCN2A*-C959X reduces dendritic complexity and spine density while increasing receiver-neuron excitability in hCO-hStrO assembloids, related to Figure 3.

(A) Compartmental $Na_V1.2$ expression in hCO-hStrO assembloids. (A(i)) Immunostaining for $Na_V1.2$ (red), NeuN (green), and DAPI (blue) in day 154 hCO-hStrO assembloids. Higher-magnification views from the hCO and hStrO compartments are shown on the right. Scale bars: 200 µm and 10 µm. (A(ii)) Relative $Na_V1.2$ intensity in the hCO and hStrO compartments within

the same assembloid, normalized to NeuN. *n* = 3 assembloids from 2 WT hiPSC lines. Paired *t* test.

(B) Reduced dendritic arborization and spine density of striatal receiver neurons. (B(i)) Schematic of live-cell imaging of receiver neurons and spines in hCO-hStrO assembloids > 30 days after fusion. (B(ii)) Total dendritic length in WT and HET receiver neurons. WT: *n* = 26 neurons from 4 hiPSC lines; HET: *n* = 25 neurons from 3 hiPSC lines; unpaired *t* test. (B(iii)) Total spine density in WT, HET, and HOM receiver neurons. WT and HET data from Figure 3 are included for comparison with HOM. WT: *n* = 74 dendrites from 9 assembloids from 3 WT hiPSC lines (C03, KOLF2.1J, and B07); HET: *n* = 86 dendrites from 9 assembloids from 3 HET hiPSC lines (F01, A02, and E04); HOM: *n* = 44 dendrites from 9 assembloids from 3 HOM hiPSC lines (A03, D06, and F03). One-way ANOVA with Bonferroni's test. (B(iv)) Spine subtype densities. Same *n* as in B(iii). Two-way ANOVA with Šídák's test.

(C) Increased intrinsic excitability of HET striatal receiver neurons in hCO-hStrO assembloids. (C(i)) Schematic of whole-cell patch-clamp recording from receiver neurons followed by *post hoc* spine analysis, with representative firing traces from WT and HET receiver neurons at −80 mV in response to a series of depolarizing current injections. Insets show responses to +100 pA current injection. (C(ii)) Evoked AP number at −80 mV across increasing current injections. (C(iii)) Evoked AP number at RMP. WT: *n* = 16 cells from 8 assembloids from 2 WT hiPSC lines (A11 and KOLF2.1J); HET: *n* = 14 cells from 7 assembloids from 2 HET hiPSC lines (A02 and E04). Two-way ANOVA for C(ii) and C(iii).

(D) Reduced dendritic spine density of patched HET striatal receiver neurons in hCO-hStrO assembloid slices. (D(i)) Representative image of a Neurobiotin-filled patched receiver neuron. Scale bar: 50 μm. (D(ii)) Representative dendritic segments from patched WT and HET receiver neurons. Scale bars: 5 μm. (D(iii)) Total spine density. WT: *n* = 24 dendrites from 4 assembloids from 2 hiPSC lines; HET: *n* = 27 dendrites from 5 assembloids from 2 hiPSC lines. Mann–Whitney *U* test. (D(iv)) Spine subtype densities. Same *n* as in D(iii). Multiple Mann–Whitney *U* tests with Holm–Šídák correction.

Data are presented as mean ± SEM. ns, not significant, **p* < 0.05, ***p* < 0.01, ****p* < 0.001, *****p* < 0.0001.

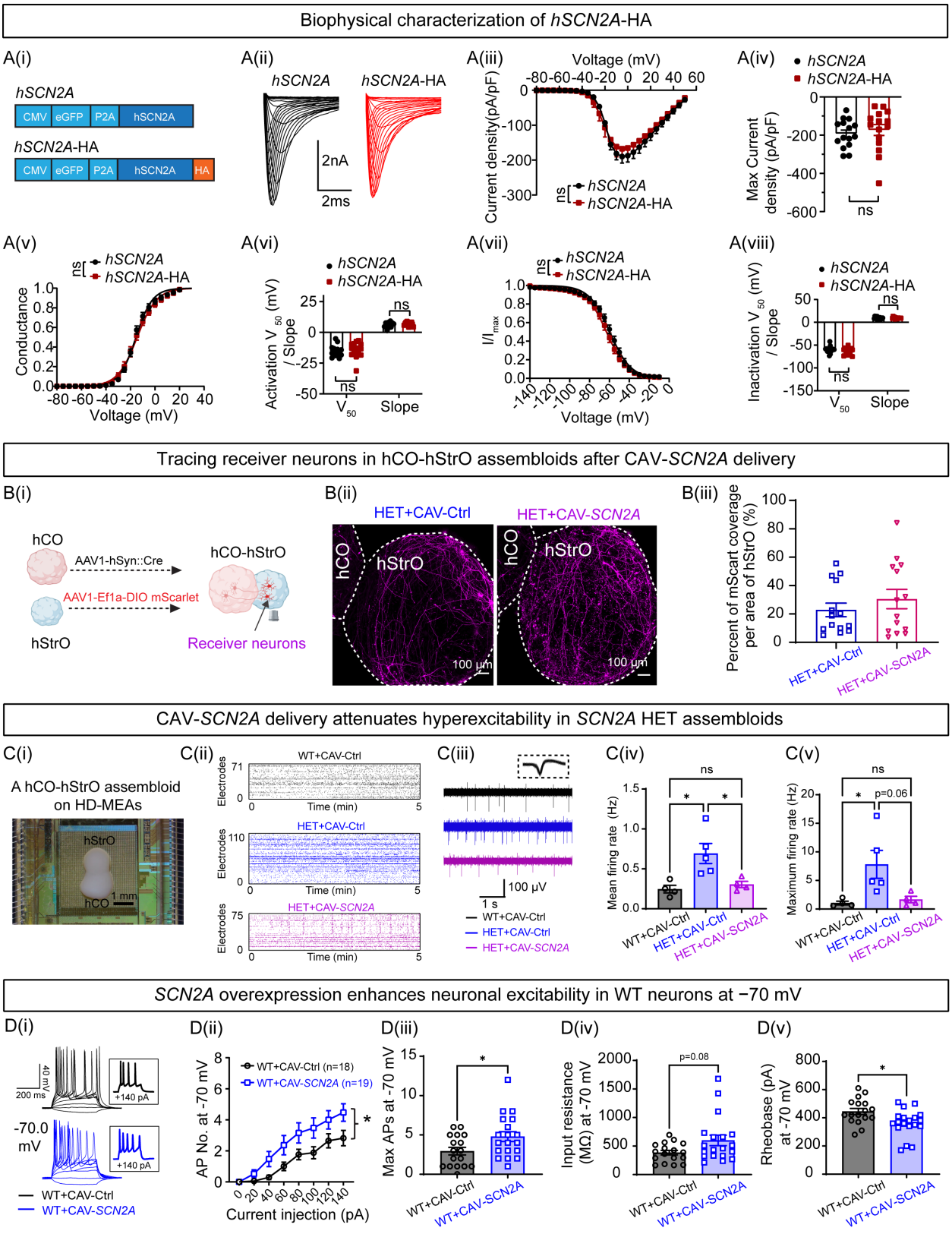


Figure S5. Biophysical validation of *hSCN2A*-HA vector and electrophysiological effects of CAV-*SCN2A* delivery, related to Figure 5.

(A) Biophysical characterization of *hSCN2A*-HA. (A(i)) Schematic of *hSCN2A* and HA-tagged *hSCN2A* expression constructs. (A(ii)) Representative whole-cell sodium current traces recorded from cells expressing *hSCN2A* or *hSCN2A*-HA. (A(iii)) Current density-voltage (I–V) relationship. (A(iv)) Quantification of maximal current density. (A(v)) Conductance-voltage (G–V) relationship. (A(vi)) Quantification of activation V_{50} and slope. (A(vii)) Steady-state fast inactivation curves. (A(viii)) Quantification of fast inactivation V_{50} and slope. For A(ii)–A(viii), *hSCN2A*: n = 15 cells; *hSCN2A*-HA: n = 15 cells. Curves in A(v) and A(vii) were fit using Boltzmann equations. Statistical comparisons were performed using two-way repeated-measures ANOVA for A(iii), A(v), and A(vii), and unpaired t tests for A(iv), A(vi), and A(viii); ns, not significant.

(B) Tracing of receiver neurons in hCO-hStrO assembloids after CAV-*SCN2A* delivery. (B(i)) Schematic of receiver neuron labeling in hCO-hStrO assembloids using AAV1-hSyn::Cre in hCOs and AAV1-Ef1a-DIO-mScarlet in hStrOs. (B(ii)) Representative images of receiver neuron labeling in HET+CAV-Ctrl and HET+CAV-*SCN2A* assembloids. Scale bar: 100 μm. (B(iii)) Quantification of mScarlet$^+$ coverage within the hStrO area. HET+CAV-Ctrl: n = 14 assembloids; HET+CAV-*SCN2A*: n = 14 assembloids. Data were obtained from 2 HET hiPSC lines (A02 and E04). Two-tailed unpaired t test; ns, not significant.

(C) CAV-*SCN2A* delivery attenuates elevated network firing in *SCN2A*-C959X HET assembloids. (C(i)) Representative hCO-hStrO assembloid on a high-density microelectrode array (HD-MEA). Scale bar: 1 mm. (C(ii)) Representative raster plots. (C(iii)) Representative single-electrode traces. (C(iv)) Mean firing rate. (C(v)) Maximum firing rate. WT+CAV-Ctrl: n = 4 assembloids; HET+CAV-Ctrl: n = 5 assembloids; HET+CAV-*SCN2A*: n = 4 assembloids. Data were obtained from 2 WT and 2 HET hiPSC lines; one-way ANOVA with Tukey's test.

(D) Exogenous *SCN2A* overexpression enhances intrinsic excitability of WT neurons held at −70 mV in dissociated hCO neurons. (D(i)) Representative firing traces from WT+CAV-Ctrl and WT+CAV-*SCN2A* neurons recorded at −70 mV. (D(ii)) Evoked AP number across increasing current injections. WT+CAV-Ctrl: n = 18 cells; WT+CAV-*SCN2A*: n = 19 cells. The same sample sizes apply to D(iii)–D(v). (D(iii)) Maximum AP number at −70 mV. (D(iv)) Input resistance at −70 mV. (D(v)) Rheobase at −70 mV. Statistical comparisons were performed using two-way ANOVA in D(ii), a two-tailed unpaired Welch's t test for D(iii), and two-tailed Mann–Whitney U tests for D(iv) and D(v).

Data are presented as mean ± SEM. ns, not significant, *$p < 0.05$, **$p < 0.01$.

Supplemental Tables

Table S1. Isogenic relationships among WT and *SCN2A* mutant hiPSC lines used in this study, related to STAR Methods.

***SCN2A* mutation**	**WT line(s)**	**Mutant line(s)**	**Isogenic relationship**
C959X	A11, B07, C03	F01, A02, E04 (HET); A03, D06, F03 (HOM)	A11, B07, and C03 are isogenic WT controls for the C959X mutant series
R524X	B5, C2, D6	E6 (HET)	B5, C2, and D6 are isogenic WT controls for the R524X mutant series

Table note: KOLF2.1J WT served as the common parental line from which all edited clones were derived.

Table S2. hiPSC lines used in each experiment and analysis, related to STAR Methods.

Experiment / Analysis	KOLF 2.1J WT	*SCN2A*-C959X									*SCN2A*-R524X			
		A11 WT	B07 WT	C03 WT	F01 HET	A02 HET	E04 HET	A03 HOM	D06 HOM	F03 HOM	B5 WT	C2 WT	D6 WT	E6 HET
Organoid / assembloid characterization	×	×	×	×							×		×	
qPCR	×		×	×	×	×	×	×	×	×				
Western blot		×		×		×	×		×	×	×	×	×	×
Patch-clamp, chemogenetic activation	×	×		×										
Patch-clamp, dissociated hCO neurons	×	×				×	×							
Patch-clamp, hCO slices	×	×	×		×	×								
Patch-clamp, hStrO slices	×	×				×	×				×		×	×
Patch-clamp, assembloid neurons	×	×				×	×							
Dendritic morphology / Sholl analysis	×	×	×	×	×	×	×							
Spine density and subtype analysis	×		×	×	×	×	×	×	×	×	×		×	×
Axon projection analysis	×		×	×	×	×	×	×	×	×	×		×	×
Anterograde / Retrograde viral tracing	×	×												
AIS analysis	×		×	×	×	×	×							
MEA recording	×	×				×	×							
Bulk RNA-seq	×		×	×	×	×	×	×	×	×				
Xenium spatial analysis	×												×	
CAV-*SCN2A* rescue validation	×	×				×	×							
CAV-*SCN2A* rescue electrophysiology	×	×				×	×							
CAV-*SCN2A* rescue spine analysis	×	×				×	×							
Cytogenetic microarray QC	×	×			×	×			×	×				

Table note: Isogenic relationships among WT and mutant lines are summarized in **Table S1**.

Table S3. High-density cytogenetic microarray quality-control summary of representative edited hiPSC lines used in this study, related to STAR Methods.

Line/Clone	Genotype	Role in study	Array QC	Novel sample-specific CNV	Background CNVs	Conclusion
KOLF2.1J	WT	parental WT	PASS	None detected	Known KOLF2-C1 CNVs only	No new detectable large-scale genomic abnormality
A11	WT	isogenic WT	PASS	None detected	Known KOLF2-C1 CNVs only	No new detectable large-scale genomic abnormality
A02	HET	isogenic HET	PASS	None detected	Known KOLF2-C1 CNVs only	No new detectable large-scale genomic abnormality
F01	HET	isogenic HET	PASS	None detected	Known KOLF2-C1 CNVs only	No new detectable large-scale genomic abnormality
D06	HOM	isogenic HOM	PASS	None detected	Known KOLF2-C1 CNVs only	No new detectable large-scale genomic abnormality
F03	HOM	isogenic HOM	PASS	None detected	Known KOLF2-C1 CNVs only	No new detectable large-scale genomic abnormality

Table note: All tested lines passed cytogenetic microarray quality control (QC). No novel sample-specific copy-number variations (CNVs) were detected; observed CNVs corresponded only to known KOLF2-C1/KOLF2.1J background variants.